HIGH EFFICIENCY CARBON DIOXIDE REMOVAL DEVICES FOR MINIMALLY INVASIVE PARTIAL RESPIRATORY ASSISTANCE

by

Richard Garrett Jeffries

B.S. in Bioengineering, University of Pittsburgh, 2010

Submitted to the Graduate Faculty of

the Swanson School of Engineering in partial fulfillment

of the requirements for the degree of

Doctor of Philosophy in Bioengineering

University of Pittsburgh

2017

UNIVERSITY OF PITTSBURGH

SWANSON SCHOOL OF ENGINEERING

This dissertation was presented

by

Richard Garrett Jeffries

It was defended on

March 31, 2017

and approved by

Marina V. Kameneva, Ph.D.
Research Professor of Surgery at the University of Pittsburgh School of Medicine, and
Professor of Bioengineering

William Wagner, Ph.D.
Director, McGowan Institute for Regenerative Medicine, and Professor of Surgery,
Departments of Bioengineering and Chemical Engineering

John Kellum, M.D.
Professor and Vice Chair for Research of Critical Care Medicine, s
Director, Center for Critical Care Nephrology, CRISMA Center, and CARe

Dissertation Director: William J. Federspiel, Ph.D.
William Kepler Whiteford Professor, Departments of Bioengineering, Critical Care Medicine,
and Chemical Engineering

HIGH EFFICIENCY CARBON DIOXIDE REMOVAL DEVICES FOR MINIMALLY INVASIVE PARTIAL RESPIRATORY ASSISTANCE

Richard Garrett Jeffries, Ph.D.

University of Pittsburgh, 2017

Acute and chronic lung injuries remain significant clinical problems, and are the third leading cause of death in the United States [1]. Carbon dioxide removal (CO_2R) devices can effectively manage acute hypercapnia in patients during treatment of acute exacerbations of chronic obstructive pulmonary disease (aeCOPD) and acute respiratory distress syndrome (ARDS) when combined with protective ventilation strategies [2–4]. Widespread adaptation of CO_2R systems for this purpose or early intervention have been hindered partially due to invasive placement of large diameter intravascular devices or high circuit blood flows necessary for available extracorporeal CO_2R ($ECCO_2R$) devices. We are in development of mechanical and enzymatic approaches that facilitate high efficiency CO_2 removal in artificial lung devices to minimize invasiveness of treatment with no or low blood flow outside the body.

The impeller percutaneous respiratory assist catheter (IPRAC) uses an array of rotating impellers in an annular bundle to generate an "active mixing" effect that enabled the highest efficiency CO_2R of any reported artificial lung device [5]. We investigated additional impeller design parameters finding gas exchange could be significantly improved by reducing impeller axial spacing. Total gas exchange in the IPRAC was improved by 10% versus previous work.

The impeller system was adapted for extracorporeal use in the ultra-low-flow ECCO$_2$R device (ULFED) with the objective of matching blood flow rates common for renal hemodialysis (250 mL/min). Effective CO$_2$R at ultra-low-flows enables adaptation of common renal hemodialysis connection strategies with potential for use with dialysis equipment or to be spliced directly in existing dialysis circuitry. CO$_2$ removal up to 75 mL/min (30-37% metabolic CO$_2$ production) at hemodialysis blood flows was demonstrated in the ULFED. The effects of bundle aspect ratio and impeller length on gas exchange were evaluated. Reducing bundle diameter was found to improve CO$_2$ removal performance, while bundle and impeller length insignificantly affected performance. Subsequent in vitro hemolysis testing showed the ULFED to be comparable to a control circuit, indicating no hemolysis related issues are anticipated in vivo.

Carbonic anhydrase (CA) enzyme fiber coatings were also evaluated for CO$_2$R enhancement. CA fibers previously demonstrating 37% improved performance with specific applications at ultra-low blood flows [6–8]. Mini-ULFED prototypes were fabricated but did not significantly outperform control fibers in gas exchange testing versus active mixing alone.

TABLE OF CONTENTS

LIST OF TABLES

LIST OF FIGURES

ACKNOWLEDGEMENTS

I would like to thank my advisor Dr. William Federspiel for the opportunity to develop as a scientist and engineer in the Medical Devices Laboratory. His mentorship pushed me to always critically evaluate my research approach keeping translational objectives in mind. Experience I gained in the lab enabled me to collaborate with clinical and industrial experts, as well as how to effectively design and conduct meaningful experiments.

A special thank you to each member of the Medical Devices Lab I had the pleasure of working with. None of this work would have been possible in a research environment lacking the strong focus on collaborative problem solving I relied on during my time in the lab. Thanks especially to Brian Frankowski, who steered me in the right direction daily as a co-worker and friend, whom I owe all my development as a fabricator.

I would also like to thank Dr. Sanjeev Shroff, Chair of Bioengineering and the Cardiovascular Bioengineering Training Program (CBTP). Learning from and interacting with fellow trainees having diverse research focuses and gaining clinical experience helped me develop an invaluable breadth of knowledge in bioengineering and an appreciation for lifelong learning I will continue to build on. Finally, a very special thanks to my family and friends who supported me throughout graduate school.

I would also like to acknowledge and thank my funding sources. Without support from the National Institutes of Health (NIH) and National Heart, Lung, and Blood Institute (NHLBI)

(5R01HL070051-08, 5R01HL117637-05), the University of Pittsburgh CBTP training grant (NIH T32-HL076124) and Department of Bioengineering, The McGowan Institute for Regenerative Medicine, and the Commonwealth of Pennsylvania, none of this work would have been possible.

NOMENCLATURE AND LIST OF EQUATION VARIABLES

A_f	Total fiber surface area, cm^2
a	Reynolds coefficient
a_v	Membrane surface area per bundle volume, 1/cm
α_{CO_2}	CO_2 solubility in blood, $mL_CO_2/mL/mmHg$
b	Reynolds coefficient
C_{CO_2}	CO_2 gas concentration in blood, mL
D_{CO_2}	CO_2 diffusivity in blood, cm^2/s
D_{eff}	CO_2 effective diffusivity in blood, cm^2/s
D_f	CO_2 facilitated diffusivity in blood, cm^2/s
D_{HCO_3}	Bicarbonate ion diffusivity in blood, cm^2/s
d_h	Hydraulic diameter, cm
F_{CO_2}	Mass fraction of gaseous CO_2, %
HCT	Blood hematocrit, %
K_{CO_2}	CO_2 permeance, $mL/cm^2/s/cmHg$
k	CO_2 mass transfer coefficient, $mL_CO_2/cm^2/mmHg/s$
L	Bundle length, cm
λ	CO_2 effective solubility (dissolved and bound), $mL_CO_2/mL/mmHg$
μ	Blood dynamic viscosity, cP
P_{CO_2}	CO_2 partial pressure, mmHg
pCO_2^{inlet}	CO_2 partial pressure in blood, inlet, mmHg
$pCO_{2,b}$	Blood CO_2 partial pressure, mmHg
$pCO_{2,g}$	Sweep gas CO_2 partial pressure, mmHg
$pfHb$	Plasma free hemoglobin concentration, g/L
Q	Average blood flow rate, mL/min
Q_{OUT}^{STP}	Corrected mass flow rate of sweep gas, outlet, L/min
Re	Reynolds number
ρ	Blood density, g/mL
Sc	Schmidt number
Sh	Sherwood number
t	Time, s
V	Blood volume, mL
V_{CO_2}	Overall CO_2 mass transfer rate, mL/min
$V_{CO_2}^*$	Normalized CO_2 removal rate, mL/min
v	Superficial fluid velocity, m/s

aeCOPD	Acute Exacerbations of COPD
ARDS	Acute Respiratory Distress Syndrome
$AVCO_2R$	Arteriovenous CO_2 Removal
CA	Carbonic Anhydrase
CFD	Computational Fluid Dynamics
COPD	Chronic Obstructive Pulmonary Disease
CPB	Cardiopulmonary Bypass
CRRT	Continuous Renal Replacement Therapy
$ECCO_2R$	Extracorporeal CO_2 Removal
ECMO	Extracorporeal Membrane Oxygenation
Fr	French, Units of Insertion Diameter: 1 Fr = 1/3 mm
HCO_3	Bicarbonate ion
HFM	Hollow Fiber Membrane
ID	Inner Diameter
IMV	Invasive Mechanical Ventilation
IPRAC	Impeller Percutaneous Respiratory Assist Catheter
IVC	Inferior Vena Cava
IVOX	Intravenous Oxygenator
LPV	Lung Protective Ventilation
NIV	Non-Invasive Ventilation
NIH	Normalized Index of Hemolysis
P_{plat}	Plateau Pressure
pCO_2	CO_2 Partial Pressure
PMP	Polymethylpentene
PP	Polypropylene
pfHb	Plasma free hemoglobin
RAS	Respiratory Assist System
RPM	Rotations Per Minute
SEM	Scanning Electron Microscope
SLA	Stereolithography
STP	Standard Temperature Pressure
TIH	Therapeutic Index of Hemolysis
ULFED	Ultra-Low-Flow $ECCO_2R$ Device
ULPV	Ultra-Protective Lung Ventilation
VT	Tidal Volume
VILI	Ventilator-Induced Lung Injury
$VVCO_2R$	Venovenous CO_2 Removal

1.0 INTRODUCTION

Lung disease remains a global concern and is the third leading cause of death in the United States, responsible for 147,000 deaths annually [9]. Treatment typically consists of invasive mechanical ventilation (IMV) where patients are intubated and sedated, and can further exacerbate lung injuries due to high tidal volumes and inspiratory pressures. Alternative treatments utilize membrane gas exchangers that perform respiratory function independent of the lungs, allowing the injured tissue to rest and heal. Emerging technologies have improved efficiency and effectiveness of this approach and show promise to minimize the need for IMV. This chapter describes both approaches as well as two prevalent forms of lung disease that motivated work in this field, Chronic Obstructive Pulmonary Disease (COPD) and Acute Respiratory Distress Syndrome (ARDS). The objective of this project was to develop previously unexplored approaches for highly efficient CO_2 removal in an intravascular or extracorporeal device that enables minimally invasive partial respiratory assistance and treatment of acute hypercapnic respiratory failure. The basic principles of artificial lung technology and overall goals of this work are also described in this chapter.

1.1 RESPIRATORY DISEASES

Chronic forms of lung failure such as chronic obstructive pulmonary disease (COPD) currently afflict an estimated 23.6 million Americans [10]. COPD is a group of respiratory conditions including chronic bronchitis (bronchiole inflammation) and emphysema (deterioration of alveolar elasticity), characterized by dyspnea, lung airflow limitations, coughing, and other symptoms [11]. The condition is diagnosed in 80-90% of cases due to smoking related airway injuries, but environmental and genetic factors such as exposure to air pollution, second-hand smoke, and occupational dust and chemicals can also lead to COPD [12]. The economic burden of COPD in the United States is considerable, costing an estimated $43 billion in direct and indirect costs in 2007 [10]. Less severe cases can be treated with pharmacotherapies to manage symptoms, but this approach has not been shown to modify the long-term decline of lung function, and patient adherence to prescribed therapy is low [10].

Acute exacerbations of COPD (aeCOPD) can onset from bacterial exposure, viral infection, or exposure to pollution [13]. Defined as a change in a patient's "baseline dyspnea, cough, and/or sputum that is beyond day-to-day variations, is acute in onset, and may warrant a change in regular medication in a patient with underlying COPD", aeCOPD hospitalizes over 725,000 patients annually, with a mortality rate of 10-25% [14]. aeCOPD can normally be treated with antibiotics and corticosteroids for mild exacerbations, but in the 15–25% of cases associated with moderate-to-severe respiratory acidosis (pH < 7.25 and/or $PaCO_2$ > 45 mmHg) patients are often transitioned to invasive mechanical ventilation (IMV) [14]. IMV requires patients to be sedated and intubated to allow forced respiration using high tidal volumes (~12 mL/kg) and plateau pressures (P_{plat} >30 cmH_20) [15]. Outcomes using IMV demonstrate benefit versus no treatment, however the aggressive volumes and pressures necessary for full respiratory

support introduce a risk of barotrauma and volutrauma [15]. High pressures risk epithelial and endothelial injury with subsequent pulmonary edema and protein leakage, while high tidal volumes can cause over-distension and rupture of alveolar tissue [15]. The risk of ventilator-induced lung injuries (VILI) can be alleviated by reducing vent settings, but this may reintroduce hypercapnia and blood acidosis, and complicates weaning from ventilation. Recent work has demonstrated aeCOPD patients can benefit from non-invasive ventilation (NIV), where intubation is avoided by using a facial mask for respiration [14]. NIV has become the standard of care in severe exacerbations of COPD versus traditional IMV, reducing mortality rates from 23% to 9% [16, 17]. 15–26% of patients still fail NIV and are transitioned to IMV however, where mortality rates are greater than if the patient had initially been treated with IMV [16, 18–21]. Common indications of NIV failure are hypercapnia, severe acidosis, dyspnea, and increased respiratory rate – all manifestations of inadequate CO_2 management [22]. The issues associated with hypercapnia during ventilation in severe ae-COPD demonstrate a need for additional management of blood CO_2 in patients during NIV to prevent intubation, and during IMV to improve weaning.

An acute form of respiratory failure, ARDS, is the result of pulmonary inflammation in response to direct or indirect insult and has mortality rates between 40-45%, afflicting around 190,000 patients annually [23–25]. ARDS is characterized by a breakdown of the alveolar-capillary barrier leading to the flooding of alveolar sacs and a dramatic reduction in gas exchange effectiveness as resistance to gas diffusion in the fluid filled sac increases [26]. ARDS is clinically indicated as severe hypoxemia that is rapid onset, with radiographic evidence of bilateral pulmonary infiltration, the absence of left heart failure, and is generally diagnosed in patients already critically ill from shock, pneumonia, sepsis, or other trauma [24, 27]. Death

usually results from widespread hypoxemia and multi-organ failure rather than lung failure alone [24]. IMV is the traditional approach for ARDS therapy, but the ARDSnet studies demonstrated patients can benefit from lung-protective ventilation (LPV) using lower tidal volumes (V_T = 6 mL/kg) and plateau pressures (P_{plat} <30 cmH_2O) [28]. These recommendations demonstrated a reduction in mortality rates by 22% versus traditional IMV settings (V_T = 12 mL/kg), however, more recent studies have shown that patients are still at risk of VILI [28, 29]. The reduced mortality rates were shown to be linearly related to V_T and P_{plat} settings, leaving several to postulate that further reduction of these settings may improve outcomes (ultra-protective lung ventilation, ULPV: V_T = 4 mL/kg, $P_{plat} \leq$ 25 cmH_2O) [30]. Avoidance of injury using this approach can sufficiently oxygenate patients but CO_2 removal requires higher tidal volumes. This introduces serious risks of inducing hypercapnia with subsequent respiratory acidosis and related injuries [23]. As with aeCOPD, newer ventilation techniques are beneficial for ARDS treatment, but CO_2 removal remains a challenge that if left unmanaged can negate the benefits of newer treatments. The clinical need for additional means of mitigating respiratory acidosis in these two patient populations are among the primary motivations behind the development of CO_2 removal devices as well as this project.

1.2 ARTIFICIAL LUNGS FOR CO_2 REMOVAL

Gas exchange specifically targeting CO_2 removal was conceptualized by Kolobow and Gattinoni in the late 1970's. They demonstrated in lambs that if a portion of the metabolic CO_2 production could be eliminated during IMV by alternative means, vent settings could be modified to reduce tidal volumes, peak inspiratory pressure, and respiratory rate [31, 32]. The basic principles of

operation of CO_2 removal devices are shared with extracorporeal membrane oxygenation (ECMO). The key advantage for CO_2 removal devices is that a significant volume of CO_2 is present in relatively small volumes of blood, and extracorporeal CO_2 removal ($ECCO_2R$) treatment can be effective at comparatively lower blood flow rates. CO_2 is predominantly carried in the form of highly soluble bicarbonate ion that rapidly restores depleting CO_2 as it is eliminated, and the CO_2 dissociation curve is essentially linear and does not saturate like the oxyhemoglobin dissociation curve [31, 33, 34]. The full metabolic production of CO_2 (200 mL/min) is contained in approximately 400 mL of blood, meaning that an artificial lung can theoretically fully support CO_2 removal needs at blood flow rates ~10% of that necessary for equivalent oxygenation support (4-7 L/min) [35, 36]. While ECMO systems could be jointly utilized for CO_2 removal, the differences in exchange dynamics and the benefits CO_2 management alone can provide, there is significant potential and need for the development of minimally invasive systems specific to this application.

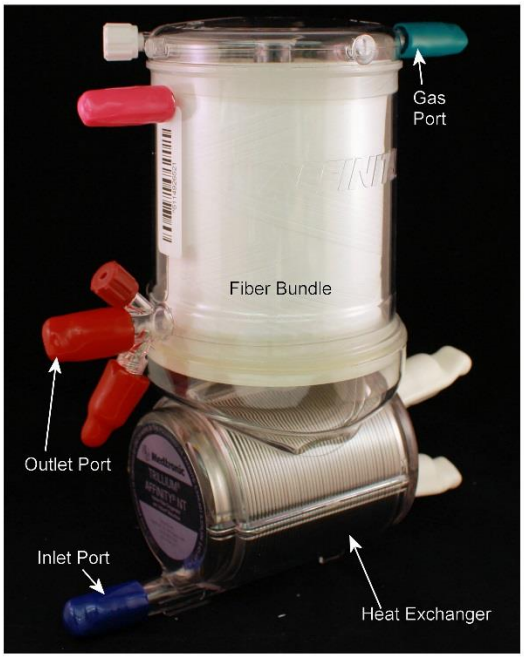

Figure 1.1. Artificial Lung Device. Medtronic Affinity artificial lung cartridge showing common elements of oxygenator devices.

1.2.1 Gas Exchange Dynamics in Hollow Fiber Membranes

Modern artificial lung devices are primarily built on the same basic concept of gas exchange via partial pressure differences across a packed bed of microporous hollow fiber membranes (HFMs). This concept has been implemented in various ways to maximize efficiency, minimize invasiveness, and reduce complexity with the development of extracorporeal [37–40], intravascular [5, 41–46], and paracorporeal [47–49] artificial lung devices. Extracorporeal designs (Figure 1.1) are largely derived from cardiopulmonary bypass (CPB) systems and consist of a flow-through cartridge containing a large bundle of hollow fiber membranes. Blood passes over membranes outside of fibers, and gas exchange occurs through the fiber wall. A sweep gas,

often pure O_2, flows through hollow fiber membrane lumens, creating a partial pressure gradient between gas levels in the blood and sweep gas that facilitates diffusion across the fiber wall. Fibers have microporous walls and are fabricated from hydrophobic polymers such as polypropylene (PP) and modern polymethylpentene (PMP) making them permeable to gasses, but impermeable to fluids [50]. This material property enables effective separation of gas and blood pathways. Both O_2 and CO_2 diffuse across the membrane wall based on a differential gradient, where O_2 moves into the blood with a strong gradient (pO_2^{gas}: pO_2^{blood} ≈ 700:45 mmHg) and CO_2 exits the blood into the sweep gas down a weaker gradient (pCO_2^{gas}: pCO_2^{blood} ≈ 50:0 mmHg). Once in blood the majority of O_2 binds to hemoglobin within red cells, which quickly become saturated (inlet → outlet saturation ≈ 65 → 100%). In contrast the majority of CO_2 in blood is in the form of bicarbonate ion (HCO_3), which dramatically increases the carrying capacity of CO_2 in blood, but maintains pCO_2 at relatively low levels making decarbonation challenging. As a result of the high carrying capacity the exchange rate of CO_2 is largely independent of blood flow rate and can be achieved at significantly lower flow rates (<500 mL/min) than those needed for oxygenation.

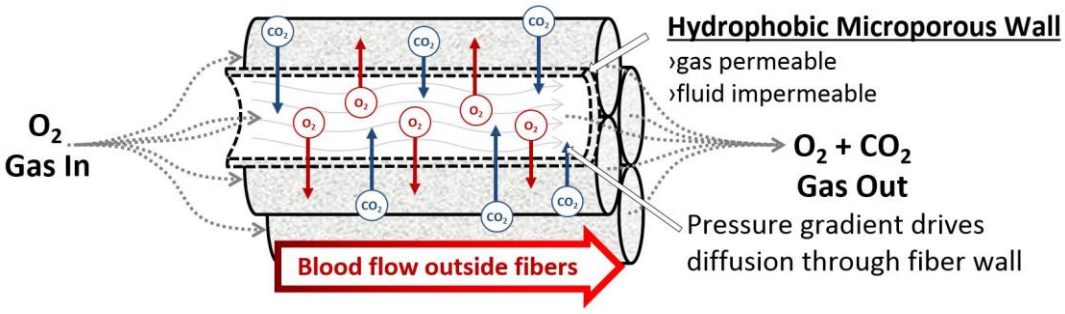

Figure 1.2. Gas exchange between blood and sweep gas across HFM wall.

Gas exchange rate is also largely dependent on diffusive resistances of gasses in fluid. The overall mass transfer rate is $\dot{V}_{CO_2} = K_{CO_2} A_f \left(pCO_{2,g} - pCO_{2,b}\right)$ where K_{CO_2} is the CO_2 permeance, A_f is the fiber membrane surface area, and $pCO_{2,g}$ and $pCO_{2,b}$ are the CO_2 partial pressures in the sweep gas and blood, respectively. Gas permeance is dictated by the diffusive resistances in the sweep gas pathway, through the membrane wall, and through blood [50]. Transfer resistance within the sweep gas pathway itself is negligible, so the permeance is primarily dependent on blood-side resistance and to a lesser extent the membrane resistance. Blood-side resistance is a function of the diffusional boundary layer thickness that exists on the gas exchange surface, where fluid velocity is reduced by drag forces. Within the boundary layer molecular diffusion dominates in contrast to convection that occurs in bulk flow. The overall rate of gas transfer is therefore limited by the diffusional distance necessary to traverse the surface boundary layer. CO_2 near the fiber surface within the boundary layer is quickly eliminated but the majority of additional CO_2 comes from bulk flow, requiring it to first diffuse the full thickness of the boundary layer to reach the fiber surface. Most modern artificial lungs take advantage of cross-flow fiber orientations rather than parallel orientations, which to an extent reduces development of the surface boundary layer [50, 51]. A more effective means of reducing the fiber boundary layer thickness is by increasing fluid velocity, which directly impacts the boundary layer and improves gas exchange efficiency. Several devices previously developed and in use utilize this approach to enhance performance by mechanically agitating blood near fibers to increase fluid velocity, creating an "active mixing" effect that will be expanded on in the following section and Chapter 2. A more detailed analysis of the equations and factors governing CO_2 transfer rates are also presented in Section 5.2.4.

1.3 INTRAVASCULAR CO_2 REMOVAL DEVICES

Carbon dioxide removal devices have been developed for intravascular and extracorporeal use. Intravascular devices, or respiratory assist catheters, are intended for percutaneous insertion into the inferior vena cava and generally consist of a long slender fiber bundle. The primary advantage of this approach is that it eliminates the complexity and concerns associated with traditional extracorporeal circuits. A device without blood circuitry obviates use of a blood pump, reduces blood-contacting surface area, simplifies device management, and avoids fluid loading patients with a primed circuit during device connection/insertion. An intravascular also exposes the device to the majority of the cardiac output (≈2/3), minimizing potential for flow rate limited gas exchange observed in low-flow $ECCO_2R$ devices.

The major challenge in development of intravascular devices is removing enough CO_2 with a form factor compact enough to function in the vasculature [52]. CO_2 removal of 70-160 mL/min has been shown to benefit patients with hypercapnia, which translates to a target CO_2 removal rate of ≥25-35% metabolic CO_2 production (~200-250 mL/min) at normocapnia (pCO_2 = 45 mmHg) [53, 54]. This level of gas exchange is challenging with small surface areas so most research in this area has focused on development of approaches that increase gas exchange efficiency. The first successful design was the Intravenous Oxygenator (IVOX), which to date is the only catheter device tested in humans [42, 55]. The IVOX used crimped fibers to disturb blood flow pathways and avoid fiber clumping in the vena cava, and achieved CO_2 removal rates up to 40–70 mL/min [56]. Approximately 30% of patients showed improvements in blood gasses such that ventilator settings could be reduced, however performance levels were deemed insufficient and clinical trials were halted [42]. Additional concerns surrounding the large

insertion size of the IVOX (34–50 Fr) that required a specialized surgeon for placement ultimately suspended further developments [57, 58].

Later respiratory assist catheters focused on improving overall gas exchange and reducing insertion size using novel approaches to maximize efficiency. The Hattler Catheter shown in Figure 1.3 uses a pulsating balloon inside an annular fiber bundle to generate an "active mixing" effect that increases flow velocity through the bundle [59]. Greater velocity and bundle cross-flow diminish the highly limiting diffusive boundary layer at the gas exchange surface, facilitating maintenance of stronger gaseous concentration gradients spanning fiber walls and increasing transfer efficiency. Active mixing improved gas transfer in the Hattler Catheter to levels 50–300% greater than non-pulsating devices [60]. Despite promising performance the large insertion size of the Hattler Catheter (32 Fr) ultimately limited clinical appeal and development was suspended.

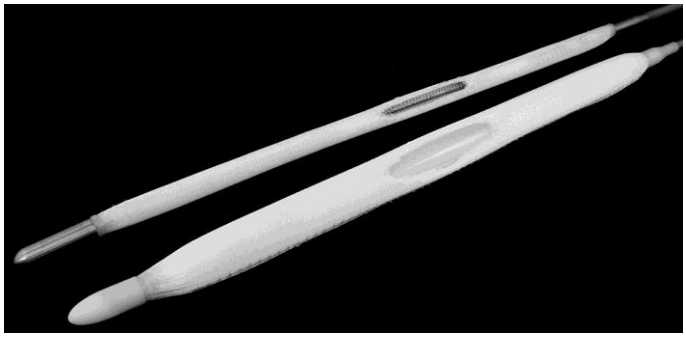

Figure 1.3. Hattler Catheter & IPRAC Respiratory Assist Catheters. Cutaway fiber sections showing indwelling balloon (Hattler Catheter, bottom) and rotating impellers inside safety coil (IPRAC, top).

The majority of other reported designs used novel fiber arrangements and mechanical mechanisms to enhance performance but were unable to achieve clinically relevant levels of total gas exchange. Notable examples are the PENSIL, which used pressure cycling in closed-end fibers [43, 61], the D-ILAD that arranged fibers in a rotating Archimedes screw [44], the HIMOX using fibers in an expanding disk-shaped configuration [45, 62], and the IVLAD with fibers wrapped over a vibrating actuator to impose active mixing [46].

1.3.1 The Impeller Percutaneous Respiratory Assist Catheter (IPRAC)

The most recent development in this area and one primary focus of this project is the Impeller Percutaneous Respiratory Assist Catheter (IPRAC) in development in our lab (Figure 1.3). The IPRAC consists of a slender HFM bundle surrounding an array of rotating impellers that generate highly effective active mixing [5]. CO_2 removal rates up to 529 mL/min/m^2 were achieved (39 mL/min total) on the bench, the highest efficiency of any reported gas exchanger. Previous work focused primarily on characterizing the relationship between rotation rate and gas exchange, as well as evaluation of various impeller geometries. In these studies a strong relationship between impeller design and gas exchange was observed, suggesting further improvements could be made to increase IPRAC performance. The existing design has an insertion diameter of 25 Fr, which we believe can be reduced by improving total CO_2 removal rates through investigation of new impeller designs and implementation of carbonic anhydrase (CA) immobilized HFMs. This bioactive fiber approach was shown to improve CO_2 removal rates by up to 36% in blood by facilitating the conversion of bicarbonate ions to CO_2 within the fiber boundary layer [7]. Chapter 6.0focuses on the combination of these technologies.

The primary objective of this project is to improve upon existing technologies to develop minimally invasive CO_2 removal devices. The design objectives for a respiratory assist catheter are:

1. CO_2 removal rates equivalent to 25-35% of the metabolic CO_2 production ($\geq$65 mL/min) at normocapnia ($pCO_2 \approx 45$ mmHg).
2. Minimally invasive insertion diameter (< 20 Fr).
3. In vitro hemolysis levels comparable to a gas exchange circuit of commercially available components.

1.4 EXTRACORPOREAL CO_2 REMOVAL DEVICES ($ECCO_2R$)

CO_2 removal devices were initially conceptualized as extracorporeal systems and the most progress has been in this area. Three general approaches for extracorporeal CO_2 removal ($ECCO_2R$) have been explored – arteriovenous CO_2 removal ($AVCO_2R$), venovenous CO_2 removal ($VVCO_2R$), and low-flow systems intended for compatibility with CRRT (continuous renal replacement therapy) circuits. Several technologies for enhancing performance efficiency have also been utilized that could potentially be integrated within any of these systems including active mixing, bioactive fibers, blood acidification, and electrodialysis.

1.4.1 Arteriovenous CO_2 Removal ($AVCO_2R$)

The most commonly used configuration of $ECCO_2R$ is with arteriovenous cannulation. $AVCO_2R$ uses a low-resistance oxygenator (Novalung iLA) in a circuit generally bridging the femoral

artery and vein [63]. The arteriovenous pressure differential drives flow through the circuit, eliminating the need for a blood pump. At flow rates up to 1.5 L/min, CO_2 removal rates of 100–200 mL/min were reported in acute animal models of ARDS [49, 64, 65]. In a clinical report $AVCO_2R$ was shown to help avoid intubation for IMV in 19 of 21 patients (10% intubation rate, versus 100% in the control arm), however there was no difference in long-term mortality rates [66]. There are several limitations associated with $AVCO_2R$ however. Circuit flow is dependent on cardiac output and therefore any peripheral vascular disease or decompensated heart failure are contraindications for use [67]. Cannulation also risks ischemia and limits ambulation, promoting patient deconditioning [53]. The large bore, dual cannulation required to sustain the high blood flows has also limited clinical appeal of $AVCO_2R$ for early intervention, a shortcoming that has become a focal area for improvement with newer technologies.

1.4.2 Venovenous $ECCO_2R$ ($VVCO_2R$)

Recent developments in $ECCO_2R$ have focused on addressing the limitations of $AVCO_2R$. New $ECCO_2R$ systems incorporate a blood pump that eliminates the cardiac-related contraindications and enables single-site venovenous cannulation, and can operate at lower blood flows (≤500 mL/min) to allow the use of smaller bore cannula. The Hemolung Respiratory Assist System (RAS) from ALung Technologies is an integrated pump-oxygenator that uses a 15.5 Fr dual-lumen cannula for patient connection [22]. A rotating smooth-walled cylindrical core adjacent to gas exchange fibers generates secondary flows within the HFM bundle (0.59 m^2), making it the only approved device that incorporates a mechanism specifically for active mixing. This feature increases in vitro CO_2 removal by up to 60%, generates significant washing to minimize thrombus formation and reduces fiber surface area required for respiratory support [68]. The

Hemolung has been reported in several case studies to be an effective co-therapy to NIV for patients with aeCOPD as a means to avoid intubation or aid weaning from IMV [3, 4, 69, 70]. In 15 patients with moderate ARDS the Hemolung was used to regulate $PaCO_2$ and pH during UPLV (V_T = 4 mL/kg) with minimal complications, and will be included in the upcoming SUPERNOVA (A Strategy of UltraProtective lung ventilation With Extracorporeal CO_2 Removal for New-Onset moderate to seVere ARDS) trials for assessment of $ECCO_2R$ to facilitate UPLV in moderate to severe ARDS [23].

Novalung's iLA Activve system includes a central controller with compatibility for several passive gas exchange cartridges for a range of blood flow rates ranging from low-flow $ECCO_2R$ to ECMO. Using the "mid-flow" cartridge (1.3 m^2 iLA Membrane Oxygenator also used in $AVCO_2R$) and 22 Fr cannula, CO_2 removal rates <50 mL/min were observed at a blood flow of 0.5 L/min in 10 hypercapnic patients [71]. In controlled clinical trials (ECLAIR), intubation was avoided in 14/25 patients (56%) with acute hypercapnic respiratory failure refractory to NIV, however major bleeding was observed in 36% of patients in addition to other major complications associated with the device including extracorporeal clotting and air detection in the circuit [72]. The "low-flow" iLA Activve kit uses a cylindrical bundle design (0.35 m^2) and is intended for blood flows ≤ 800 mL/min using an 18 Fr dual lumen cannula for venous access, but data available for this configuration is limited.

1.4.3 Low-Flow $ECCO_2R$

Developing $ECCO_2R$ systems primarily direct focus on further reducing necessary blood flow rates for venovenous treatment to 200-400 mL/min. The Hemodec DECAPsmart uses a pediatric membrane lung (0.3 m^2) in series with a polysulfone hemofilter (1.35 m^2) to operate at low blood

flows (<500 mL/min) [73]. Plasma is pulled out of blood in the hemofilter and then recirculated back to an oxygenator. Plasma recirculation increases the flow rate through the oxygenator thereby improving gas transfer efficiency by means similar to active mixing, i.e. increased blood velocity at the fiber surface to reduce the diffusive boundary layer thickness. The DECAPsmart was successfully used in adults and children before the design was acquired, becoming the Estor ProLUNG [74–76]. The oxygenator has since been replaced with a larger surface area device (1.8 m^2) and the novel plasma recirculation component was eliminated, reducing the complexity of the system. In a small study using the modified design, intubation was avoided in 88% of patients on NIV and $ECCO_2R$ with acute hypercapnic respiratory failure associated with aeCOPD versus 66% avoidance with NIV alone, however this difference was not statistically significant and complication rates were high (51% of patients, primarily due to device malfunction) [77]. Maquet also began development of the PALP CO_2 removal system that could operate at flows down to 0.2 L/min using a 0.98 m^2 gas exchanger cartridge for use with their CARDIOHELP system [78]. Average CO_2 removal rates of ~60 mL/min were reported at these flows in hypercapnic pigs, however planned aeCOPD clinical trials were canceled prior to enrollment [78, 79].

The PrismaLung system was the first artificial lung to be designed specifically as an attachment to existing hemodialysis hardware. The system consists of a Medos Hilite 800 LT pediatric oxygenator (0.32 m^2) fitted to a Gambro-Baxter Primaflex hemodialysis controller with 13 Fr dual lumen dialysis cannula. Performance was evaluated in hypercapnic pigs ($PaCO_2$ > 80 mmHg) with modest removal rates ≤60 mL/min at blood flow rates of 400 mL/min [80]. $PaCO_2$ levels were reduced but not returned to normal levels (81 mmHg to 70 mmHg). At low flows (200–300 mL/min) CO_2 removal rates were lower (40–55 mL/min). The benefit to patients at

these low performance points will be assessed in upcoming human trials with the PrismaLung for use with CRRT hardware [81] and as UPLV co-therapy for mild–moderate ARDS [82] and severe ARDS [83].

1.4.4 Approaches for Enhancing CO_2 Removal

Several alternative approached to enhance CO_2 removal efficiency have been explored to reduce flow rates necessary for clinically significant gas exchange. Bioactive fibers that have carbonic anhydrase (CA) enzyme immobilized on gas exchange surfaces locally convert bicarbonate ion to CO_2 at the fiber surface [7, 8]. CO_2 removal rates improved up to 37% using CA fibers in blood versus untreated control fibers in miniaturized artificial lung modules [84]. Disruption of the diffusive boundary layer in an active mixing system may also improve enhancement associated with CA fibers, which is investigated in Chapter 6.0. CA fiber performance can also be improved by adding small amounts of acidic sulfur dioxide (SO_2) gas to fiber sweep gas [85]. Diffusion of acidic species directly into the surface boundary layer increases local pCO_2 by promoting the conversion of bicarbonate ion to CO_2 at the gas exchange surface. This increases the partial pressure driving gradient across fiber walls and improves CO_2 removal. Acid gas alone enhanced gas exchange by 17%, but worked synergistically with CA fibers to increase CO_2 removal by 109% in miniaturized artificial lung modules. Whole blood acidification has also been investigated with infusion of lactic acid to an $ECCO_2R$ circuit [86, 87]. CO_2 removal rates improved up to 78% during 48 hour studies in pigs with no indications of significant organ or erythrocyte damage. Electrodialysis has been explored to modulate blood electrolyte concentrations to promote bicarbonate conversion to CO_2 in a gas exchange circuit [88, 89]. CO_2 removal nearly doubled (to 112 mL/min) at low blood flows of 250 mL/min in five acute studies

in pigs, but further testing is necessary to assess safety with respect to renal function. Bicarbonate dialysis was evaluated in acute sheep studies to eliminate CO_2 from blood in the form of bicarbonate ion [90]. A hemofilter was used to remove 100-150 mL/min of ultrafiltrate from 350-400 mL/min of blood containing CO_2 and bicarbonate and replaced with an equal volume of sodium hydroxide replacement solution. An average 60 mL/min of CO_2 was removed from blood at normocapnia without complications.

Several novel approaches have been explored for enhancing CO_2 removal in HFM devices that are largely independent of bundle design and could be used to reduce fiber surface area, achieve greater overall gas exchange performance, or reduce necessary blood flow rates. Active mixing, as described above and later in Chapter 2.0, is an established means of increasing CO_2 and O_2 exchange efficiency and has been implemented in the approved Hemolung $VVCO_2R$ system as well as the majority of respiratory assist catheters previously developed. This approach shows significant promise and is critical to the functionality and effectiveness of each of the devices described in this project. Bioactive HFMs have also been investigated to specifically improve CO_2 removal [6]. Carbonic anhydrase (CA) is an enzyme native to erythrocytes that is responsible for catalyzing the reversible reaction that converts CO_2 gas to its predominant form in blood, bicarbonate ion (HCO_3). Immobilization of CA enzyme directly to the fiber surface allows depleted CO_2 within the boundary layer to be replenished locally from HCO_3, rather than exclusive reliance on the diffusion of additional CO_2 from bulk fluid outside the boundary layer. Using this approach CO_2 removal from blood was improved by 37% [7, 8]. This approach has promise in combination with active mixing as is explored in Chapter 6.0.

Controlled addition of acidic species to blood has also been shown to improve CO_2 removal rates in artificial lungs by taking advantage of the blood buffering system, which forces

conversion of some bicarbonate ion to CO_2 in order to regulate pH. This spike in pCO_2 increases the driving gradient for elimination by hollow fiber membranes. This approach has been explored through whole blood acidification using naturally occurring lactic acid [86, 87] and by mixing acidic SO_2 gas into the fiber sweep gas to introduce acidic species directly at the fiber surface [85]. CO_2 removal enhancement is promising but these approaches present several technical challenges and are still experimental. An approach for decarbonation through electrodialysis has been reported as well, where an electrical field is applied to blood to selectively modulate pH and electrolyte concentrations [88]. CO_2 removal rates were improved by 75% during acute testing in pigs through electrodialysis, however blood electrolyte concentrations were affected by the treatment and the approach adds significant complexity to the gas exchange circuit.

1.4.5 Objectives for Minimally Invasive CO_2 Removal

Significant progress in $ECCO_2R$ has been made, but improvements are necessary to provide simple, safe, effective, and minimally invasive respiratory support at low-blood flow rates. Recognizing the potential for advancement in this area, this project also explores the efficacy of utilizing the rotating impeller technology from the IPRAC for an extracorporeal device. The design objectives for an $ECCO_2R$ device are:

1. CO_2 removal rates equivalent to 25-35% of the metabolic CO_2 production ($\geq$65 mL/min) at normocapnia ($pCO_2 \approx 45$ mmHg) and dialysis blood flow rates (250 mL/min).
2. Minimally invasive cannula (< 15 Fr).
3. In vitro hemolysis levels comparable to a gas exchange circuit of commercially available components.

The gas exchange and hemocompatibility objectives for an $ECCO_2R$ device are comparable to those for a respiratory assist catheter. The target insertion diameter for cannula in an external circuit are less than for an intravenous device however, since the increased size is considered an appropriate tradeoff for the simplicity and lack of external circuitry with an insertable device.

Our goal is to advance previously explored approaches for highly efficient CO_2 removal for use in an intravascular or extracorporeal device that enables minimally invasive partial respiratory assistance. This thesis describes the continued development of the IPRAC and initial design, fabrication, and testing of a new extracorporeal device that utilizes the IPRAC impeller technology for minimally invasive $ECCO_2R$. Chapter 2.0 and 3.0 focus on evaluation of new IPRAC impeller designs and arrangements on gas exchange and hemocompatibility. To investigate the potential for the impeller concept in alternative artificial lung applications, Chapter 4.0 presents the results of feasibility experiments for an IPRAC design modified for extracorporeal use at ultra-low blood flows, characteristic of renal hemodialysis. Chapter 5.0 builds on the development of an ultra-low-flow $ECCO_2R$ device (ULFED) through redesign of the feasibility prototype tailored for extracorporeal use. New design parameters were identified and evaluated for in vitro gas exchange and hemolysis. Finally, Chapter 6.0 reports the results of feasibility testing of combining mechanical and enzymatic approaches for enhancing CO_2 removal, where CA immobilized fibers are incorporated into an impeller active mixing device.

2.0 EFFECT OF IMPELLER DESIGN AND SPACING ON GAS EXCHANGE IN A PERCUTANEOUS RESPIRATORY ASSIST CATHETER

The following chapter presents work peer-reviewed and published in the journal Artificial Organs [91]. *Computational fluid dynamics (CFD) modeling was conducted by Dr. Greg Burgreen, PhD, at the University of Mississippi. Methods, results, and discussion specifically pertaining to that work can be found in the above reference. Noteworthy discussion from the modeling analysis is included in the sections below.*

2.1 INTRODUCTION

The benefit of providing partial respiratory support (CO_2 removal) for patients with acute hypercapnic respiratory failure has been demonstrated with extracorporeal CO_2 removal ($ECCO_2R$) devices [92, 93]. Similar to extracorporeal membrane oxygenators (ECMO), $ECCO_2R$ systems utilize microporous hollow fiber membranes (HFMs) to remove CO_2 and add oxygen (O_2) to the blood [94–96]. By these means, $ECCO_2R$ performs respiratory function independent of the pulmonary system, allowing the injured lungs to rest and heal. Partial respiratory support can prevent the need for invasive mechanical ventilatory (IMV) treatment in patients with acute exacerbations of chronic obstructive pulmonary disease (COPD) and allows low tidal volume lung protective ventilation (LPV) strategies to be utilized in the treatment of

acute respiratory distress syndrome (ARDS) [25, 28]. Concerns with $ECCO_2R$ are similar to those of traditional ECMO however, in that blood loop and equipment management can be highly complicated. Some emerging $ECCO_2R$ systems are comparatively less complex to operate [2, 7], but all still depend on passage of blood through an external flow loop and generally have a high surface area of synthetic material directly in contact with blood [97].

Several groups have previously or are currently investigating the development of an intravenous device for partial respiratory support [43, 44, 46, 56, 62, 98]. All of these devices use HFMs as in ECMO/$ECCO_2R$, but instead of removing blood from the body in an external circuit, intravenous devices are inserted percutaneously into the venous system (generally the inferior vena cava, IVC). As a result, intravenous respiratory assist devices also have the advantage of performing respiratory function independent of the lungs, allowing the injured pulmonary tissue to rest and heal. In contrast to ECMO/$ECCO_2R$ however, the complexities associated with blood flow loops and circuit management are eliminated along with the high blood-contacting surface area. Intravenous devices also do not require a circuit blood pump and have the benefit of performing gas exchange on systemic blood flow through the IVC (≈2/3 cardiac output), whereas blood availability for gas transfer in extracorporeal devices is limited by circuit blood flow. The greatest challenge in development of this technology is achievement of sufficient gas transfer with the limited gas exchange surface area that can be incorporated into a device that functions within the venous system while minimizing insertion size [97]. Early intravenous devices achieved CO_2 removal rates up to 40-70 mL/min [99, 100] and reached human clinical trials [42], but concern surrounded the large diameters (32-50 Fr), which required specialized surgeons for insertion [42, 55, 58]. To eliminate the need for surgical insertion we are seeking to develop an intravenous device with an insertion diameter of 20-25 Fr. A promising approach we are

investigating to achieve this was first presented by Mihelc et al., which consists of a slender HFM bundle surrounding an array of rotating impellers to generate an "active mixing" effect [5]. Active mixing improves mass transfer by increasing blood velocity across gas exchange surfaces, which diminishes the highly limited diffusive boundary layer at the membrane surface and prevents blood-side accumulation of oxygen and depletion of carbon dioxide at the membrane surface [101]. This maintenance of a strong gas partial pressure differential across the membrane promotes efficient gas exchange. The impeller percutaneous respiratory assist catheter (IPRAC) achieved CO_2 removal rates up to 529 ± 20 mL/min/m^2 on the bench with a total fiber surface area of 0.07 m^2, for a total removal rate of 36 mL/min during pilot studies [5]. Earlier work focused primarily on characterizing the relationship between rotation rate and gas exchange, as well as evaluation of eight different impeller designs. Not surprisingly, gas exchange correlated directly with rotation rate, and maximum CO_2 removal rates were achieved at the highest rate tested (20,000 RPM) [5]. A strong dependence of gas exchange on impeller design was also observed. The top performing design achieved exchange rates over twice that of the lowest performer. Recognizing the potential for further improvement to gas exchange, the objective of this work was to combine bench work and computational fluid dynamics (CFD) to develop and evaluate several new impeller designs for the IPRAC. We additionally investigated the effects on gas exchange of features such as axial spacing between impellers and number of blades.

2.2 METHODS

2.2.1 Device Description

The IPRAC prototype (Figure 2.1A) consists of an array of impellers fixed to a flexible stainless steel driveshaft (0.042" (1.07 mm) diameter) (SS304V, Heraeus Medical Components, St. Paul, MN) that rotate concentrically within a stationary stainless steel coil (inner diameter 5 mm). 250 polypropylene (PP) fibers (x30-240; Membrana Celgard, Wuppertal, Germany) are wrapped around the outside of the coil, preventing direct contact between impellers and fibers (Figure 2.2B). Individual fibers have outer diameters of 300 μm and measure 30 cm in length, for a total membrane surface area of 0.07 m^2. The flexible driveshaft extends out of the fiber bundle through the medial manifold where it connects to an external DC brushless servomotor (2444-024B; MicroMo Electronics Inc., Clearwater, FL) at the proximal manifold. To prevent backflow of fluid up the driveshaft tubing, an infusion line continually pumps fluid at 15 ml/hr down the driveshaft tube toward the medial manifold where it exits the device into the recirculating loop. The sweep gas pathway in the full IPRAC prototype incorporates both the inlet and outlet gas ports in the proximal manifold, permitting percutaneous insertion to the inferior vena cava via the femoral vein (Figure 2.1B). Sweep gas enters the inlet port and flows directly into the fiber bundle at the medial manifold. Sweep flow exits the fiber bundle in the distal manifold, where it enters separate tubing integrated into the fiber bundle that returns it to the gas outlet port in the proximal manifold. This return gas pathway consists of wire reinforced polyimide tubing (MinVasive Components, Trenton, GA). This design is different from that described by Mihelc et al., which used a hollow driveshaft tube to return the sweep gas from the distal to proximal

manifold. This modification allows the diameter of the impeller driveshaft to be significantly reduced versus previous prototypes.

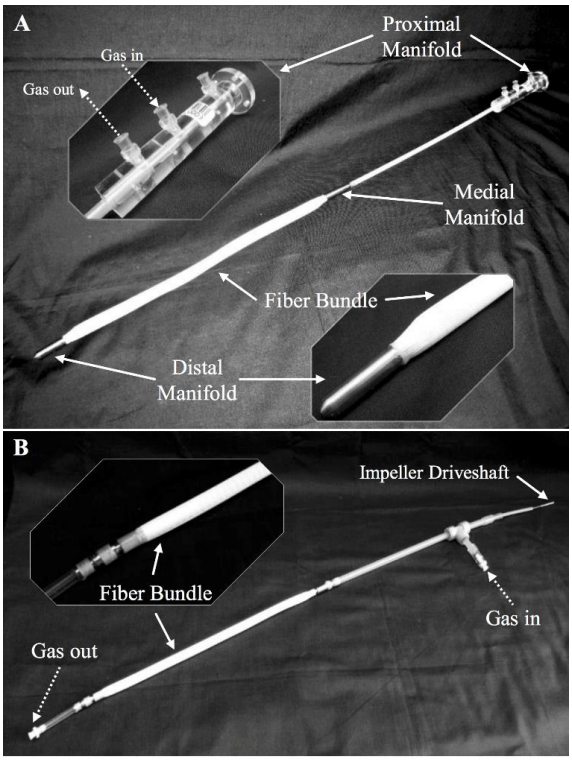

Figure 2.1. IPRAC and Modified IPRAC prototypes. (A) Full IPRAC prototype with gas inlet and outlet at the proximal manifold. (B) Modified IPRAC used for in vitro CO_2 removal from water with distal manifold sweep gas outlet port and interchangeable impeller driveshaft.

In this work a modified IPRAC device (Figure 2.1B) was used to evaluate gas exchange of each impeller. In vitro testing does not require percutaneous insertion, so the gas pathway was

configured to allow sweep gas to exit directly from the distal manifold, thereby eliminating the need for return gas pathway tubing. The modification also allowed the impeller driveshaft to be easily interchanged. This enabled the use of the same fiber bundle for all testing, thereby eliminating a potential source of variability. The sweep gas pressure at the fiber bundle inlet is consistent in both gas pathway designs, so the modification has no effect on resulting gas exchange.

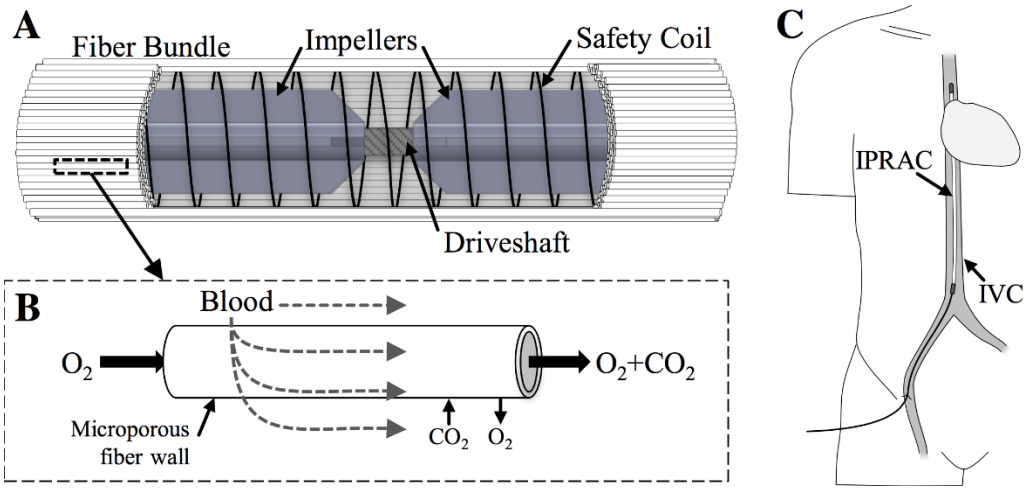

Figure 2.2. IPRAC indwelling impellers, blood/gas pathways, and vascular placement. (A) Tear-away view of IPRAC fiber bundle showing indwelling safety coil and impellers on driveshaft. (B) An enlarged view of sweep gas versus blood pathways in a single HFM. Pure O_2 gas flows into the fiber lumen and an O_2 + CO_2 gas mixture exits at fiber outlet. Blood flows on the outside of the fiber, separated from sweep gas flow by the microporous fiber wall. (C) IPRAC insertion to the inferior vena cava (IVC) via the femoral vein with percutaneous gas pathway and driveline tubing.

Following initial testing, the impellers with greatest CO_2 removal rates in the modified IPRAC were incorporated into full IPRAC prototypes for gas exchange evaluation.

2.2.2 Impellers

All impellers were designed in SolidWorks (Concord, MA) and fabricated at the University of Pittsburgh Swanson Center for Product Innovation (Pittsburgh, PA) from a hydrophobic epoxy resin (Watershed XC11122; DSM Somos, Sittard, Netherlands) using stereolithography (SLA). Impellers measured 10 mm in length with a maximum outer diameter of 4 mm. The reduction in driveshaft diameter from 0.090" (2.3 mm) in previous work to 0.042" (1.07 mm) allowed design of taller blades with increased surface area. The six impeller blade designs evaluated are shown in Figure 2.3. The Flat Blade design is similar to the top performing geometry from previous work but has 3-fold increased blade surface area to enhance potential fluid volume displacement. Each of the Curved, Flat-Tangent, and Radial-Tangent blades (where the Radial-Tangent design is a combination of the Curved and Flat-Tangent blades) were designed with the objective of minimizing the change in velocity vector directionality of incident flow. The Crescent blade was designed to funnel flow toward the center of the impeller, with the objective of focusing generated flow to a single region on each blade. All impellers had 2-5 blades. Impellers were glued to the distal 280 mm of flexible drive shafts. Axial separation distance between impellers was set at 2 or 10 mm, resulting in a total of 23 or 14 impellers, respectively.

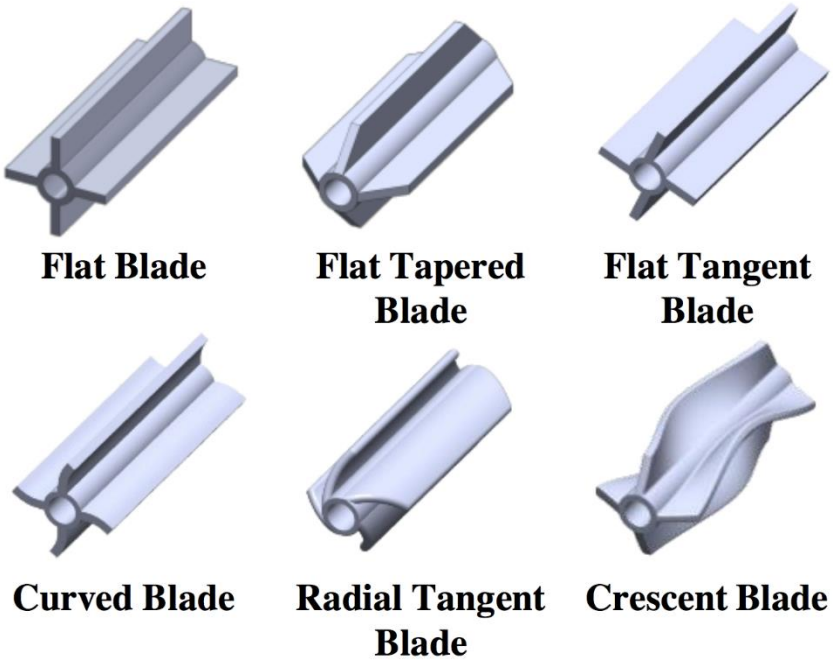

Figure 2.3. IPRAC impeller designs. Six impeller geometries evaluated in in vitro gas exchange studies. Each impeller measures 10 mm in length with maximum outer diameter of 4 mm.

The design of blades and determination of the optimal combination of blade design, axial spacing, and number of blades was a progressive process. The Flat, Flat-Tangent, Curved, and Flat-Tapered impellers were designed and tested first with 4 blades and 10 mm axial separation. As design characteristics and arrangements were shown experimentally and in CFD simulations to be beneficial, or not, for gas exchange (e.g. axial separation, 45° taper on blade ends, etc.), these features were selectively implemented into later designs (i.e. Radial-Tangent and Crescent blades). As a result, not all designs were tested with varying number of blades or at multiple axial separation distances. The combinations of blade number and impeller spacing for the geometries tested are listed in Table 2.1.

Table 2.1. Design matrix of IPRAC blade parameter combinations evaluated in vitro.

Blade Design	With 10-mm spacing (14 impellers)	With 2-mm spacing (23 impellers)
Flat	4 blades only	4 blades only
Flat-Tapered	4 blades only	3, 4, or 5 blades
Flat-Tangent	4 blades only	—
Curved	4 blades only	—
Radial-Tangent	—	2, 3, or 4 blades
Crescent	—	3 or 4 blades

2.2.3 In Vitro Flow Loop and Gas Exchange Testing

Gas exchange testing was performed in an in vitro recirculation loop (Figure 2.4), as described by Eash et al. [58]. The loop consisted of a reservoir, centrifugal pump (BPX-80; Medtronic, Minneapolis, MN), two commercial oxygenators (Vision Hollow Fiber Oxygenator; Gish Biomedical, Rancho Santa Margarita, CA) to control inlet CO_2 gas tension, and the modified IPRAC device within a 7/8-in ID acrylic test section. Pure O_2 sweep gas was pulled through the fiber bundle at 3.0 L/min by a sealed vacuum pump (N811 KV.45P; KNF Neuberger Inc., Trenton, New Jersey) and regulated with a thermal mass flow controller (GR-116-1-A-PV-O_2; Fathom Technologies, Georgetown, Texas). Pressure drop across the fiber bundle was monitored with differential transducers (143C; Honeywell International, Inc., Morristown, NJ). We have shown previously that measured CO_2 removal in water bench testing correlates well with in vivo performance (within ≈10%) for IPRAC devices, so for simplicity all testing was performed in deionized water at 37°C [5, 101]. Water flow rate was maintained at 3.0 L/min in the loop and monitored with a clamp-on ultrasonic flow probe (Transonic Systems Inc., Ithaca, NY). Water pressure at the test section inlet was measured with a liquid pressure transducer (PX771-025DI;

Omega Engineering Inc., Stamford, CT) and maintained at physiologically relevant venous pressures (10-15 mmHg).

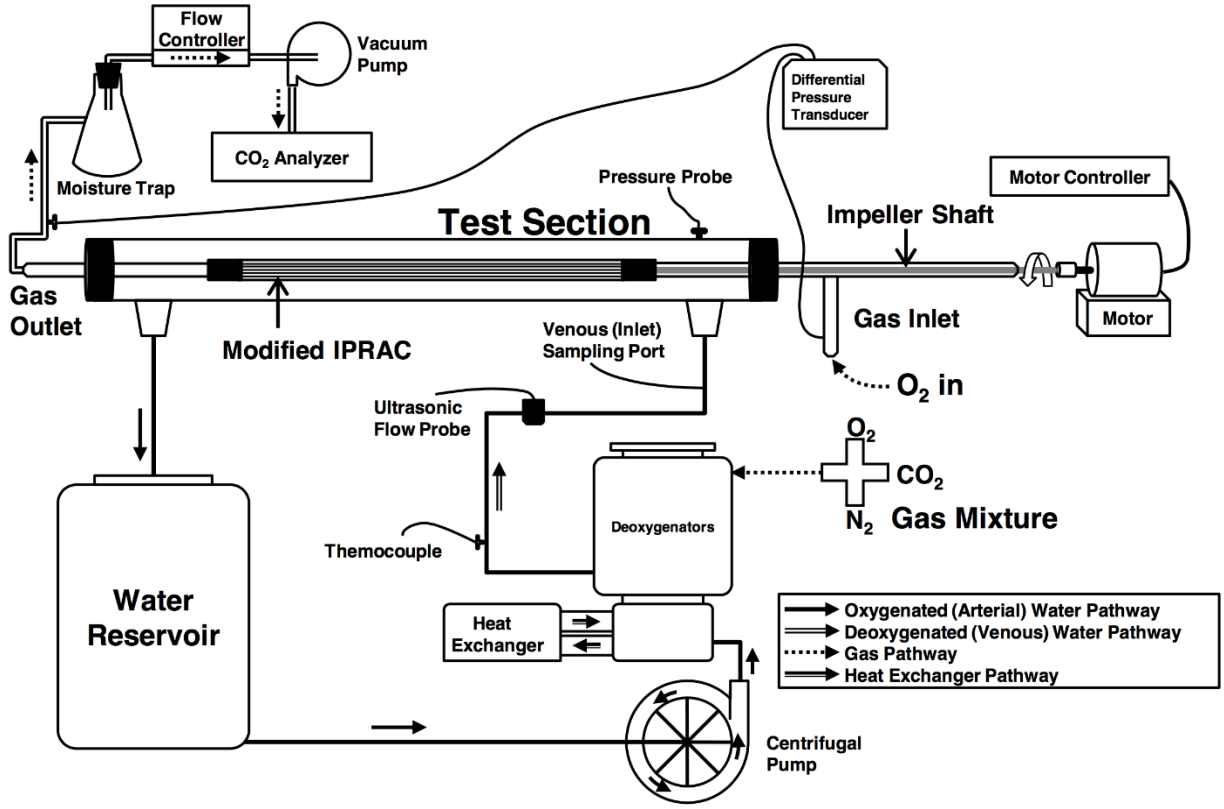

Figure 2.4. IPRAC in vitro gas exchange loop.

The CO_2 and O_2 gas tensions in the fluid were measured with a blood gas analyzer (RapidLab 248; Siemens, Erlangen, Germany). Inlet pCO_2 was adjusted to conditions relevant to venous blood (pCO_2 = 50 ± 5 mmHg) via a CO_2/N_2 gas mixture through commercial

oxygenators. The outlet sweep gas CO_2 concentration was measured with a gaseous CO_2 analyzer (WMA-4; PP Systems, Amesbury, MA). Inlet O_2 partial pressure was not regulated but was typically steady around 25 ± 10 mmHg.

Gas exchange was evaluated for each impeller rotating at 20,000 RPM. The fraction of CO_2 in the outlet gas was used to calculate total CO_2 removal, V_{CO_2}, according to Equation 2.1, as the product of the fraction of CO_2 exiting the fibers, F_{CO_2}, and the STP corrected mass flow rate of the sweep gas, Q_{OUT}^{STP}.

$$V_{CO_2} = Q_{OUT}^{STP} F_{CO_2} \quad 2.1$$

To reduce variability associated with small differences (< 5 mmHg) between trials, $\boldsymbol{V_{CO_2}}$ was then normalized $\left(\boldsymbol{V_{CO_2}^*}\right)$ to our target inlet pCO_2 of 50 mmHg according to Equation 2.2.

$$V_{CO_2}^* = V_{CO_2} \cdot \frac{50\ mmHg}{pCO_2^{INLET}} \quad 2.2$$

2.2.4 Statistical Analysis

Reported gas exchange values are the average of 6-8 measurements each. Significance testing was performed in SPSS (PASW Statistics 18; IBM, Armonk, NY). Student's or paired t-tests and ANOVA were conducted with subsequent posthoc testing when all assumptions for parametric testing were satisfied. Assumptions required for parametric analysis include: 1) homogeneity of variance (i.e. homoscedasticity) as determined by Levene's test, 2) normally distributed data (Kolmogorov-Smirnov test), and 3) equal group sample sizes. With violation of the first assumption, or if both the second and third assumption were violated, the non-parametric Kruskal-Wallis test was used in place of ANOVA. Non-parametric posthoc comparisons of

means were conducted with the Mann-Whitney U test coupled with a Bonferroni correction to avoid inflation of a Type I (false positive) error rate.

2.3 RESULTS

2.3.1 Spacing Effects

The Flat and Flat-Tapered blades were each tested side-by-side with 2 mm and 10 mm axial separation to investigate spacing effects on gas exchange efficiency. A small (5-10%) improvement in CO_2 removal rate ($p<0.005$) was achieved at 2 mm separation for both geometries tested (Figure 2.5A). Normalizing the gas exchange rate to the number of impellers (Figure 2.5B) showed that reducing the separation gap resulted in a 35% (Flat blade) and 28% (Flat-Tapered blade) decrease in gas exchange per impeller.

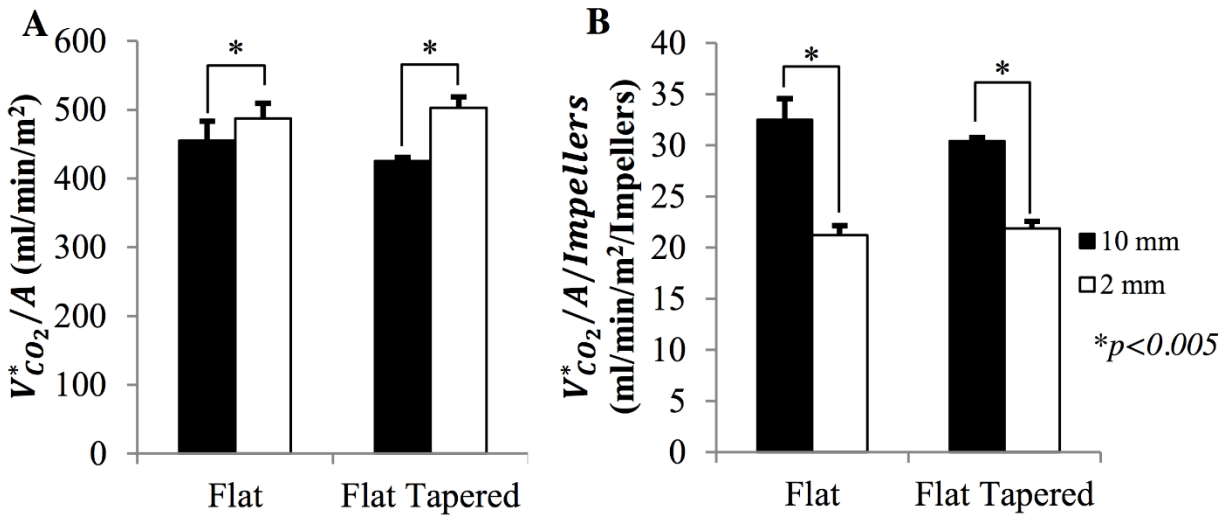

Figure 2.5. Impeller Spacing effects on IPRAC gas exchange. All impellers were fixed to a 270 mm section of driveshaft at either 2 mm or 10 mm axial spacing between impellers. At the shorter (2 mm) and longer (10 mm) axial separation distances 14 and 23 impellers were attached in total, respectively. Plots show CO_2 removal rates of Flat and Flat-Tapered impellers (with 4 blades) at both 2 and 10 mm axial spacing with normalization for (A) fiber surface area, $\boldsymbol{V^*_{CO_2}/A}$, mL/min/m^2 or (B) fiber surface area and number of impellers, $\boldsymbol{V^*_{CO_2}/A/Impellers}$, mL/min/m^2/Impellers.

2.3.2 Comparison of Impeller Blade Designs

Six unique impeller designs were compared with either 10 mm (Figure 2.6A) or 2 mm (Figure 2.6B) axial separation with four blades each. Due to the progressive nature of the testing process, not all designs were evaluated at both 10 and 2 mm separation. The Curved and Flat-Tangent

blades were not shown to significantly affect gas exchange versus the Flat blade at 10 mm separation, so were not tested later at 2 mm separation after it was determined the shorter axial spacing was beneficial. The Radial-Tangent and Crescent blades that were designed last were only tested at the more advantageous 2 mm separation distance. The Curved and Flat-Tangent blades outperformed the Flat-Tapered blade in gas exchange testing by a small (5-8%) but statistically significant ($p<0.005$) margin. No other designs were found to differ statistically with 10 mm separation, however comparison of Flat to the Flat-Tapered failed to meet the required p-value by a small margin ($p=0.009$, but required p-value from Mann-Whitney non-parametric comparison of means with Bonferroni correction was $p<0.0083$). Statistical comparison of means found the measured CO_2 removal data for the Flat, Flat-Tapered, Radial-Tangent, and Crescent blades (2 mm axial spacing) to differ insignificantly ($p=0.072$), suggesting no statistical difference exists between these designs.

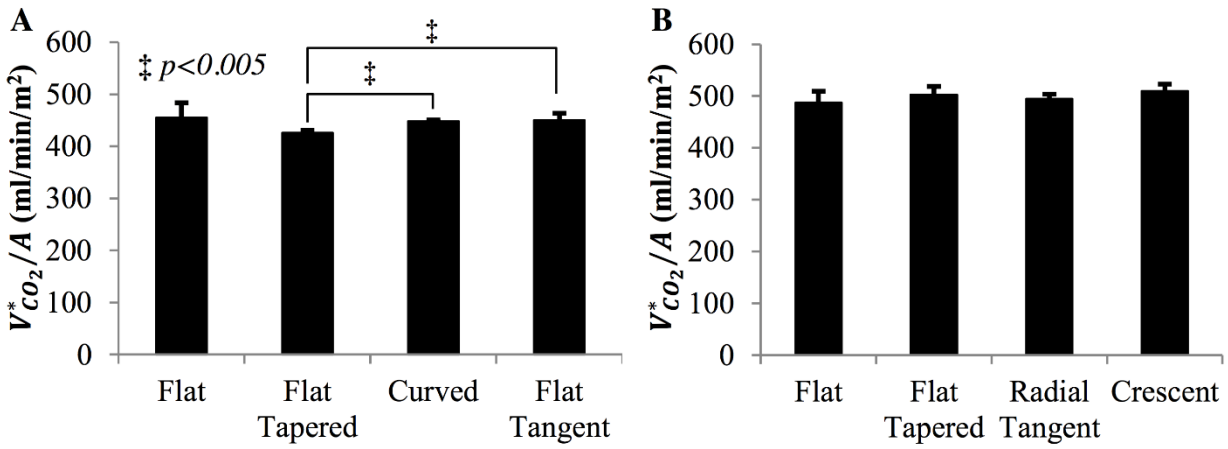

Figure 2.6. Effect of IPRAC blade design on gas exchange. CO_2 removal rate normalized to fiber surface area (0.07 m^2) of six impeller designs, each with 4 blades. (A) Data shown for impellers with 10 mm axial separation. (B) Data shown for impellers with 2 mm axial separation.

The 45° chamfer (taper) that distinguishes the Flat and Flat-Tapered designs was not shown to affect gas exchange experimentally at either 2 mm or 10 mm separation. Since no disadvantage in gas exchange was demonstrated for the tapered blade modification, this feature was incorporated into blades designed after that finding (i.e. Crescent and Radial-Tangent).

2.3.3 Number of Blades

Three designs (Flat-Tapered, Radial-Tangent, and Crescent) were each tested with varying number of blades (Figure 2.7). The achievable gas exchange rates with the Flat-Tapered and Crescent impellers were both found to be independent of the number of blades in head-to-head comparisons (p=0.24 and p=0.97, respectively). Only the Radial-Tangent impellers achieved

statistically differing gas exchange rates (p=0.01). CO_2 removal rates of the Radial-Tangent design with two blades were 5% (p=0.006) and 4% (p=0.015) less than the same design with three-blade and four-blades, respectively. While gas exchange rates were shown to differ statistically for one design with varying numbers of blades (Radial-Tangent), the overall effect for all devices tested was marginal (~0-5%).

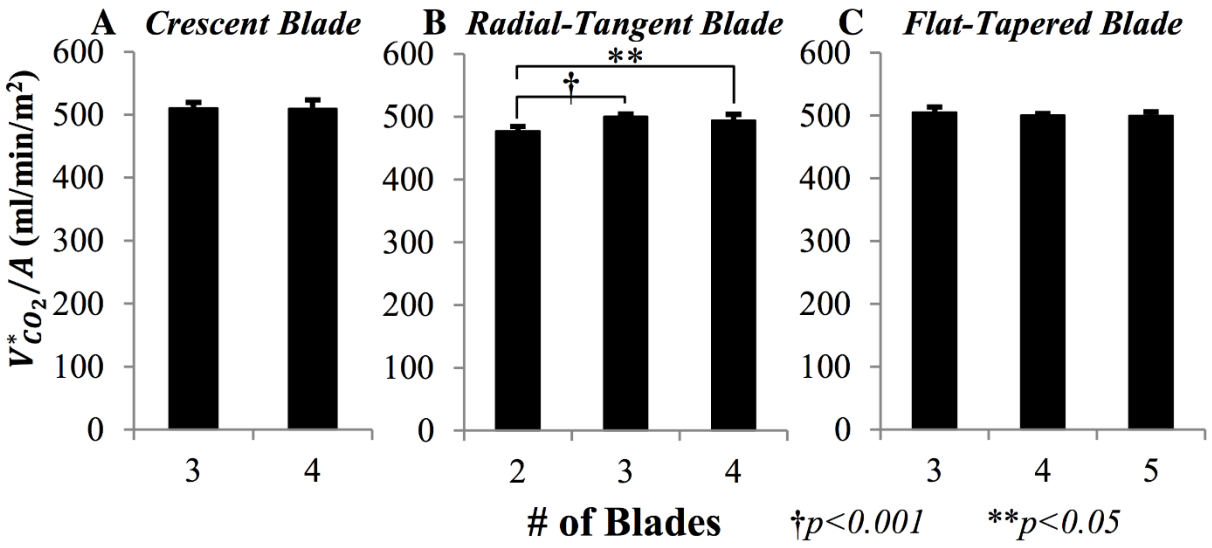

Figure 2.7. Effects of blade frequency on IPRAC gas exchange. CO_2 removal rate normalized to fiber surface area (0.07 m^2) versus blade number on impellers with (A) Crescent blades, (B) Radial-Tangent blades, and (C) Flat-Tapered blades. Each impeller device had 2 mm axial separation. *†p<0.001, **p<0.05.*

2.3.4 Full IPRAC Prototype Gas Exchange Testing

Following in vitro gas exchange testing with the modified catheter device, full IPRAC prototypes were manufactured that incorporated impellers with either the Crescent, Flat-Tapered, or Radial-Tangent blades. Each device consisted of impellers with three blades and 2 mm axial spacing. The gas exchange performances of the full IPRAC devices are shown in Figure 2.8. The highest CO_2 removal rate (573 ± 8 mL CO_2/min/m^2) was achieved with the Crescent blade, followed by the Flat-Tapered (535 ± 17 mL CO_2/min/m^2) and the Radial-Tangent (516 ± 7 mL CO_2/min/m^2) prototypes. With the exception of the Crescent blade that achieved 11% greater CO_2 removal in a full IPRAC device versus the modified catheter, the gas exchange data generally agreed between full and modified IPRAC devices. In full prototypes the Flat-Tapered and Radial-Tangent blades performed 6% and 3% greater than in testing with the modified device.

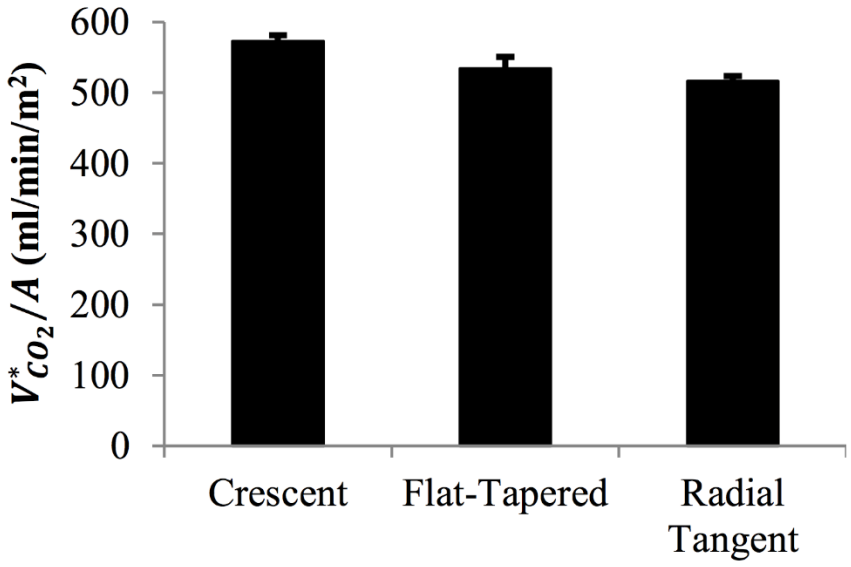

Figure 2.8. CO_2 removal rates of full IPRAC prototypes. Prototypes contained either Crescent, Flat-Tapered, or Radial-Tangent blade designs. Each impeller contained 3 blades and was separated axially by 2 mm.

2.4 DISCUSSION

In vitro testing demonstrated that CO_2 removal achieved with impeller rotation was improved by reducing axial spacing and increasing the total number of rotating impellers. The design of the blade as well as the number on each impeller was not found to significantly influence gas exchange. Our top performing impeller arrangement achieved a CO_2 removal rate of 573 ± 8 mL/min/m^2 (40.1 mL/min) in a full IPRAC device, an improvement of ~10% versus previous work [5].

The mechanisms by which an actively mixed system can facilitate HFM mediated gas exchange in blood oxygenators has been described previously [51, 101–103]. In short, impeller rotation adds orthogonal velocity components to bulk movement in the vessel, resulting in cross-flow through the fiber bundle and increased fluid velocity at the membrane surface. Greater velocity and bundle cross-flow diminish the highly limiting diffusive boundary layer at the gas exchange surface, facilitating maintenance of stronger gaseous concentration gradients spanning fiber walls [51]. The significance of this enhancement is emphasized when considering the effect of impeller facilitated active mixing on the mass exchange effectiveness parameter. The ratio (~0-1) of achieved CO_2 removal versus maximum possible removal normalized for blood flow rate, gas flow rate, and pCO_2^{INLET}, increases >15-fold from 0.012 to 0.203 with impeller rotation at 20,000 RPM versus passive gas exchange (i.e. 0 RPM) [104].

Among potential factors contributing to gas exchange, our results suggest that indirect and direct interactions between neighboring impellers are of importance. When axial separation distance is reduced from 10 mm to 2 mm, the length of the fiber bundle associated with each impeller (i.e. bundle length/# impellers) decreases by 40%. We believe the CO_2 removal efficiency of each impeller (i.e. $V_{CO_2}^*/A/Impellers$) with 2 mm axial spacing is affected by the reduced bundle surface area associated with each impeller. Figure 2.9 shows CFD predicted velocity profiles in fluid surrounding impellers and the flow pathways of fluid as affected by rotating impellers. Above each rotor, fluid is strongly propelled radially outward through the fiber bundle before recirculating inward back through the bundle in the space between impellers. As the distance between impellers shrinks, the resistance to inward flow increases, reducing the pumping efficiency of each impeller and the associated contribution to gas exchange. In simulations we demonstrated that a 45° chamfer (taper) at the blade ends mitigated this

interference and diminished the losses in efficiency for individual impellers at 2 mm versus 10 mm spacing (22% predicted improvement in CO_2 removal at 2 versus 10 mm for Flat-Tapered, 16% for Flat). Predicted gas exchange performance versus each experimental dataset are shown in Figure 2.10. Experimentally the 45° chamfer did not significantly affect overall gas exchange (i.e. the Flat and Flat-Tapered did not differ statistically at 2 mm spacing or at 10 mm spacing) but the improvement in total CO_2 removal at 2 versus 10 mm spacing for the Flat-Tapered blade (18%) exceeded that of the Flat blade (7%). The effects of the blade taper are logically not inclusive of gas exchange, and could possibly contribute a hemocompatibility advantage as well given that attenuating flow interference may lessen stresses exerted on blood cells. Given that our overall gas exchange improved with 23 versus 14 impellers despite the 28-34% reduced contribution of individual impellers, we proceeded with testing of new blade designs (Crescent and Radial-Tangent) exclusively at 2 mm spacing. Considering the potential benefits to gas exchange and hemocompatibility each was designed with a 45° taper at the end of each blade.

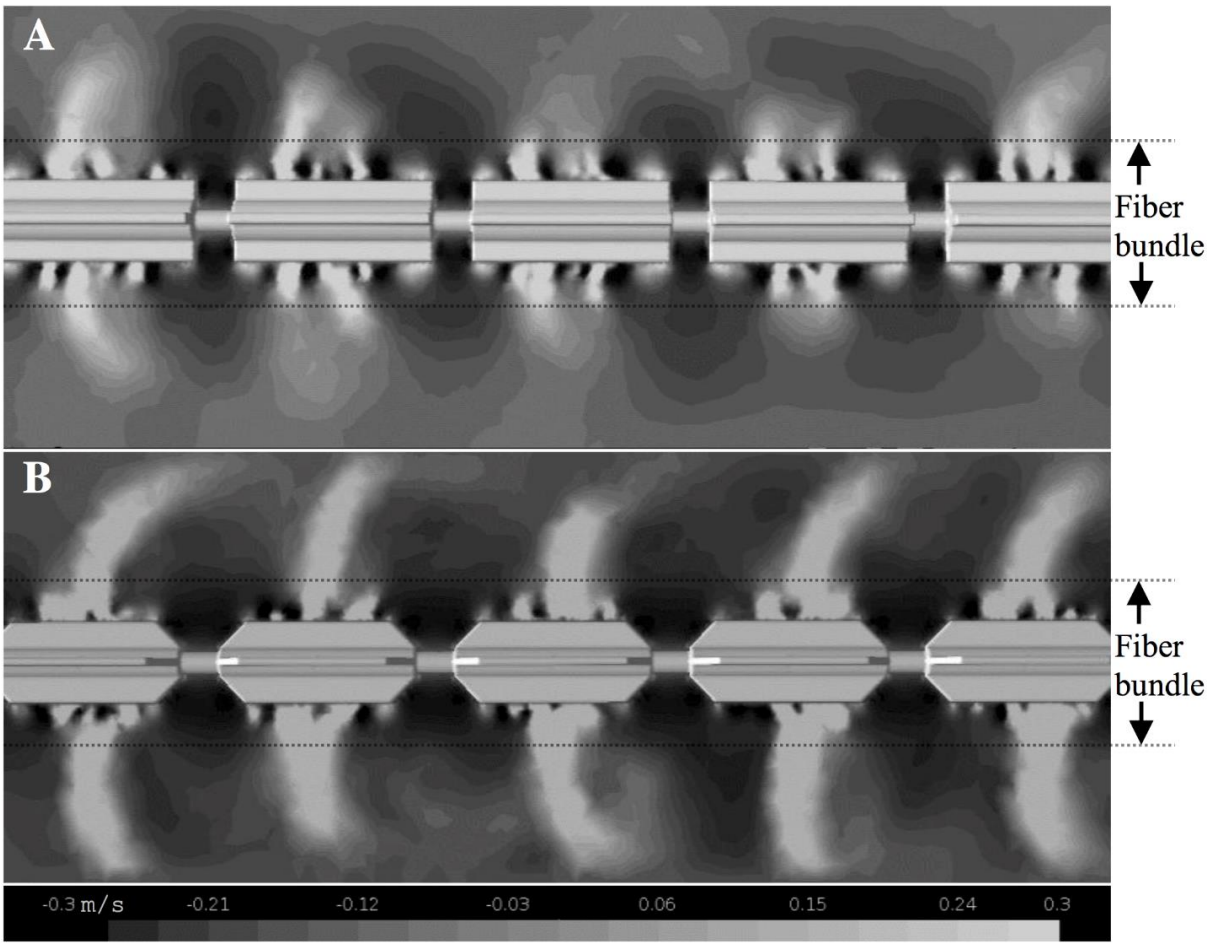

Figure 2.9. CFD predicted fluid velocities in the IPRAC with impeller mixing. 3 L/min of bulk flow from left to right. Light and dark contour regions correspond to fluid velocity (in m/s) in positive radial direction (away from shaft) and negative radial direction (toward the shaft), respectively. (A) Flat blade 2 mm spacing (B) Flat-Tapered blade at 2 mm axial spacing.

Each impeller chosen for testing in full IPRAC prototypes was fabricated with three blades. The failure to show any significant effect of blade number on gas exchange for the designs tested suggests that only a few impeller blades provide the necessary orthogonal velocity

components required to create efficacious active mixing conditions. We also theorized that additional blades would exert additional shear stresses and viscous energy dissipation to the fluid. Given the conceivable advantage to hemocompatibility and equivalent contribution to gas exchange, we concluded that incorporating more than three blades was inessential. The discrepancy in performance between the modified and full IPRAC devices containing the same impellers/arrangements may be due in part to the manufacturing process, given that the fiber bundle is wrapped and potted for each device by hand.

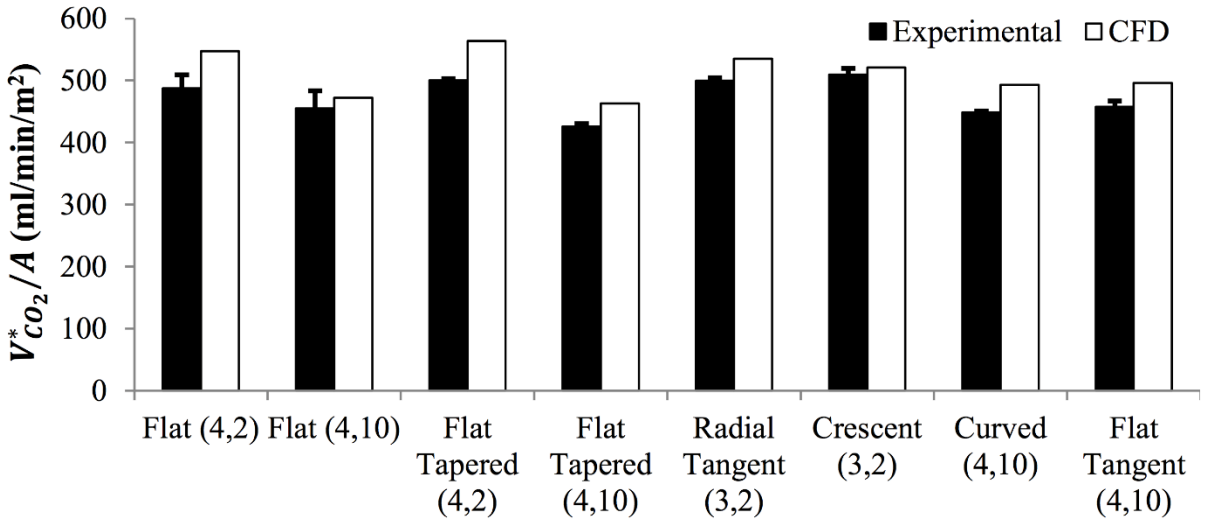

Figure 2.10. CFD predicted versus experimental gas exchange rates in the IPRAC. CO_2 removal rates normalized to fiber surface area (0.07 m^2). *Group nomenclature: Impeller Name (Number of blades, Impeller separation distance in mm).*

The CFD simulation model developed for the IPRAC in collaboration with Dr. Burgreen was valuable for flow visualization and drove our progressive design process. Formal optimizations of impeller blade designs were not conducted however. A limitation of developing a CFD model for a complex flow system such as the IPRAC is that not all nuances of device operation can be captured with exact fidelity. For example, the use of a non-rigid driveshaft that provides the IPRAC with the necessary flexibility for insertion and operation in tortuous environments does not prevent radial impeller movement within the safety coil. It is possible that operational subtleties such as this affect resulting gas exchange non-negligibly, but would be far too complex to accurately predict in a CFD model. Despite this, the error associated with our gas exchange model was reasonably acceptable (2-13%), and accurately predicted the overall benefits of reducing impeller axial spacing, which we demonstrated to be the most influential parameter investigated. This finding suggests that our model may be beneficial for identifying design features and impeller arrangements that profoundly influence gas exchange in future studies.

Rotation speed remains an important factor in active mixing, as was shown for all geometries tested previously [5]. Other possible design parameters or arrangements that may contribute to gas exchange that were not investigated in this work are impeller length or driveshaft orientation relative to other impellers (i.e. aligned with blades offset to neighboring impeller). Collectively though these results suggest that at constant impeller rotation rates, we may expect little further improvement in gas exchange with optimization of impeller blade designs and arrangements.

The resulting CO_2 removal rate of the IPRAC after investigation of impeller arrangements and design is ~2/3 of the target rate of ≥65 mL/min. We hypothesized that

improvements to the impeller design would enable reduction of the insertion diameter from the current 25 Fr to a more clinically relevant diameter <20 Fr. Due to the modest improvement in total gas exchange performance it is not feasible with the current IPRAC design to reduce the device diameter. Decreasing the IPRAC insertion size would require a combination of reducing the HFM surface area and reducing impeller blade size, both of which are expected to negatively impact gas exchange performance. A potential method of improving gas exchange would be incorporation of carbonic anhydrase (CA) immobilized fibers. This approach was shown to enhance CO_2 removal by 37% in blood [7]. The combination of CA-fibers and active mixing may have an additive or synergistic effect on CO_2 removal. Recent studies, however, suggest the CA fibers may be most effective at blood flow rates significantly lower than those relevant to the IPRAC (<500 mL/min) [84]. This topic is further discussed in Chapter 6.0.

3.0 IPRAC IN VITRO HEMOLYSIS TESTING

3.1 INTRODUCTION

Blood cell hemolysis refers to the rupture of erythrocytes in blood and dispensing of cellular contents into the plasma. This is a naturally occurring process as red blood cells age and lyse, however in the presence of blood contacting devices this process can be expedited due to mechanical trauma. Plasma free hemoglobin (pfHb) is generally eliminated from the plasma by conjugating with α-2-globulin to form a haptoglobin complex before reticuloendothelial clearance, however this pathway is exhausted at plasma hemoglobin concentrations exceeding ~130-150 mg/dL [105, 106]. High concentrations of hemoglobin in the plasma can result in deposition into body tissues, hemoglobinuria, and can eventually lead to endothelia cytotoxicity and excessive nitric oxide scavenging [107–109].

Hemocompatibility studies are of special interest for the impeller percutaneous respiratory assist catheter (IPRAC) since hemolysis is often associated with shear due to rotating parts, narrow clearances, and mechanical components necessary in these systems (e.g. bearings, seals) in blood pumps [110–113]. A systematic approach to determine the relationship between in vitro hemolysis and active mixing was undertaken to identify components of the impeller system that may contribute to hemolysis.

The objectives of the hemolysis studies reported in this chapter were to establish if specific aspects of the IPRAC design contributed to erythrocyte trauma. Hemolysis tests focused on five aspects of the IPRAC design that we suspected may contribute to cell damage based on reports from the blood pump literature [110–114]. (1) Impeller rotation, (2) contact between impellers and the surrounding safety coil, (3) surface roughness of impellers, (4) flow through the fiber bundle, and (5) contact between the rotating shaft and static components were each investigated independently. Modified IPRAC prototypes were designed and fabricated to evaluate each potential source of cell damage. Hemolysis associated with each design component was estimated by comparison of a modified IPRAC device versus the same device with that specific component removed. Impellers were found to contribute to minimal hemolysis in the absence of the surrounding safety cage. Contact between the impellers and the surrounding cage was found to account for the majority of cell damage observed in the IPRAC. When impeller surfaces were polished however, hemolysis associated with impeller/cage contact was largely eliminated, indicating surface roughness played a major role in contact-trauma between the impellers/cage. All other sources of cell damage investigated were found to contribute to minimal hemolysis.

3.2 METHODS

3.2.1 In Vitro Hemolysis Testing

The hemolysis test loop (Figure 3.1) consists of a basic recirculation loop similar to that described in Section 2.2.3 (page 28), depicted in Figure 2.4. Components relevant specifically to

gas exchange were removed, including the commercial oxygenator and the IPRAC gas pathway equipment. The large blood reservoir in the gas exchange circuit was replaced with a 1 L blood reservoir bag, which was submerged in a heated water bath to regulate the temperature of recirculating blood at 37 ± 1°C. Filtered and anticoagulated (20 U/mL) bovine blood was collected fresh from the slaughterhouse the morning of testing. Blood was conditioned with gentamicin (100 u/L) and hemoglobin corrected to 12 g/dL according to ASTM standards (F1841-97) [115]. Blood was recirculated at test conditions for 1 hour prior to sample collection to lyse older and fragile red cells that may spike early hemolysis measurements. Each test was run for 3 hours following initial recirculation, with samples drawn every 30 minutes. Impeller speed was maintained at 20,000 RPM in all tests and blood flow rate was set to 3.0 L/min with a blood pump (BPX-80; Medtronic, Minneapolis, MI, USA). Fluid pressure was monitored in the test section using a differential liquid pressure transducer (PX771-025DI; Omega Engineering, Inc., Stamford, CT, USA) and adjusted to venous pressures (10-15 mmHg) using a Hoffman clamp. 0.9% saline was continuously infused along the shaft (15 mL/hr) to lubricate and protect the seal and bearing from blood backflow up the driveshaft.

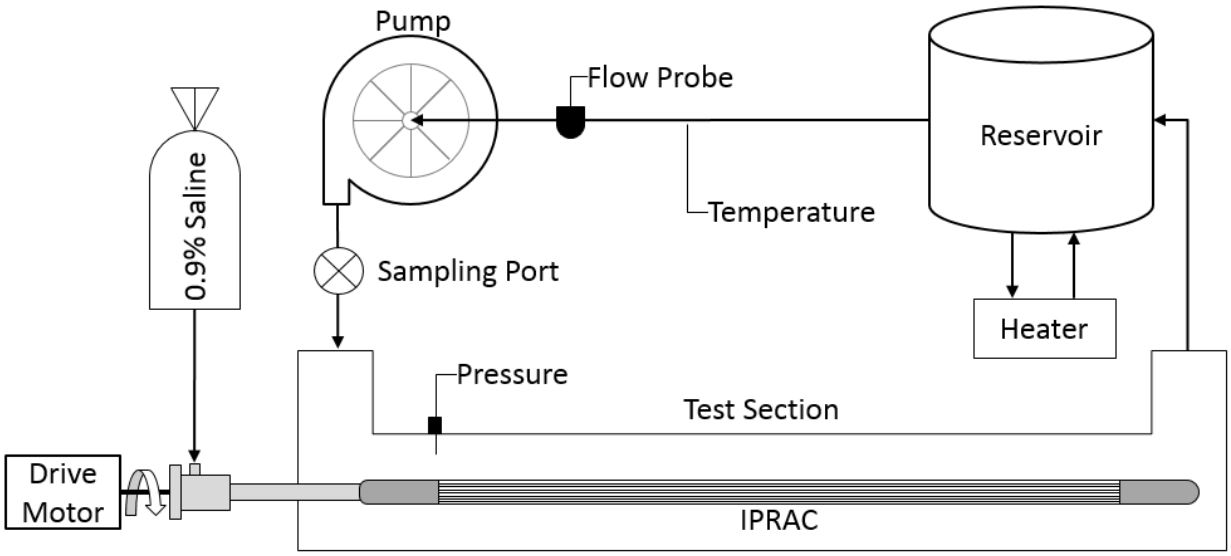

Figure 3.1. Recirculation loop for in vitro hemolysis testing with the IPRAC.

Plasma free hemoglobin (pfHb) was measured by centrifuging whole blood in two steps (15 minutes at 800 g, 10 minutes at 7,200 g) and analyzing supernatant plasma spectrophotometrically (Genesys 10S UV-Vis; Thermo Scientific, Waltham, MA, USA) at 540 nm. PfHb concentration was calculated from absorbance using a standard curve developed from a linear-fit of serially diluted whole blood with 100% hemolysis versus absorbance [116]. A Normalized Index of Hemolysis (NIH) that reports the rate of increasing pfHb in grams per 100 liters of blood flow through the device was calculated according to Equation 3.1.

$$NIH = \Delta pfHb \times V \times \frac{100 - HCT}{100} \times \frac{100}{\Delta t \times Q} \qquad 3.1$$

where NIH = normalized index of hemolysis (g/100L), $\Delta pfHb$ = increase in pfHb over the sampling time interval (g/L), V = total circuit blood volume (L), HCT = hematocrit (%), Δt = sampling time interval (min), and Q = average blood flow rate (L/min).

3.2.2 Test Devices

3.2.2.1 Full IPRAC

A baseline measurement for IPRAC generated hemolysis was determined with a full prototype previously used in gas exchange studies ("IPRAC" in results). The IPRAC prototype (23 Crescent impellers, 3 blades, 2 mm spacing – see Section 2.2.1) was inserted to the loop and suspended in the center of the test section with intersecting set screws, shown in Figure 3.2. A matching control loop with an empty test section was run in parallel to estimate the rate of cell damage due to circuit components independent of the IPRAC (e.g. blood pump, etc.). The control loop hemolysis measurement was subtracted from the IPRAC NIH value to determine the rate of cell damage for the test device. A summary of all tested devices is provided at the end of this section inTable 3.1, with specific comparisons summarized in Table 3.2.

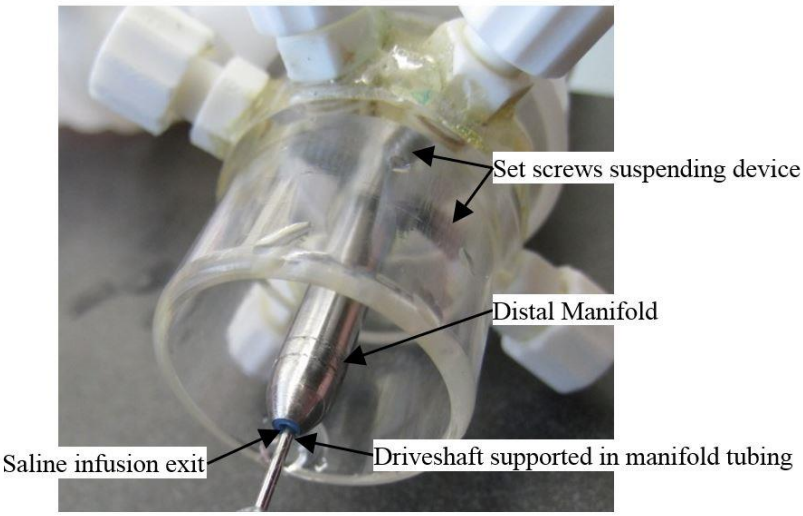

Figure 3.2. Distal manifold supporting rigid IPRAC shaft during hemolysis testing. Intersecting set screws suspend the IPRAC in the center of the test section. The rigid shaft terminates in the manifold tubing (PTFE), which is continuously flushed with saline.

3.2.2.2 Mag-Lev Device

Hemolysis due to impeller rotation was evaluated in a modified device with surrounding fiber bundle and safety coil removed ("Mag-Lev" device). Impellers were fit to a rigid stainless steel shaft (diameter matching flexible shaft diameter, 0.042") with intermittent annular magnets to maintain shaft stability in the absence of the surrounding safety coil. The arrangement of permanent magnets on the shaft is shown in Figure 3.3 (left). with the final arrangement of supportive magnets on the housing shown in Figure 3.3 (right). The final arrangement of magnets on the housing consisted of three fixtures holding 20-30 cylinder magnets on the housing (Figure 3.3, right) in addition to proximal and distal shaft support (Figure 3.2).

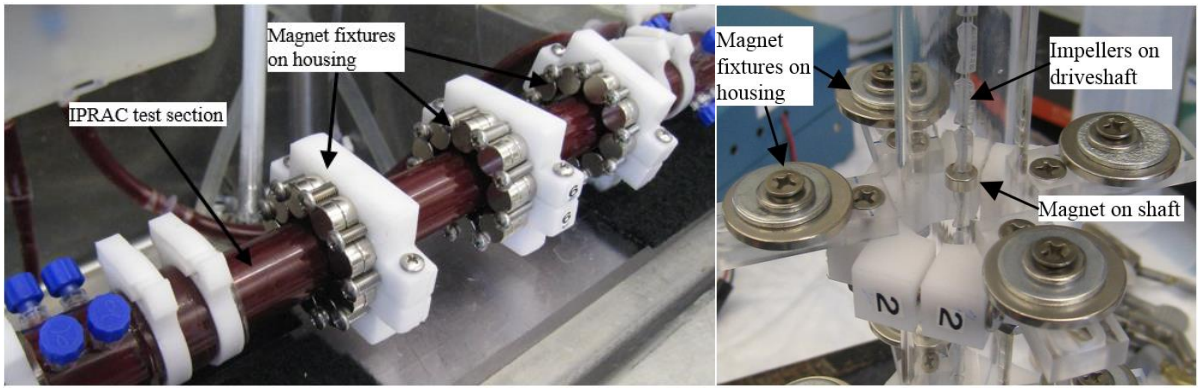

Figure 3.3. "Mag-Lev" IPRAC with magnetically levitated driveshaft for hemolysis testing. (left) Driveshaft shown with mounted magnets adjacent to impellers fixed on shaft. (right) Final arrangement of magnets on housing necessary for stable rotation at 20,000 RPM consisted of magnet arrays on three fixtures in addition to proximal and distal shaft support.

The specific contribution of impeller rotation to hemolysis was estimated by subtracting NIH of a control device with no impellers ("Blank Driveshaft" described below) from the Mag-Lev NIH value. A similar approach was taken to systematically estimate the NIH values associated with each design component of interest. The specific design aspects evaluated and the comparisons used for estimation are summarized in Table 3.2.

3.2.2.3 Blank Driveshaft Device

The third test device consisted of a rigid shaft with no impellers ("Blank Driveshaft" device). The shaft was supported by proximal and distal manifolds as shown in Figure 3.2. Measured NIH values were compared to the Mag-Lev device to estimate the contribution of impeller rotation to IPRAC hemolysis. This device was also used to evaluate if rotation of the driveshaft against static components caused cell damage by comparison it to the empty loop control circuit. A saline infusion (15 mL/hr) was connected to both proximal and distal manifolds to prevent blood backflow up shaft tubing. The full IPRAC prototype has only the proximal manifold to support the flexible driveshaft, which is accounted for when considering the contribution of these components by halving the calculated NIH value after subtracting the empty loop NIH.

3.2.2.4 Fiberless IPRAC – Stock Impellers

The fourth device tested was most similar in design to the full IPRAC prototypes, but had the fiber bundle removed ("Fiberless (stock impellers)" device). Impellers were fixed to a flexible driveshaft and rotated inside a safety coil as shown in Figure 3.4. This device allowed the contribution of the fiber bundle to be evaluated through comparison of hemolysis to the full IPRAC. The contribution of impeller/cage contact to hemolysis could also be investigated through comparison to the Mag-Lev device, allowing hemolysis associated with the impellers and manifolds to be controlled for.

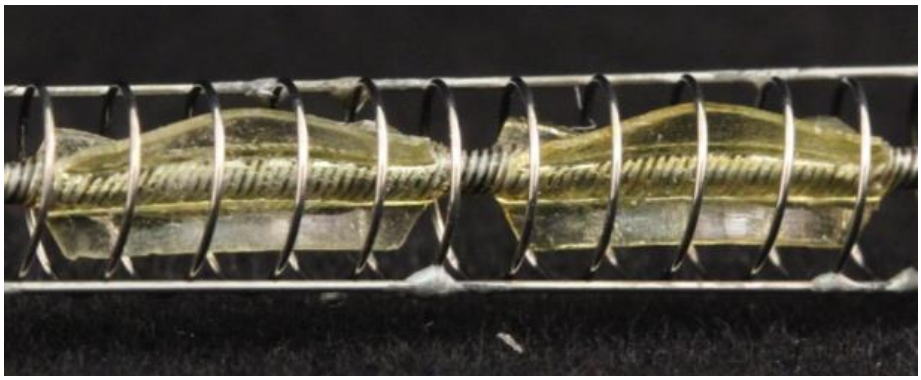

Figure 3.4. IPRAC impellers in safety coil used for hemolysis testing. “Fiberless (stock impellers)” device shown with crescent impellers (three blades, 2 mm shaft spacing).

3.2.2.5 Fiberless IPRAC – Polished Impellers

The final modified IPRAC device was built to investigate the effects of impeller surface roughness on hemolysis (“Fiberless (polished impellers)” device). Physical stress on red cells caught between impellers and the cage may be exacerbated with roughened surfaces. To investigate the effects of surface roughness during impeller/cage contact, stock impellers were re-coated with fresh resin (Watershed XC11122; DSM Somos, Sittard, Netherlands) hardened under UV. Impellers were incorporated into the Fiberless IPRAC prototype described above for direct comparison to that device. Surface roughness of impellers were qualitatively compared using scanning electron microscopy (SEM). Stock impellers, polished impellers, and stock impellers with wear (used in >5 experiments) were imaged. The Fiberless (polished impellers) device performance was compared to the Mag-Lev device to estimate hemolysis associated with polished impeller contact with the surrounding cage.

Table 3.1. Summary of modified IPRAC prototypes used for in vitro hemolysis testing.

Test Device	Device Description:
1) IPRAC	Full IPRAC prototype (Figure 2.1A). Stock impellers.
2) Fiberless (stock impellers)	IPRAC with fiber bundle removed (Figure 3.4). Stock impellers.
3) Fiberless (polished impellers)	IPRAC with fiber bundle removed (Figure 3.4). Polished impellers.
4) Magnetically Levitated Shaft	IPRAC with fiber bundle and safety coil removed. Impellers supported by magnet array on shaft and housing (Figure 3.3). Stock impellers.
5) Blank Driveshaft	IPRAC with fiber bundle, safety coil, and impellers removed.
6) Empty Loop (control)	Empty test section

3.3 RESULTS AND DISCUSSION

Plasma free hemoglobin (pfHb) concentrations measured during testing of the full IPRAC prototype over 3 hours are shown in Figure 3.5 alongside the control (empty) loop that was tested in parallel. PfHb concentrations rise linearly, which is representative of the consistency between measurements over the testing period for all datasets reported in this chapter (not all data shown).

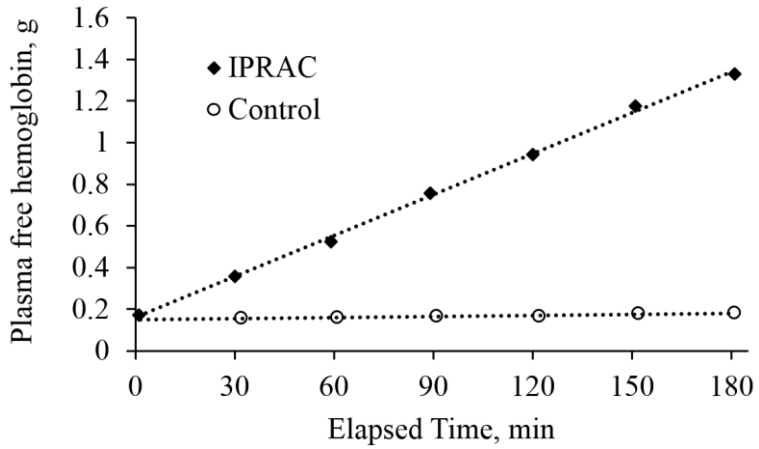

Figure 3.5. IPRAC in vitro hemolysis as total pfHb (g) versus Δt (min). Rate of accumulating pfHb in the recirculating loop was linear ($R^2 > 0.95$) over the testing period in all devices, including those not shown.

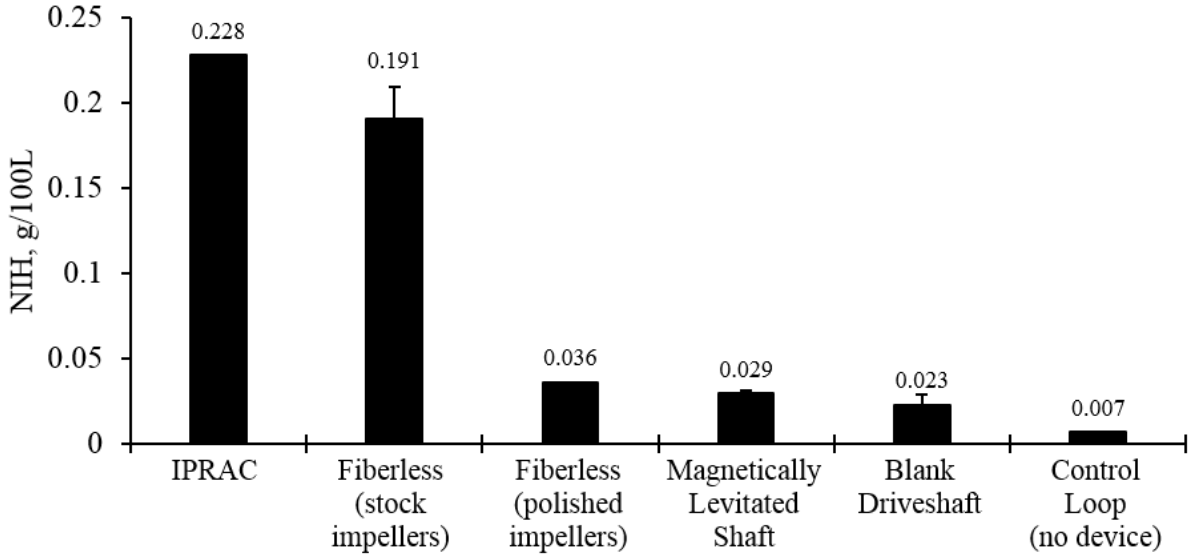

Figure 3.6. In Summary of in NIH values measured during IPRAC in vitro hemolysis studies. Device descriptions are summarized in Table 3.2.

The calculated NIH value for the full IPRAC prototype was 0.228 g/100L versus 0.007 g/100 L in the empty control loop. The estimated baseline NIH value for the IPRAC is therefore 0.221 g/100L after controlling for the empty loop performance. A NIH value ≤0.05 g/100L is generally considered an acceptable rate of cell damage in the blood pump literature [117]. This value is often reported for artificial lung devices as well, despite the absence of recent studies validating that exceeding this benchmark value translates to unacceptable in vivo performance. The estimated NIH for the IPRAC is significantly greater than the acceptable NIH value, indicating the existing design would likely cause unmanageable levels of cell damage in vivo. Following this result a series of hemolysis studies were conducted with the IPRAC. The objective of hemolysis studies were to identify design elements of the impeller system that contribute to cell damage so they can be addressed/eliminated from future IPRAC designs, or in other devices utilizing rotating impellers. The average NIH values of notable device configurations are summarized in Table 3.1 and discussed further below.

An IPRAC prototype was fabricated with a magnetically levitated driveshaft ("Mag-Lev") (Figure 3.3) to determine if impeller rotation at speeds necessary for effective active mixing is inherently hemolytic. The measured NIH of the Mag-Lev device over three experiments (n=3) was within the acceptable range at 0.029 ± 0.002 g/100L. Proximal and distal supports (Figure 3.2) were required in the Mag-Lev setup however, which may have contributed to some of the observed hemolysis in these studies. To control for hemolysis associated with the manifolds the Mag-Lev NIH was normalized by the Blank Driveshaft (i.e. no impellers) device with proximal and distal supports. The observed rate of hemolysis in the Blank Driveshaft experiments (n=4) was 0.023 ± 0.006 g/100L. Controlling the Mag-Lev hemolysis for the Blank Driveshaft device, the estimated NIH value associated with impeller rotation is 0.007 ± 0.002

g/100L. Similar normalizations were made between each of the modified IPRAC prototypes to isolate contributions associated with specific design components. Estimated hemolytic contribution of each IPRAC design component is summarized in Figure 3.7, with groups used for comparisons listed in Table 3.2. Not directly investigated here were non-contact shear effects associated with rough surfaces moving at high velocities that can contribute to hemolysis [114, 118, 119]. The Mag-Lev device performance suggests surface roughness plays an insignificant role in the current impeller system, however, based on the estimated NIH for that device using unpolished (stock) impellers. Testing indicates that impeller generated cell damage in the IPRAC is minimal in the absence of safety coil contact, and suggests that the impeller system may be adopted safely in new devices that could benefit from active mixing (e.g. extracorporeal CO_2 removal devices) or future IPRAC prototypes if other sources of hemolysis can be resolved.

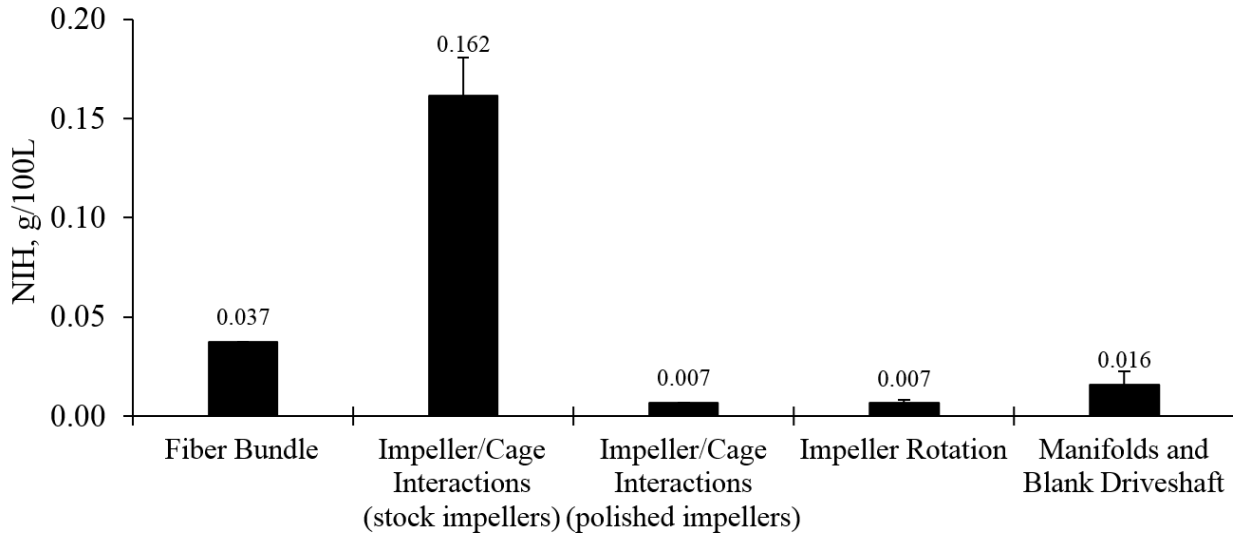

Figure 3.7. Estimated contribution to hemolysis of each IPRAC design component. Each dataset represents the estimated NIH value contributed by a single aspect of the IPRAC. Values were determined by normalizing test devices by data available for all other components. Test devices and controls for each design component listed are summarized in **Table 3.2**.

To identify other sources of hemolysis in the IPRAC, the fiber bundle and impeller/cage interactions were investigated. Material effects or high shear flow through the fiber bundle are possible mechanisms of hemolysis, and each can be evaluated for cell damage by comparison of the full IPRAC prototype to a comparable device with the fiber bundle removed (Figure 3.4). Contact between impellers and the surrounding safety coil may also contribute to significant levels of cell damage. Friction between rotating impellers and the static coil generates an unknown amount of heat, which at significant levels is known to cause hemolysis and clotting [110]. Blood cells caught between the impeller surface and the coil may also be physically

ruptured. Each of these mechanisms of hemolysis can also be evaluated with a fiber-less prototype (Fiberless (stock impellers) device) by comparison to the magnetically levitated device, which differs only in the presence of the safety coil. The device described above (Figure 3.4) was tested (n=7) and found to have a measured NIH = 0.191 ± 0.019 g/100L. Controlling for hemolysis contributed by impeller rotation and the proximal manifold, the normalized NIH associated with impeller/cage contact is ~0.162 ± 0.019 g/100L. This accounts for the vast majority of the blood damage observed in the full IPRAC prototype, and suggests impeller/cage interacts are the primary cause of hemolysis. Bundle effects account for the remaining hemolysis in the system, ~0.037 g/100L (full IPRAC prototype NIH, normalizing for impeller/cage contact, impeller effects, and manifolds).

Table 3.2. Summary of IPRAC design components investigated for in vitro hemolysis. Test Devices and Control devices differ only by the Design Component being investigated. E.g. Fiber Bundle effects were quantified by removing the fiber bundle from the full IPRAC device.

Design Component Evaluated	Test Device:	Controlled for:
1) Fiber Bundle	Full IPRAC	Fiberless (stock impellers)
2) Impeller/Cage Interactions (stock impellers)	Fiberless (stock impellers)	Mag-Lev Shaft
3) Impeller/Cage Interactions (polished impellers)	Fiberless (polished impellers)	Mag-Lev Shaft
4) Impeller Rotation	Mag-Lev Shaft	Blank Driveshaft
5) Manifolds/Rotating Shaft	Blank Driveshaft	Control Loop

Cell damage related to impeller/cage interactions could manifest in various ways. Heat generated from friction or physical trauma from cells being trapped between impellers and the coil at the time of contact could each cause hemolysis. Surface finish of impellers may play an important role in the severity of cell damage through impeller/cage interactions, and was investigated further by incorporating polished impellers into a fiber-less IPRAC device with a surrounding coil (Figure 3.4). Hemolysis generated by the test device had a NIH = 0.036 g/100L, which when normalized for cell damage associated with impeller rotation and manifold (magnetically levitated result) is ~0.007 g/100L. Surface finishes of impellers were qualitatively compared with SEM (Figure 3.8) imaging, revealing improvements in surface finish after

polishing impellers. The improvement in hemolysis testing with polished impellers suggests that the primary contributor to hemolysis in the IPRAC is impeller/cage interactions, but this may be alleviated with modifications to the impeller.

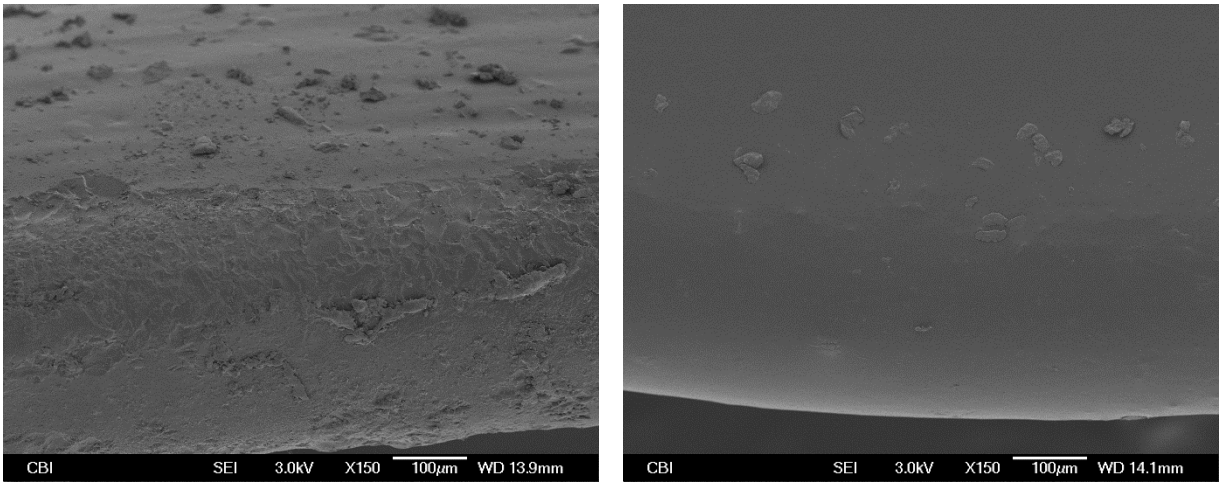

Figure 3.8. SEM images of IPRAC impeller blades detailing surface finish. (left) Blade of stock impeller at 150X detailing roughness on surface. (right) Smooth blade of polished impeller at 150X.

Hemolysis studies in modified IPRAC devices were conducted to determine if cell damage was a concern in the existing prototype. The contribution to hemolysis associated with the impellers, manifolds, impeller/cage interactions, surface effects (roughness), and the fiber bundle were each estimated through systematic comparisons in modified IPRAC prototypes. Impeller rotation was found to be minimally traumatic to blood cells, indicating they can be

safely used in future IPRAC devices or new extracorporeal CO_2 removal devices. Other components of the IPRAC design such as the manifolds where the shaft enters the blood compartment and the fiber bundle were also found to contribute to low levels of hemolysis. Impeller/cage interactions were identified to cause the greatest damage to blood cells, however this may be alleviated by improving surface finish on rotating impellers. This modification can be easily incorporated into future IPRAC prototypes and is not anticipated to affect overall gas exchange performance. Total gas exchange achieved with the IPRAC was ~40% below our target CO_2 removal rate however, and any modifications that improve gas exchange in future prototypes will require additional hemolysis studies.

Hemocompatibility testing here was limited to red blood cell hemolysis rates. Platelet activation or aggregation in response to non-biological surface contact, shear, or stagnation is a common pathway of thrombosis and device failure [120]. Housing and fiber materials were consistent with those commonly used in oxygenator devices to minimize material effects [97]. Surface effects cannot be fully eliminated with exposure to synthetic materials however, and may still trigger a biologic response. Impeller washing can help prevent stagnant clot formation, but platelet lysis in response to impeller shear can activate coagulation without sufficient anticoagulation [121]. Surface bound platelet levels in future impeller systems may be quantified as previously described using a lactate dehydrogenase (LDH) assay kit [8, 122]. Imaging of bundles under SEM may also reveal development of coagulation networks between fiber layers as well as identify platelet adhesion on fiber surfaces.

Impeller surface polishing was found to reduce impeller/cage associated hemolysis, however preventing impeller contact with the surrounding cage would more effectively minimize hemolysis. Implementing a system to prevent impeller/cage contact in the existing IPRAC device

would be very challenging. A concept for a magnetically levitated shaft was demonstrated here, however this approach is not feasible for an intravascular device. Significant magnetic forces were also required to stabilize the shaft (Figure 3.3). Elimination of impeller/cage contact could be accomplished in an extracorporeal device though replacement of the flexible cage with a larger, rigid driveshaft. The anticipated increase in overall device diameter to achieve this would be substantial and device flexibility would be compromised, limiting this approach to devices not intended for intravascular use.

4.0 FEASIBILITY TESTING FOR CO_2 REMOVAL AT ULTRA-LOW BLOOD FLOWS

4.1 INTRODUCTION

Extracorporeal gas exchange circuits have recently become recognized as a last resort option for severe lung failure when mechanical ventilation is failing or is not an alternative. Extracorporeal devices respirate blood independently of the lungs, allowing injured tissue to rest and heal [123]. The primary complication risks of extracorporeal gas exchange are associated with cannulation, exposure of blood to foreign materials, the concomitant requirement for systemic anticoagulation, and the stresses induced by mechanical pumping [22]. The degree of risk associated with these factors correlates with the extracorporeal blood flow rate necessary for treatment [22, 36, 120]. To provide full extracorporeal oxygenation of venous blood requires circuit flows up to the full cardiac output (4-7 mL/min) [35, 36]. In contrast, full metabolic CO_2 removal can be achieved at much lower extracorporeal blood flows. CO_2 is predominantly carried in the form of highly soluble bicarbonate ion that rapidly restores depleting CO_2 as it is eliminated, and the CO_2 dissociation curve is essentially linear and does not saturate like the oxyhemoglobin dissociation curve [31, 33, 34]. These differences also provide the opportunity to augment CO_2 removal efficiency with gas exchanger design features aimed at reducing the

thickness of the diffusive boundary layer at the gas exchange surface, where gas transport through blood is limited to diffusion [25].

The degree of risk associated with extracorporeal lung support is reduced when lower blood flows are needed to provide clinically meaningful benefit [36]. The ability to efficiently remove CO_2 at lower blood flows has motivated use of extracorporeal CO_2 removal, or $ECCO_2R$, as an alternative or supplement to mechanical ventilation. The two primary clinical indications where this objective is feasible are acute exacerbations of chronic obstructive pulmonary disease (ae-COPD) and moderate to severe ARDS, where lung protective ventilation strategies are necessary but are unable to maintain safe levels of CO_2 removal [28, 124]. $ECCO_2R$ was shown to reduce intubation rates in ae-COPD patients failing less invasive ventilation and assisted in weaning from ventilation [3, 4, 66, 69, 70, 72]. Hypercapnia was also managed in moderate ARDS patients using $ECCO_2R$ to facilitate more protective ventilation strategies by enabling reduction of tidal volumes to $\leq$4 mL/kg without complications [75, 23]. Associated risk remains the primary obstacle of $ECCO_2R$ adoption in these indications however. Currently approved $ECCO_2R$ systems can operate at blood flows around 500 mL/min, but still require cannula with size greater than 15 Fr [22]. The ability to provide the same levels of CO_2 removal at even lower flows will enable the use of smaller catheters that are similar in size to commonly used dialysis catheters that are 9-14 Fr.

Work on the IPRAC focused primarily on the development of new approaches to maximize gas exchange in a HFM based artificial lung device. Active mixing facilitated by rotating impellers yielded the highest CO_2 removal efficiency in the IPRAC of any reported device. CO_2 removal increased by >15-fold in the IPRAC (versus 0 RPM). The only approved respiratory assist device with active mixing (Hemolung RAS) increases gas exchange by ≈60%,

suggesting impeller mixing may be lucrative for enhancing gas exchange in an extracorporeal device [68]. Recognizing the broader potential of this approach, we hypothesized that impeller generated active mixing could be utilized in an extracorporeal device.

The IPRAC impeller technology was adapted to an extracorporeal device to determine if clinically significant CO_2 removal can be achieved at hemodialysis blood flows. CO_2 removal of 70-160 mL/min has been shown to benefit patients with hypercapnia, which translates to a target CO_2 removal rate of ≥25-35% metabolic CO_2 production (~200-250 mL/min) at normocapnia (pCO_2 = 45 mmHg) [53, 54]. The device also should maintain an optimal degree of fluid washing around the hollow fiber membranes to eliminate regions of stagnation but without causing unacceptable levels of blood cell trauma. This chapter reports on the design and bench testing of an ultra-low flow $ECCO_2R$ device (ULFED) utilizing the rotating impeller concept. Feasibility in vitro gas exchange testing was evaluated.

4.2 MATERIALS AND METHODS

4.2.1 Device Description

The feasibility prototype of the Ultra-Low-Flow $ECCO_2R$ Device (ULFED) (Figure 4.1) has the same basic geometry as the IPRAC device described in Section 2.2. Impellers (Crescent design, 3 blades, 4 mm OD, 10 mm length, spaced 2 mm, 23 total impellers) were fixed to a flexible driveshaft (0.042” (1.07 mm) diameter) (SS304V; Heraeus Medical Components, St. Paul, MN). Impellers rotate inside a stainless steel safety coil (inner diameter 5 mm) that protects the

surrounding fiber bundle. 750 PP fibers (Membrana Celgard x30-240, Wuppertal, Germany) were wrapped over the coil for a total surface area of 0.21 m^2. The assembly was potted in cylindrical acrylic housing (inner diameter 7/8" (22.2 mm)) leaving a small gap between the fiber bundle and housing wall (~4 mm). The total fluid priming volume is ~105 mL. Blood enters the housing at the center of the fiber bundle through a 3/16" (4.76 mm) stainless steel tube used in the potting (see Figure 4.1). Blood exits through a 1/4" (6.35 mm) port on the housing opposite the inlet.

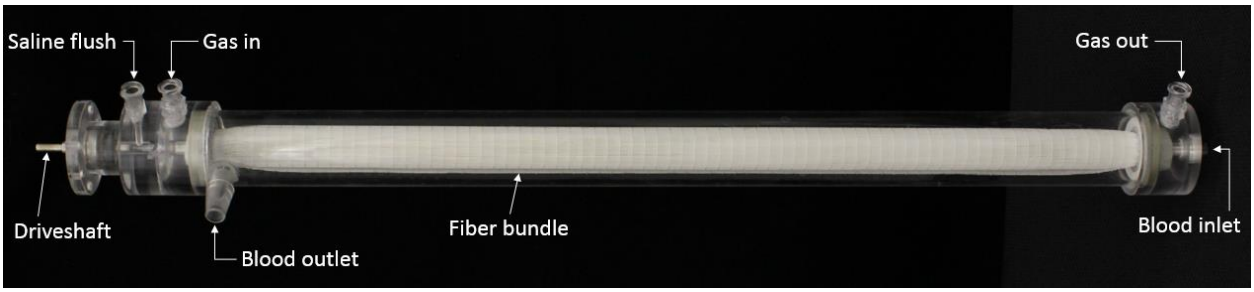

Figure 4.1. ULFED feasibility prototype with 750 PP fibers in 7/8" ID acrylic housing.

The impeller shaft exits the blood compartment at the center of the fiber bundle near the blood outlet port and connects to an external DC brushless servomotor (2057-048B; MicroMo Electronics Inc., Clearwater, FL). A stainless steel ball-bearing supports the shaft where it connects to the motor. The shaft is sealed with an oil seal (400054; SKF, Gothenburg, Sweden) next to the bearing. The driveshaft was continuously flushed with a saline infusion line (30

mL/hr) that protected seals and bearings from blood backflow up the driveshaft. The fibers terminate at each end of the housing in sealed compartments where they enter/exit the device through ports on the housing. Sweep gas flows counter-current to blood flow.

4.2.2 In Vitro Gas Exchange

CO_2 removal performance of the ULFED prototype was evaluated in a single-pass flow loop (Figure 4.2) at a hemodialysis blood flow rate of 250 mL/min. The evaluations followed ISO 7199:2009 standards for gas exchange testing in blood oxygenators [125]. Filtered and heparinized bovine blood (20 U/mL) was collected fresh from the slaughterhouse the day of testing. The fluid circuit consisted of a centrifugal blood pump (BPX-80; Medtronic, Minneapolis, MN), a commercial oxygenator (Affinity NT; Medtronic, Minneapolis, MN), two blood reservoirs connected in parallel, and the ULFED. Blood continuously recirculated at 4500-5500 mL/min while gas tensions were balanced by the commercial oxygenator to normocapnic venous conditions (pCO_2 = 45 ± 5 mmHg) using a $N2/CO_2/O_2$ gas mixture. Blood temperature was maintained at 37 ± 1°C with a heat exchanger integrated into the commercial oxygenator. Flow recirculated only to and from the primary reservoir during balancing, while secondary reservoir tubing remained clamped. Gas levels in the recirculating loop were monitored with a blood gas analyzer (RapidPoint 405; Siemens, Erlangen, Germany) until venous conditions were reached. The loop was then converted to single-pass mode for data collection by diverting flow to the secondary reservoir and clamping the bypass tubing in parallel to the ULFED. Measurements were collected at rotation speeds from 0-34,000 RPM once all measured parameters remained stable for ≥2 minutes. A minimum of two measurements were collected at

each rotation speed. Blood flow rate was continuously monitored with an ultrasonic flow probe (Transonic Systems, Ithaca, NY).

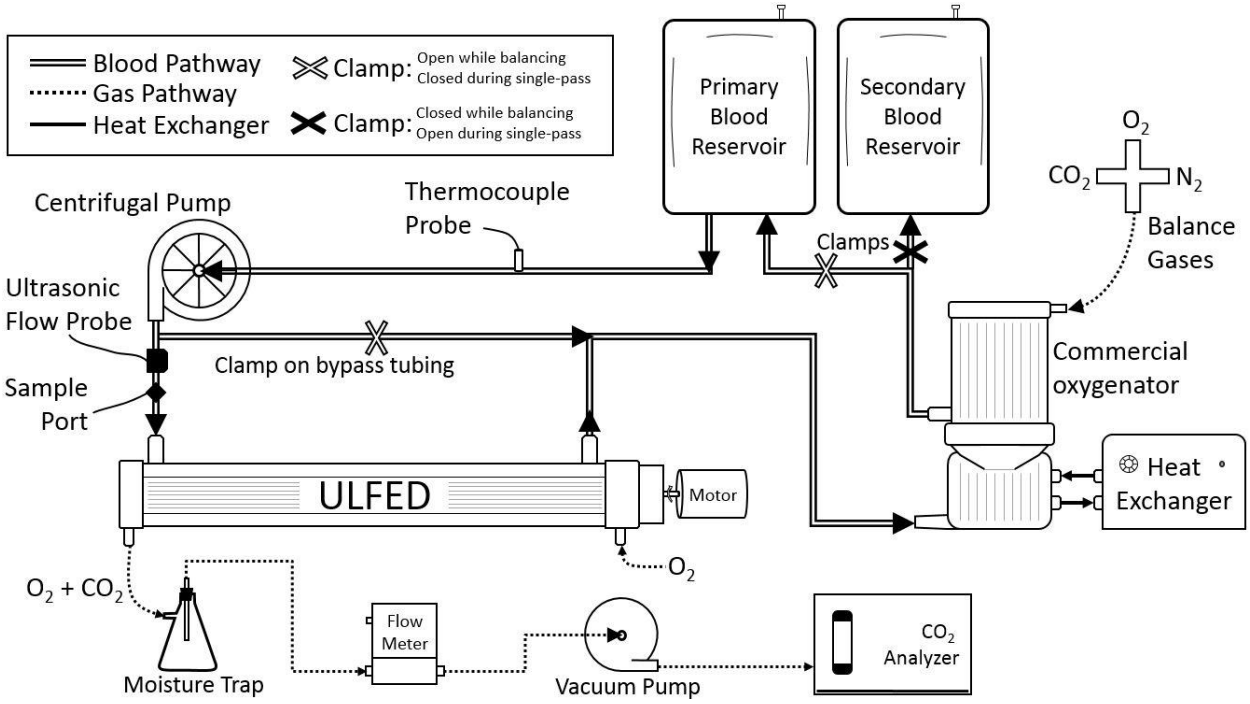

Figure 4.2. Test circuit used to evaluate in vitro gas exchange performance of the ULFED.

Details and equipment used in the sweep gas pathway match those described in Section 2.2.3. Pure O_2 sweep gas is pulled through fibers counter-current to blood flow at 5.7-6.2 L/min by a sealed vacuum pump (N811 KV.45P; KNF Neuberger, Inc., Trenton, NJ, USA). Gas flow rate was monitored with a mass flow controller (GR-116-1-A-PV-O_2; Fathom Technologies,

Georgetown, TX, USA). CO_2 in the sweep gas was measured directly with a gaseous CO_2 analyzer (WMA-4; PP Systems, Amesbury, MA, USA). CO_2 removal was calculated from the fraction of CO_2 in the outlet gas and the STP corrected gas flow rate according to Equation 2.1 (page 30) and normalized for inlet pCO_2 per Equation 2.2.

Performance is reported as the average and standard deviation at CO_2 removal at each rotation speed for one prototype. A minimum of two measurements were recorded at each rotation speed. A second prototype was fabricated and tested at select rotation speeds (10,000 – 30,000 RPM) at a later date to verify performance.

Blood samples were analyzed for hemolysis prior to and following gas exchange testing of the first prototype. An approximate normalized index of hemolysis (NIH) was calculated from measurements as described in Section 3.2.1 to estimate cell damage prior to conducting formal hemolysis testing. No formal hemolysis testing was conducted on the ULFED prototype.

4.3 RESULTS

Normalized CO_2 removal rates of each ULFED prototype tested are shown in Figure 4.3. Each device displayed a linear relationship between RPM and CO_2 removal at speeds ≥10,000 RPM. The first device achieved a maximum normalized CO_2 removal rate of 75.3 ± 0.3 mL/min at the highest rotation speed evaluated (34,000 RPM). Impeller generated active mixing overall contributed to ~225% enhanced CO_2 removal in the ULFED versus 0 RPM.

Measured NIH of the ULFED prototype over the ~6 hour gas exchange test was ~2.7 g/100L. Hemolysis in the ULFED is significantly greater than generally accepted values (≤0.05 g/100 L) for blood pumps and oxygenators. We suspect the highest RPM would contribute to the

greatest rate of cell damage, but these speeds were only maintained for short periods (~10 minutes) during data collection.

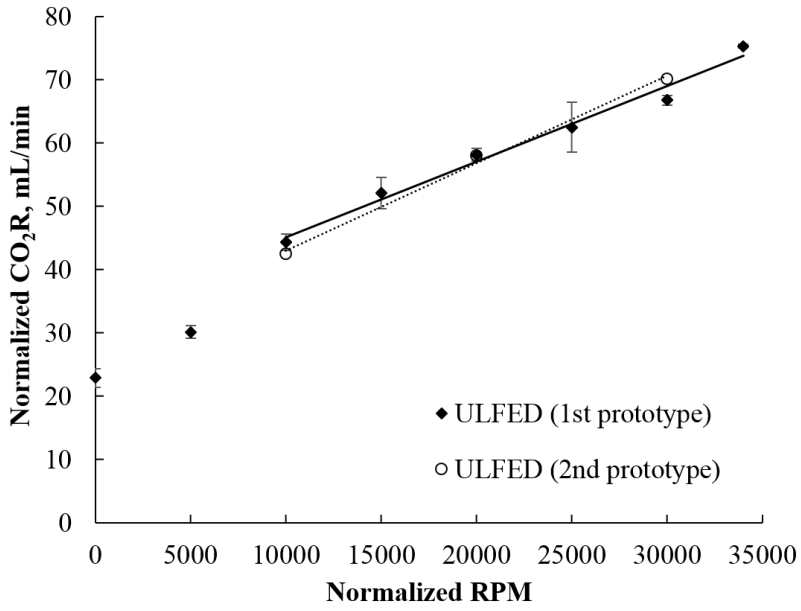

Figure 4.3. In vitro CO_2 removal of ULFED feasibility prototype versus RPM. CO_2 removal rates were normalized to an inlet pCO_2 = 45 mmHg.

4.4 DISCUSSION

Extracorporeal CO_2 removal ($ECCO_2R$) systems may be used in combination with non-invasive and protective ventilation to improve outcomes in hypercapnic respiratory failure. An $ECCO_2R$

device operating at conditions comparable to renal hemodialysis would allow adaptation of minimally invasive cannulation strategies used in dialysis. A minimally invasive $ECCO_2R$ system would also simplify circuit management, and has potential to be used with dialysis equipment or spliced into existing dialysis circuitry. Impeller technology from the IPRAC was adapted for a new $ECCO_2R$ device and demonstrated clinically significant CO_2 removal rates of 75 mL/min at 34,000 RPM could be achieved at hemodialysis blood flows (250 mL/min). Hemolysis measurements taken during gas exchange tests showed an NIH value of 2.7 g/100 L, a rate >10 times greater than acceptable values. Clinically significant gas exchange rates at dialysis flow rates were demonstrated but high hemolysis indicates a redesign focused on minimizing cell damage is necessary.

Invasive mechanical ventilation can exacerbate lung injuries using settings (tidal volumes ~12 mg/kg) that decarbonate the blood enough to prevent hypercapnia [15]. CO_2 removal at ≥65 mL/min (~25-35% metabolic CO_2 production) can correct pH and pCO_2 in hypercapnic patients to avoid transition to high tidal volume invasive ventilation [53, 54]. Intubation can be avoided with this level of support for ae-COPD and can aid in early extubation for patients already on ventilation [3, 66, 72, 77, 126, 127]. Early CO_2 removal therapy for these patients is emphasized given that mortality rates for patients transitioned to invasive ventilation after failing non-invasive ventilation are higher than if they had been intubated immediately [16]. CO_2 management also allows ventilator settings to be lowered to safer levels (tidal volumes ≤3-4 mL/kg) in ARDS that reduces risk of over-distending pulmonary tissue [23, 128, 129]. The CO_2 removal prototype here achieved CO_2 removal at ~30-37% metabolic CO_2 production, matching or exceeding levels with demonstrated clinical benefit.

An ultra-low-flow $ECCO_2R$ device (ULFED) operating at 250 mL/min makes CO_2 removal therapy comparable to dialysis and simplifies cannulation strategies. Efficient gas exchange allows fiber surface area to be minimized. Target CO_2 removal rates were achieved with 0.21 m^2, which is <40% of the surface area used in approved $ECCO_2R$ systems [54]. High washing due to impeller mixing also eliminates concerns of stagnation and associated clotting, potentially allowing anticoagulation requirements to be reduced. Existing $ECCO_2R$ systems use large fiber surface areas to achieve target CO_2 removal rates. Passive flow devices (i.e. having no active mixing mechanism) with CO_2 removal performance matching the ULFED have surface areas >1.3 m^2 (Novalung iLA Activve with iLA or XLung, Estor Prolung, Maquet PALP) [71, 78]. Low surface area devices (<0.5 m^2) that report lower CO_2 removal rates (<60 mL/min) and operate at low blood flows (<300 mL/min) are available or in development, including the Novalung iLA Activve with MiniLung or MiniLung Petite, and the Gambro-Baxter PrismaLung [80]. The Hemolung RAS has demonstrated clinical benefit to patients using a relatively low surface area design (0.59 m^2) and flows (350-550 mL/min) in part due to integrated active mixing components [22, 53].

Hemocompatibility testing was not formally conducted on the ULFED based on preliminary hemolysis data collected during gas exchange testing. Rotation speeds up to 34,000 RPM were tested in the ULFED that may have contributed to higher cell damage than seen in the IPRAC, which was tested only at 20,000 RPM. The ULFED was only tested at the maximum speed, where hemolysis is logically greatest, for short periods (~10 minutes). Hemolysis associated with the ULFED at maximum speed for an extended duration would likely be greater than the measured NIH of ~2.7 g/100L. In vitro hemolysis testing on the IPRAC revealed that contact between impellers and the surrounding cage was a significant source of cell damage.

When the cage and fibers were removed from a modified IPRAC as described in Chapter 3.0, hemolysis was within acceptable ranges (NIH < 0.05 g/100 L). Polishing impeller surfaces may eliminate cell damage associated with impeller/cage contact, but any feature contributing to measureable hemolysis are not ideal. Impeller/cage related cell damage in future ULFED prototypes can instead be eliminated entirely by preventing contact between impellers and the safety cage. This is accomplished in a redesign of the ULFED described in Chapter 5.0, where the flexible driveshaft is replaced with a larger diameter rigid shaft.

The ULFED was tested at rotation speeds greater than those evaluated in the IPRAC (34,000 versus 20,000 RPM). The IPRAC performance curves (RPM versus CO_2 removal) observed and reported by Mihelc et al. suggest it may also benefit from higher rotation speeds [5]. Gas exchange in the ULFED prototype at the maximum 34,000 RPM was 30% greater than at 20,000 RPM. We may therefore expect to see IPRAC CO_2 removal rates improve from 40 mL/min (see Chapter 2.3.4) to 50-55 mL/min if evaluated at this higher rotation speed.

5.0 ULFED DESIGN MODIFICATIONS AND IN VITRO PERFORMANCE CHARACTERIZATION

Sections from the following chapter are included in a manuscript currently under review for publication. The manuscript reports in vitro performance of only the top performing ULFED design discussed below, including gas exchange and hemolysis results. Topics omitted from the manuscript include the theoretical scaling analysis (Sections 5.2.1 and 5.3.1), comparison of bundle aspect ratio and impeller length on gas exchange performance (Sections 5.3.3 and 5.3.4), and the computational gas exchange model (Section 5.2.4).

5.1 INTRODUCTION

Clinically significant levels of CO_2 removal at hemodialysis flow rates was demonstrated with an ULFED prototype that closely resembled the IPRAC fitted to standalone housing. Hemocompatibility concerns associated with high rotation speeds required in the ULFED prototype and design features irrelevant to an extracorporeal device motivated additional work in this area and the design of a new impeller device optimized for the application. This chapter discusses design improvements to the ULFED that tailor its use for extracorporeal support.

Elimination of shaft flexibility removes a potential source of cell trauma by preventing contact between the impellers and the surrounding stainless steel coil, as well as heat generated

from friction where the shaft enters the blood compartment. Stabilizing the existing 0.042" diameter shaft at 34,000 RPM would be extremely challenging due to harmonic instabilities during rotation that occur with a small diameter shaft (discussed further in Section 5.3.1 below). The shaft diameter will therefore be increased to provide more stability according to a theoretical analysis of critical shaft rotation speed. The bundle and impeller diameters will also be scaled proportionally to maintain geometric similarity between the current and proposed design.

Gas exchange in the IPRAC was increased when spacing between impellers was reduced. A potential mechanism is that the number of recirculation regions in the bundle increased as a direct result of adding more impellers. Each impeller is associated with a distinct region of flow recirculation in and out of the fiber bundle, and increasing the density of recirculation regions may increase active mixing intensity and gas exchange. The effect of increasing the number of impellers (by reducing length) on gas exchange in the ULFED was investigated to evaluate this mechanism. The effects of fiber bundle geometry on gas exchange were also evaluated. The IPRAC bundle design was restricted by vascular dimensions that are irrelevant for an extracorporeal device. Changes to the bundle aspect ratio (length and diameter) affect fiber locations relative to the impellers and could be optimized to maximize efficiency. For example we hypothesize that lengthening the bundle will increase the surface area of fibers in the first layer of the bundle where we suspect active mixing intensity is greatest, but if this parameter has little impact a shorter bundle would simplify fabrication, require less impellers, and reduce priming volume.

This chapter reports on the redesign and testing of an ULFED for operation at hemodialysis blood flows (250 mL/min). A theoretical approach is described to estimate a range of appropriate design scaling factors to ensure shaft stability during rotation. The effects of

impeller length and bundle design were also investigated in the ULFED. We hypothesized that bundle geometry and impeller length are parameters that can be optimized to maximize performance. ULFED prototypes were tested in vitro for CO_2 removal performance. In vitro hemolysis testing was conducted using the top performing ULFED from gas exchange experiments against a clinically approved oxygenator control. In parallel we conducted a computational analysis using a previously verified mathematical model for CO_2 removal to estimate the performance enhancement gained by impeller generated active mixing.

5.2 METHODS

5.2.1 Determination of Theoretical Scaling Factor

The primary objective of the scaling analysis is to determine an appropriate shaft size for the ULFED so that rotational stability is maintained during operation. The shaft diameter, impellers, and bundle inner diameter will each be scaled by the same factor to maintain geometric similarity to the feasibility prototype.

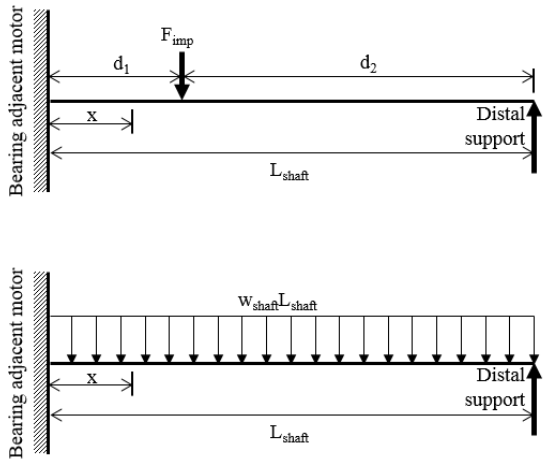

Shaft deflection due to impellers: $\delta_{imp}\left[x=\frac{L_{shaft}}{2}\right]=\sum^{\#imps}\delta_{imps,all}$

$for\ x=d_1 \rightarrow \delta_{imp}=\frac{F_{imp}{d_1}^2{d_2}^3}{12EIL_{shaft}^3}\left(3L_{shaft}+d_1\right)$

$for\ x<d_1 \rightarrow \delta_{imp}=\frac{F_{imp}d_2^2x}{12EIL_{shaft}^3}\left(3d_1L_{shaft}^2-2L_{shaft}x^2-d_1x^2\right)$

$for\ x>d_1 \rightarrow \delta_{imp}=\frac{F_{imp}d_1}{12EIL_{shaft}^3}\left(L_{shaft}-x\right)^2\left(3L_{shaft}^2x-d_1^2x-2d_1^2L_{shaft}\right)$

Moment of inertia: $I=\frac{\pi}{64}D_{shaft}^4$

Shaft deflection under own weight

$\delta_{shaft}\left[x=\frac{L_{shaft}}{2}\right]=\frac{w_{shaft}x}{48EI}\left(L_{shaft}^3-3L_{shaft}x^2+2x^2\right)$

$w_{shaft}=\rho_{shaft}g\frac{\pi}{4}D_{shaft}^2$

Figure 5.1. Theoretical shaft deflection equations for ULFED driveshaft. $\boldsymbol{\delta_{imp}}$ is the shaft deflection associated with each impeller, $\boldsymbol{L_{shaft}}$ is the shaft length between proximal bearings and distal supports, $\boldsymbol{x}$ is the distance to the deflection point (equal to ½ L_{shaft}), $\boldsymbol{F_{imp}}$ is the force associated with the mass of impellers along the shaft ($\boldsymbol{\rho_{imp}gV_{imp}}$), $\boldsymbol{\rho_{imp}}$ is the impeller material density (DSM Somos Watershed XC11122, 1.12 g/cm^3), $\boldsymbol{E}$ is the modulus of elasticity of the 316L stainless steel driveshaft (1.89e11 kg/m/s^2), $\boldsymbol{I}$ is the moment of inertia of the driveshaft, $\boldsymbol{\rho_{shaft}}$ is the 316L stainless steel driveshaft density (7.863 g/cm^3), $\boldsymbol{D_{shaft}}$ is the driveshaft diameter, and $\boldsymbol{w_{shaft}}$ is the weight of the driveshaft in N/m.

The minimum shaft diameter for future ULFED prototypes is based on the shaft's theoretical critical rotation speed, which is an approximation of the minimum rotation rate that excites the shaft's natural frequency. Operation at or above the critical speed (N_c) causes system vibration and instability, so common practice suggests operating speeds should be $\leq 0.75N_c$. We

are targeting operating speeds $\leq 0.5N_c$ for additional safety and to account for small errors due to estimations in the analysis. The critical rotation speed is calculated as

$$N_c = \frac{30}{\pi}\sqrt{\frac{g}{\delta_{st}}} \qquad 5.1$$

Where N_c is expressed in RPM, g is the gravitational constant (9.81 m/s^2), and δ_{st} is the maximum static shaft deflection due to gravitational forces at rest (meters). The shaft deflection is a function of the shaft diameter and is estimated from beam deflection equations that account for impeller and shaft weights as shown in Figure 5.1.

The beam was assumed to be fixed at one end (proximal end attached to motor) and supported distally. The number and mass of impellers was accounted for in deflection equations. Impeller length and diameter are scaled proportionally with the shaft to maintain geometric similarity so less impellers fit on the shaft as the scaling factor increases. The mass of individual impellers in the analysis was estimated based on anticipated volume in SolidWorks and raw material density. The total shaft deflection distance at rest is the sum of all deflections, $\delta_{st} = \delta_{shaft} + \sum^{\#\ imps} \delta_{imp,i}$, where the maximum deflection is assumed to be at the center of the shaft. Scaling factors of 1-5 were evaluated, where a scaling factor of 2 represents a shaft diameter of 2×0.046", i.e. double the IPRAC shaft diameter. The analysis was performed for exact impeller and bundle scaling factors but shaft diameters were limited to readily available sizes that could be stock ordered (e.g. 3/16", ¼", etc.). The closest available shaft size was used for all evaluated scaling factors.

Pumping ability of geometrically similar impellers will also increase as a function of diameter. Larger impellers will therefore require lower rotation speeds to achieve the same fluid velocities in the fiber bundle. We hypothesized that gas exchange will be comparable in the

scaled up ULFED if average fluid velocity in the fiber bundle is matched to the feasibility prototype [52, 130]. Fluid velocity leaving the blade tip was assumed to scale proportionally with impeller diameter. A decrease in fluid velocity was accounted for as fluid moves radially outward away from impellers (proportional decrease with radius). Bundle thickness was estimated using Archimedean spiral length equations to approximate the number of fiber wraps for any given scaling factor. Critical rotation speeds at each scaling factor were compared to the estimated rotation speed for scaled devices.

5.2.2 Device Description

The new ULFED prototype (Figure 5.2) shares the same basic design as the feasibility prototype discussed in section 4.2.1 and the IPRAC in section 2.2.1. A series of rotating impellers are fixed on a rigid stainless steel drive shaft and surrounded by an annular bundle of polypropylene (PP) hollow fiber membrane fibers (300 μm diameter, total gas exchange surface area 0.42 m^2) (Membrana Celgard x30-240, Celgard, Wuppertal, Germany) inside a cylindrical acrylic housing. Impellers (Figure 5.3) were designed in SolidWorks (Concord, MA, USA) and fabricated at the University of Pittsburgh Swanson Center for Product Innovation (Pittsburgh, PA, USA) from a hydrophobic epoxy resin (Watershed XC11122; DSM Somos, Sittard, Netherlands) using stereolithography (SLA). The Radial Tangent (3 blades) impeller design previously evaluated in the IPRAC (section 2.2.2) was chosen for future ULFED prototypes for its similarity to established centrifugal pump vane designs.

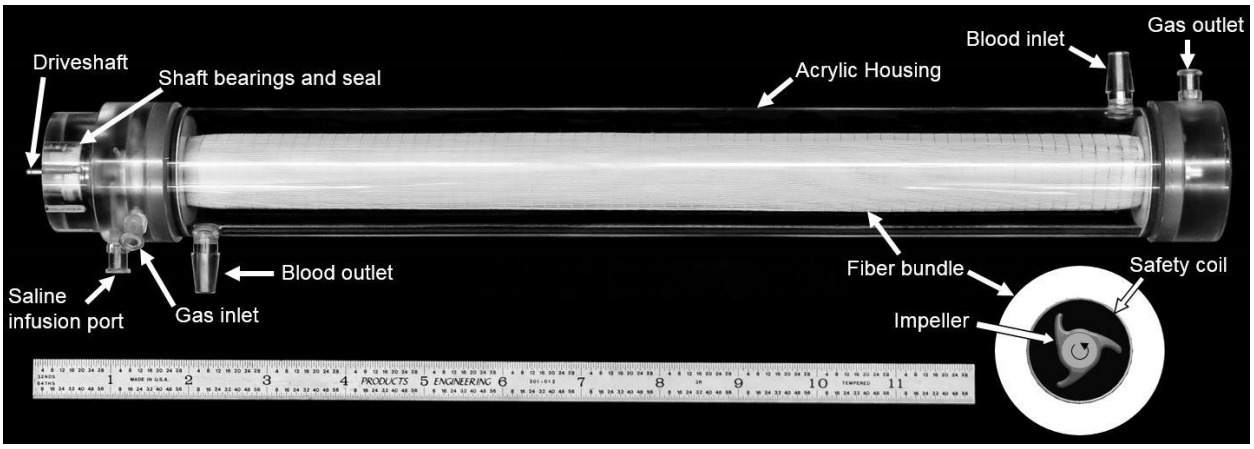

Figure 5.2. ULFED prototype and cross-sectional schematic. Schematic shows arrangement of impellers surrounded by safety coil and annular fiber bundle.

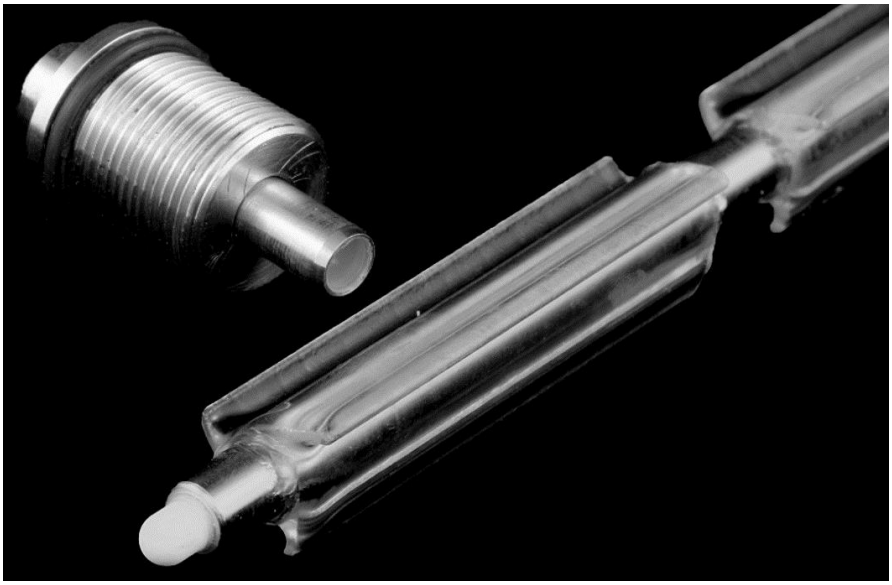

Figure 5.3. Distal end of ULFED driveshaft showing impellers and bearings. Impellers/bearings from Device 3 – (4 cm length, 11.7 mm diameter), ceramic pivot bearing, and UHMWPE bearing cup.

Three ULFED prototypes were fabricated to evaluate the impact of bundle aspect ratio on gas exchange. Impellers were fabricated with axial lengths according to the scaling analysis, and at 1/4 of the scaled length to evaluate the effects of impeller length (recirculation regions) in the bundle. Spacing between impellers was set to 1/5th impeller length to match the top performing arrangement from IPRAC testing (Section 2.3.1). Each shaft was fit with the maximum number of impeller that would fit in the available space. Specific device dimensions were determined through the scaling analysis and are presented in the Results section below in Table 5.2.

The impeller drive shaft extends out of the blood pathway and is sealed (400054; SKF, Gothenburg, Sweden) and supported by bearings (Ceramic R3; Ortech, Inc., Sacramento, CA). An external DC brushless servomotor (4490 H 048B; MicroMo Electronics, Inc., Clearwater, FL) drives shaft rotation. Heparinized saline (20 U/mL) is continuously infused along the shaft at 30 mL/hr to lubricate and protect the seal and bearing from blood backflow up the driveshaft. The shaft is supported distally using a custom pivot bearing (ceramic pin (MSC Industrial Supply, Melville, NY) nested in an ultra-high molecular weight polyethylene cup (UHMWPE; Orthoplastics, Lancashire, UK)) shown in Figure 5.3.

Blood ports on the proximal and distal ends of the house are 1/4" [6.35 mm]. Blood enters at the port distal to the motor, and exits at the opposite end. The location of the inlet port was relocated to the housing in the ULFED versus the previous prototype for ease of fabrication. Pure O_2 sweep gas is pulled through fibers under vacuum, counter-current to the direction of blood flow.

Three ULFED prototypes were fabricated with different bundle aspect ratios. Two additional prototypes were fabricated with the bundle aspect ratio that performed highest in gas exchange testing for repeatability and hemolysis testing.

5.2.3 In Vitro Gas Exchange

CO_2 removal performance of ULFED prototypes were evaluated according to methods detailed in Section 4.2.2 (page 67) following established ISO 7199:2009 standards [125]. Blood continuously recirculated until normocapnic venous conditions (pCO_2 = 45 ± 5 mmHg) were reached. ULFED gas exchange measurements were collected at dialysis blood flows (250 mL/min) at rotation speeds from 0-5,000 RPM once all measured parameters remained stable for ≥2 minutes. Pure O_2 sweep gas was pulled through fibers counter-current to blood flow at 8.0 L/min.

A minimum of two measurements were collected at each rotation speed. Each of the three ULFED prototypes were evaluated with both impeller configurations (full length and ¼ length impellers). Repeatability testing was conducted with two newly fabricated ULFED prototypes after identifying the highest performing bundle/impeller configuration. Failure in the gas pathway in one of the new prototypes limited repeatability testing to a single device. CO_2 removal of the two matching ULFED prototypes are reported as average and standard deviation of performance at each rotation speed.

5.2.4 Computational Gas Exchange Model

The ULFED fiber bundle design is not optimized for uniform flow in the fiber bundle in the absence of impeller mixing. To estimate the CO_2 removal enhancement associated with active mixing versus development of uniformly distributed flow in the fiber bundle we use a computational model developed and validated previously by our group to predict CO_2 removal in passive flow conditions. The mathematical model described by Svitek and Federspiel [101] uses

an empirical mass transfer correlation for a geometrically similar annular fiber bundle, incorporating a "facilitated diffusivity" to account for CO_2 transport in blood in the form of bicarbonate ion. The computational model was used exclusively for interpretation of gas exchange results and was not verified experimentally.

Derivation of mass transfer equations for O_2 and CO_2 in blood by membrane oxygenators have been reported by several investigators [51, 101–103, 131–134]. The overall mass balance is the same for each gas, the major differences being the definition of terms in the mass transfer correlation. The model assumes that gas side and membrane wall resistances are negligible because resistance to gaseous diffusion in blood is significantly greater [52]. Total CO_2 in the blood is either dissolved (7%), bound to hemoglobin (23%), or hydrated to bicarbonate ion (HCO_3) (70%) in a reversible reaction catalyzed by carbonic anhydrase enzyme within red blood cells [33]. Conversion between CO_2 and HCO_3 is many times greater than diffusion and convection in blood so the model assumes that dissolved CO_2 is always in equilibrium with hemoglobin bound and bicarbonate forms. The physical constants used for CO_2 in the model analysis are summarized in Table 5.1.

The overall mass balance of CO_2 in the blood is:

$$Q\frac{dC}{dr} = 2\pi rLka_v\Delta P \qquad 5.2$$

where Q is the blood flow rate perpendicular to the fiber bundle, C is dissolved and chemically bound gas concentration in blood, r is the radial coordinate, L is bundle thickness, k is the mass transfer coefficient, a_v is the membrane surface area per bundle volume, and ΔP is the gaseous pressure difference across the membrane wall, which is assumed to be constant from fiber inlet to outlet. Molecular diffusion of CO_2 is neglected from the mass balance since it is small relative

to convective transport. CO_2 concentration is estimated from an empirical fit of the CO_2 dissociation curve, relating partial pressure to total CO_2 (mL CO_2 /mL blood):

$$C_{CO_2} = qP_{CO_2}^t \quad 5.3$$

where q and t are constant regression parameters with values 0.128 and 0.369 [34].

The overall mass balance can be rearranged for CO_2 partial pressure as a function of radial displacement through the fiber bundle:

$$\frac{dP}{dr} = -\frac{2\pi rka_v L}{Q\lambda}\Delta P \quad 5.4$$

where λ is the effective solubility of both dissolved and bound CO_2:

$$\lambda = \frac{\partial C_{CO_2}}{\partial P_{CO_2}} = qtP_{CO_2}^{t-1} \quad 5.5$$

The mass transfer coefficient k is solved from an analogous mass transfer correlation for heat transfer perpendicular to a bundle of tubes [51, 102, 135]:

$$Sh = aRe^b Sc^{1/3} \quad 5.6$$

where Sh is the Sherwood number, Re is the Reynolds number, Sc is the Schmidt number, and the constants a and b are empirically derived values based on the fiber bundle geometry. The Reynolds number relates inertial to viscous forces, defined as $Re = \rho v d_h/\mu$, where ρ is the fluid density, d_h is the hydraulic diameter characteristic of the fiber packing (equal to hollow fiber diameter for packed beds with porosity >0.5), v is the superficial fluid velocity in the bundle ($Q/2\pi rL$), and μ is the dynamic fluid viscosity. The Schmidt number relates momentum to mass diffusivity, and is defined as $Sc = \nu/D$, where ν is kinematic viscosity, and D is diffusivity of the dissolved gas. The Sherwood number relates molecular to convective mass transfer resistance, defined as $Sh = kd_h/\alpha D$ where α is CO_2 solubility in fluid.

Table 5.1. Physical constants used in passive flow gas exchange model.

Parameter	Description	Value
Q	Blood flow rate	250 mL/min
ρ	Blood fluid density	1.06 g/mL
d_h	Hydraulic diameter	0.03 cm
μ	Dynamic viscosity of blood	3.4 cP
α	Solubility of CO_2 in blood	6.62e-4 mL_{CO_2}/mL_{blood} /mmHg
D_{CO_2}	Diffusivity of CO_2 in blood	7.39e-6 cm^2/s
D_{HCO_3}	Diffusivity of HCO_3 in blood	4.62e-6 cm^2/s
pCO_2^{in}	Inlet CO_2 partial pressure	45 mmHg
pCO_2^{fibers}	Average sweep gas CO_2 partial pressure	2 mmHg

A facilitated diffusivity (D_f) term must be used in the Sherwood number for blood, which accounts for diffusion of both bicarbonate ion and dissolved CO_2. An effective diffusivity (D_{eff}) term is then used in the Schmidt number that accounts for chemically bound forms of CO_2. Each is defined by Svitek and Federspiel [101] and simplify to:

$$D_f = D_{CO_2} + \frac{D_{HCO_3}}{\alpha}\lambda \tag{5.7}$$

$$D_{eff} = \frac{D_f}{1 + \frac{1}{\alpha}\lambda} \tag{5.8}$$

where D_{CO_2} and D_{HCO_3} are the diffusivities of CO_2 and bicarbonate ion in blood.

The above definitions and equations can be combined and rewritten to yield the mass transfer coefficient:

$$k = a\alpha d_h^{b-1}\left(\frac{Q}{2\pi r L}\right)^b \left(D_{CO_2} + \frac{D_{HCO_3}}{\alpha}\lambda\right)^{2/3} \left(1 + \frac{1}{\alpha}\lambda\right)^{1/3} \nu^{1/3-b} \tag{5.9}$$

Equation 5.9 can be inserted into Equation 5.4 and integrated to determine the partial pressure profile through the annular fiber bundle. The resulting profile can then be used together with Equation 5.3 to calculate the total CO_2 removed from the system:

$$V_{CO_2} = Q_{blood}\Delta C \qquad 5.10$$

where ΔC is the CO_2 concentration difference between the blood entering and exiting the bundle.

The constants a and b are unique to bundle design and are typically determined experimentally in gas exchange tests in water [51, 60, 101–103, 131–135]. Previous researchers have had success using the average of reported values for various devices however [130]. The ULFED bundle was designed with no expectation of achieving uniform flow through the fiber bundle under passive flow conditions (i.e. 0 RPM). Calculating mass transfer correlation constants from water experiments are therefore not feasible. The values measured by Svitek and Federspiel (a= 0.54, b= 0.42) were used to predict CO_2 removal to within 10% of experimental performance in two annular bundle designs. The ULFED design is comparable to the described device, having geometrically similar bundles, matching fiber surface area, and similar bundle porosity. Predicted flow in the ULFED also has estimated Reynolds (≈1–2) and Peclet (≈400–500) numbers within the range previously evaluated (Re ≈ 1–8, Pe ≈ 400–3500) in water. Other studies have reported these values in the range of a = 0.12–0.71 and b = 0.32–1 for blood oxygenators. Model calculations were conducted using a and b values from the geometrically similar bundle design. Calculations were also performed using conservative coefficient values that would yield the highest predictions among all oxygenators.

5.2.5 In Vitro Hemolysis Testing

Filtered and heparinized bovine blood (20 U/mL) was collected fresh from the slaughterhouse the day of testing per ASTM standards (F1841-97) [115]. The gas exchange loop was modified for hemolysis testing by removing the bypass tubing parallel to the ULFED, the commercial oxygenator, the secondary reservoir, and the ULFED gas pathway components. A reasonable cannula for the target 250 mL/min of blood flow (13 Fr Avalon Elite DLC 10013; Maquet, Rastatt, Germany) was included in the circuit so overall hemolysis reflected that of a clinical setup. Blood (1000 mL) was continuously recirculated with a pediatric centrifugal pump (PediMag; Thoratec, Pleasanton, CA) for 3 hours. The reservoir was submerged in a heated water bath to maintain a circuit temperature of 37°±1°C. ULFED rotation was set to the minimum speed necessary where CO_2 removal did not differ significantly from the maximum rate achieved. A second ULFED circuit configuration evaluated performance using a hemodialysis controller roller pump (Prisma; Baxter, Deerfield, IL) and cannula. A larger bore 14 Fr, 15 cm dialysis cannula (AK-22142-F; Teleflex, Morrisville, NC) was used in the second circuit due to availability of parts recommended for the target blood flows.

A control circuit was tested to evaluate ULFED hemolysis against an approved low-flow blood oxygenator (Minimax Plus; Medtronic, Minneapolis, MN). Blood flow in the control loop was maintained at the minimum rate necessary (1250 mL/min) to match ULFED CO_2 removal performance according to the manufacturer [136]. Pump (BP-50; Medtronic, Minneapolis, MN) rotation speed in the loop was maintained at 2100-2200 RPM against 180 mmHg to simulate inclusion of cannula recommended for use at the target blood flows (14 Fr Biomedicus 96820-014 venous, 12 Fr Biomedicus 96820-012 arterial) [137, 138]. Pressure against the pump was adjusted using a Hoffman clamp on ULFED outlet tubing and continuously monitored with a

differential fluid pressure transducer (PX771-025DI; Omega Engineering, Inc., Stamford, CT) across the pump. All other components and conditions were consistent between circuits. All three ULFED prototypes fabricated for gas exchange testing were evaluated for hemolysis in both circuit configurations, as the gas pathway failure observed in one prototype did not interfere with hemolysis testing.

Samples were drawn every 30 minutes to measure hematocrit (HCT) and plasma free hemoglobin (pfHb). Plasma was isolated from whole blood in two centrifuge spins (15 minutes at 0.8 g, 10 minutes at 7.2 g), and absorbance at 540 nm was measured spectrophotometrically (Genesys 10S UV-Vis; Thermo Scientific, Waltham, MA). PfHb concentration was calculated from absorbance using a standard curve developed from a linear-fit of serially diluted whole blood with 100% hemolysis versus absorbance [116].

The Normalized Index of Hemolysis (NIH) was calculated for circuit comparisons:

$$NIH\ (g/100L) = \Delta pfHb \times V \times \frac{100 - HCT}{100} \times \frac{100}{\Delta t \times Q} \qquad (11)$$

Where NIH = normalized index of hemolysis in grams of hemoglobin released into the blood per 100 L of flow through the circuit (g/100 L); $\Delta pfHb$ = increase in pfHb over the sampling time interval (g/L); V = circuit volume (L); HCT = hematocrit (%); Δt = sampling time interval (min); Q = average blood flow rate (L/min). A time-of-therapy normalized index was also calculated, since the NIH equation does not reflect total hemolysis returned to a patient in the context of treatment duration. Flow rate normalization in the NIH equation is eliminated in the new Therapeutic Index of Hemolysis (TIH) calculation to indicate the total grams of hemoglobin released to the blood per 100 minutes of therapy (g/100min):

$$TIH\ (g/100min) = \Delta pfHb \times V \times \frac{100 - HCT}{100} \times \frac{100}{\Delta t} \quad (12)$$

5.2.6 Statistics

All statistical comparisons were conducted in SPSS (IBM, Armonk, NY). Mean maximum gas exchange rates and performance curves were analyzed with a two-way ANOVA to identify specific design parameters or interactions that significantly affected performance (bundle length, bundle diameter, impeller length). A one-way ANOVA with Tukey HSD post hoc testing was used to compare removal rates at each RPM of the top performing device after data satisfied assumptions of homogeneity of variance, normality, and independence. RPM comparisons were used to identify the minimum speed necessary to achieve statistically equivalent performance to the maximum CO_2 removal rate. The determined rotation speed for that device was used for subsequent hemolysis testing. Mean NIH values were compared using a one-way ANOVA with Tukey HSD post hoc test after satisfying relevant assumptions. TIH data violated the assumption of homogeneity of variance via Levene's Test, and means were compared with Welch's F test. Subsequent Games-Howell post-hoc tests were used for between group comparisons of means. All comparisons of means were considered significant at the level $p<0.05$.

5.3 RESULTS

5.3.1 Scaling Factor Analysis and Device Dimensions

Figure 5.4 shows the estimated critical rotation speed ($0.5N_c$) of the driveshaft and estimated rotation speed necessary for prototypes versus scaling factors. The critical speed increases with scaling factor due to the increasing diameter of the driveshaft. The curve "steps" upward with scaling factor since the driveshaft diameter in our analysis was restricted to the closest available parts (e.g. drive shafts with diameters 5/32", 4 mm, 3/16", etc.). Small fluctuations in critical rotation speed between "steps" are associated with the increasing weight of impellers as each increases in size (slightly decreasing N_c) and decreasing number of impellers as less can fit on the shaft (from 23 impellers at scaling factor = 1 to 4 impellers at scaling factor = 5).

The curve showing required rotation speed to match average fluid velocity in the bundle of the feasibility prototype decays with scaling factor. The generated fluid velocity increases with impeller diameter, so lower speeds are necessary to achieve the same fluid velocity through the bundle. The relative distance between impellers and the bundle midpoint also decreases with increasing scaling factor since less fiber wraps are necessary in a larger diameter bundle. These factors contribute to the nonlinear decay of the required speed curve. The intersection of the two curves is the minimum estimated scaling factor where critical speed matches or exceeds necessary rotation speed. The region spanning these curves shaded in red in Figure 5.4 represent the range of acceptable scaling factors estimated for the redesigned ULFED. A scaling factor of 3.95 was chosen for the new ULFED dimensions based on availability of parts and one ULFED prototype was built to these dimensions. Two other prototypes were fabricated having reduced fiber length (Device 2) or reduced bundle diameter (Device 3) to evaluate bundle geometry

effects on gas exchange. Design dimensions of each ULFED prototype are summarized in Table 5.2.

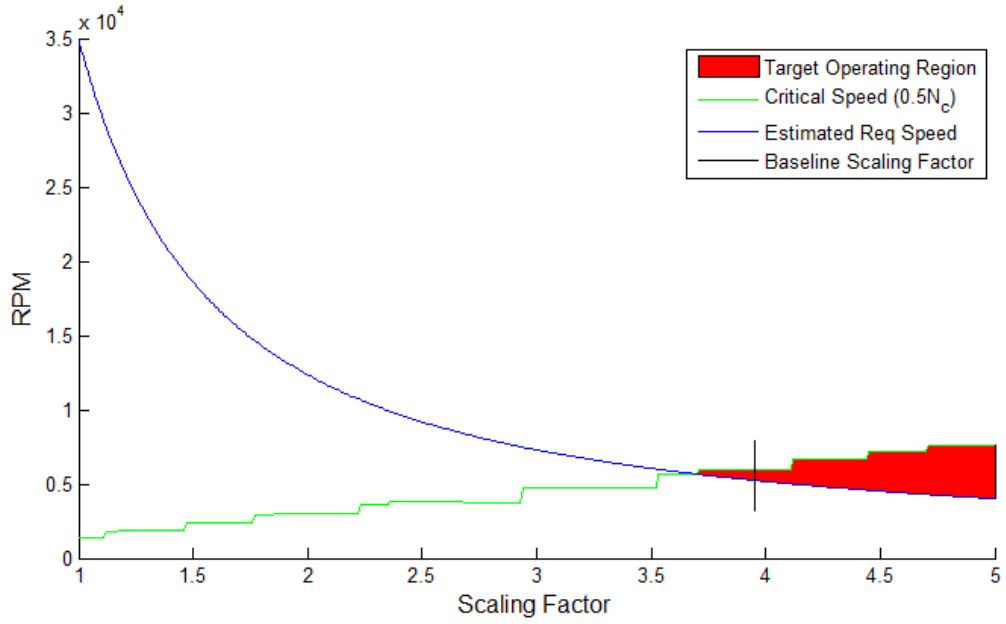

Figure 5.4. Results of ULFED scaling factor analysis. Plot shows estimates of theoretical critical speed ($0.5N_c$) at various impeller scaling factors (green) and estimated rotation speed at each scaling factor required to match the average superficial fluid velocity in the fiber bundle based on impeller blade tip velocity (blue). The target range of scaling factors are shaded in red. The chosen baseline scaling factor for the ULFED prototype (3.95) is marked in black.

Table 5.2. Dimensions of ULFED Test Devices.

	Device 1	Device 2	Device 3
Fiber Bundle Length	30 cm	16.9 cm	30 cm
Bundle/Impeller/Shaft Scaling Factor	3.95	3.95	2.7
Drive Shaft Diameter	3/16” [4.76 mm]	3/16” [4.76 mm]	3/16” [4.76 mm]
Annular Bundle Inner Diameter	21.3 mm	21.3 mm	14.4 mm
Annular Bundle Outer Diameter	28.5 mm	31.3 mm	22.8 mm
Bundle Thickness	3.6 mm	5.0 mm	4.2 mm
Impeller Diameter	15.8 mm	15.8 mm	11.7 mm
Estimated Priming Volume	240 mL	135 mL	240 mL
Impeller Configuration 1 *(4 cm impeller length, 0.8 cm shaft gap)*			
Number of Impellers	6	3	6
Impeller Configuration 2 *(1 cm impeller length, 0.2 cm shaft gap)*			
Number of Impellers	23	12	23

5.3.2 In Vitro Gas Exchange

Figure 5.5 shows the CO_2 removal rate of Device 3 as a function of rotational speed for both impeller configurations. Performance curves shown in Figure 5.5 are representative of trends in all devices, as well as the relationships between each impeller arrangement. Maximum CO_2 removal rates for each device are summarized in Figure 5.6. A sharp increase in CO_2 removal occurred between 0-2,000 RPM in all devices before subsequently leveling off at higher speeds. The maximum normalized CO_2 removal rates ranged from 57-75 mL/min, where Device 3 with 4 cm impellers achieved the highest rate of 75.1 ± 1.1 mL/min at 5,000 RPM. Performance at 4,000 RPM in the same device did not differ significantly from the maximum rate however (74.1 ± 3.3 mL/min, p=0.99).

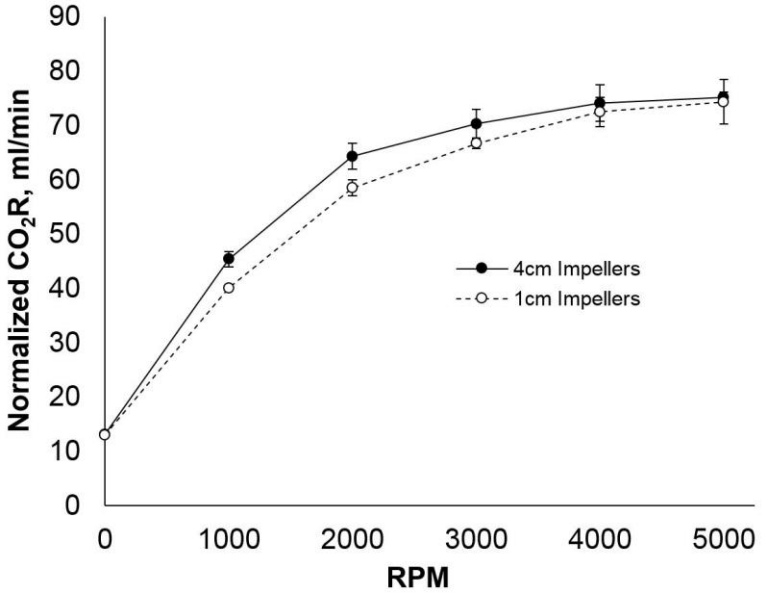

Figure 5.5. Example of ULFED gas exchange performance curves versus RPM (Device 3 with each impeller configuration shown). Error bars represent one standard deviation of measured $\boldsymbol{V^*_{CO_2}}$ at each rotation speed.

5.3.3 Bundle Aspect Ratio Effects

Maximum performance with both impeller configurations was 26–31% greater with the reduced bundle diameter in Device 3 (maximum $V^*_{CO_2}$ = 75.1 ± 1.1 mL/min, n=2 prototypes) than Device 1 (maximum $V^*_{CO_2}$ = 60.1 ± 3.9 mL/min) (all $p<0.05$). Gas exchange performance curves for Device 3 were significantly greater ($p<0.05$) than the larger bundle diameter Device 1 when tested with both 1 cm and 4 cm long impellers in 3 of 4 comparisons. The exception being Device 3, impeller configuration 2 versus Device 1, impeller configuration 2, where the two were not found to differ significantly.

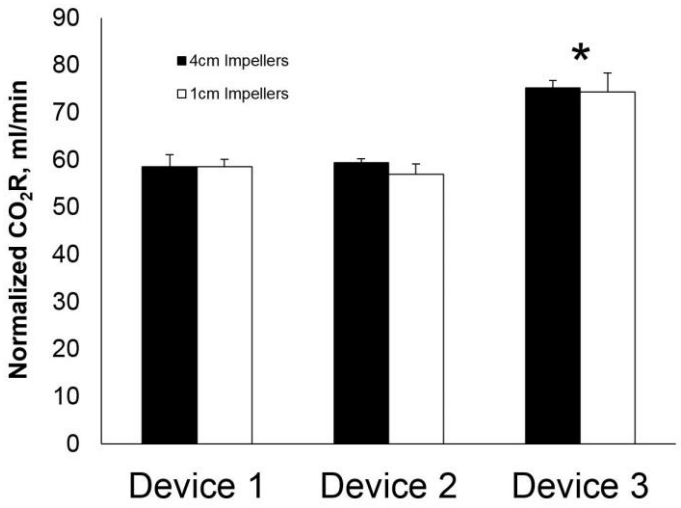

Figure 5.6. Maximum in vitro normalized CO_2 removal rate of ULFED prototypes in blood. Error bars represent one standard deviation. *$p<0.05$.

The impact of fiber bundle length was evaluated by comparison of Device 1 and 2. With impeller configuration 2, Device 1 was found to be significantly greater than Device 2 ($p<0.05$), but no difference was found when comparing each Device with impeller configuration 1. Total differences in gas exchange at each rotation speed for impeller configuration 2 were small however, with a maximum range of 6.6 mL/min (12%). Comparisons of only the maximum gas exchange rates (57-60 mL/min) of each device were insignificant ($p>0.05$), indicating that no practical performance advantage is gained by modification of the total bundle length.

5.3.4 Impeller Effects

Each device was evaluated with both impeller configurations (4 cm impeller length, 0.8 cm gap versus 1 cm impeller length, 0.2 cm gap). Impeller configurations were found to impact the performance curves in each device, where configuration 1 was superior in Devices 2 and 3, and configuration 2 achieved greater CO_2 removal in Device 1 (each $p<0.05$). No impeller configurations yielded significantly different maximum CO_2 removal rates however, so the overall impact of each difference was inconsequential.

5.3.5 In Vitro Hemolysis

Gas exchange performance was highest in Device 3 (30 cm length, 14.4 mm bundle diameter) and was selected for hemocompatibility testing. Maximum performance was comparable between impeller configurations, so each of the three prototypes were built with configuration 1 (4 cm length, 0.8 cm gap) for ease of fabrication. Measured rates of pfHb accumulation were highly linear over testing periods ($\Delta pfHb$ versus elapsed time $R^2 > 0.95$ in all tests, results not shown). Table 5.3 shows the calculated hemolysis indices for the ULFED (at 4,000 PRM) and the control device. NIH values for the standard-ULFED circuit (0.78 ± 0.19 g/100L), dialysis-ULFED circuit (1.55 ± 0.03 g/100L), and the control circuit (0.11 ± 0.01 g/100L) each differed significantly from one another (ANOVA $p<0.001$, all group-wise comparisons $p<0.001$). The TIH value of the standard-ULFED (0.190 ± 0.041 g/100min) did not differ significantly from the control circuit (0.123 ± 0.013 g/100min; Welch test $p<0.001$, group-wise $p=0.169$). The hemolysis using dialysis circuit components (0.386 ± 0.010 g/100min) was significantly greater than both other test groups (each $p<0.05$).

Table 5.3. Summary of ULFED in vitro hemolysis testing.

Test Device	Blood Flow (L/min)	TIH (g/100 min)	NIH (g/100 L)
ULFED (standard configuration)	0.25	0.190±0.041	0.775±0.186*
ULFED (dialysis configuration)	0.25	0.386±0.010*	1.551±0.025*
Minimax	1.25	0.123±0.013	0.105±0.012*

**Significant at $p<0.05$ versus all other devices*

5.4 DISCUSSION

Supplementing respiration by removing CO_2 independent of the lungs can improve outcomes for patients at risk of requiring or already receiving invasive mechanical ventilation. The ultra-low-flow $ECCO_2R$ device (ULFED) operates at blood flow rates consistent with renal hemodialysis to simplify circuit management and minimize invasiveness of CO_2 removal. In vitro CO_2 removal rates up to 74 mL/min at 4,000 RPM were achieved by the ULFED with minimal cell trauma (therapeutic index of hemolysis, TIH = 0.19 g/100min) at blood flows consistent with dialysis (250 mL/min).

CO_2 removal systems used in conjunction with non-invasive or protective ventilation strategies have been shown to correct pCO_2 and pH in hypercapnic patients with removal rates equivalent to ~25-35% of the metabolic CO_2 production (~200-250 mL/min) [53, 54]. CO_2 removal at these levels prevented intubation in patients with ae-COPD failing or unresponsive to non-invasive ventilation [3, 66, 72, 77]. Partial respiratory assistance has also aided weaning from ventilation [3, 126, 127] and allows reduction of ventilator tidal volumes to ultra-protective levels (3-4 mL/kg) [23, 128, 129]. The ULFED exceeded these CO_2 removal rates by eliminating

~30-37% of the metabolic CO_2 production at normocapnic test conditions (inlet pCO_2 = 45 mmHg). Gas exchange will also increase proportionally with pCO_2 in hypercapnic patients, where CO_2 removal up to 50% or more of metabolic production can be required.

Efficient gas exchange in the ULFED minimizes necessary fiber surface area and enables clinically significant CO_2 removal rates at hemodialysis blood flows. Pump-less arteriovenous CO_2 removal ($AVCO_2R$) requires dual cannulation (13-19 Fr) for circuit flows of 600-2,000 mL/min that is shunted between the femoral artery and vein through a 1.3 m^2 oxygenator [129, 139, 140]. A newer integrated pump-oxygenator system uses a rotating core to generate active mixing to improve gas exchange up to 60% with a 0.59 m^2 bundle [141]. Comparatively lower flows (350-500 mL/min) are possible in the simplified veno-venous circuit, but requires 15.5 Fr cannulation [22]. Developing systems combine existing oxygenators with dialysis controllers targeting even lower flows (200-300 mL/min) to minimize cannulation invasiveness (≤14 Fr). These systems utilize larger surface area gas exchangers (≥1 m^2) to improve performance [77, 78] or target lower CO_2 removal using smaller pediatric oxygenators (40-55 mL/min with 0.3 m^2 bundle in pigs with $PaCO_2$ > 80 mmHg) [80]. Approaches to enhance CO_2 removal such as bicarbonate dialysis [90], blood acidification [87], electrodialysis [88], plasma recirculation [73], and fiber enzyme coatings [84] are also being explored to reduce necessary blood flows for treatment.

The rotating impellers in the ULFED enhance gas transfer by generating an active mixing effect in the fiber bundle that improves convective mixing at gas exchange surfaces [5, 44, 91, 130]. Computational simulations have indicated development of continuously recirculating flow pathways in/out of the fiber bundle with impeller mixing [91]. Blood is pumped radially outward through the bundle by impellers, then pulled back into the bundle toward low-pressure regions in

the gaps between impellers before converging onto the impeller blade and cycling through the bundle again. Increasing flow velocity past gas exchange surfaces is a well-established mechanism for improving transfer efficiency by diminishing the thickness of the surface diffusive boundary layer [103]. This facilitates replenishment of gases to the membrane surface to maximize the concentration gradients spanning fiber walls. Recirculating flow also maintains a high level of washing in the bundle that eliminates regions of stagnation where thrombus formation may otherwise occur at low blood flows.

The linear region of gas exchange performance at higher RPM that is observed in nearly all devices suggests there may be a maximum CO_2 removal rate achievable by active mixing that is characteristic of the bundle geometry. This is supported by performance curves of each device being statistically distinguishable when comparing impeller lengths (each $p<0.05$), but ultimately achieving the same maximum CO_2 removal rates (each $p>0.05$). Impeller length may have a stronger impact on gas exchange than demonstrated here, but the ability to establish this was limited by bundle geometry.

We attribute the performance improvement between Device 1 and 3 here to the difference in bundle diameter, however the impeller geometry is different in these devices as well. The vane height of impellers in Device 3 are approximately 1/2 that of Device 1 impellers, which is necessary to accommodate the reduced inner diameter of the fiber bundle. It is unlikely the performance differences are associated with impeller vane height based on our previous findings using impellers for active mixing and mechanics of impeller mixing. Trimming vane height reduces overall impeller diameter, which reduces the blade tip velocity (and associated exiting fluid velocity) for any given rotation speed. We have also shown that increasing vane height (by

135%) of geometrically similar impeller designs by reducing drive shaft diameter improved gas exchange by <10% [5, 91].

Simulations were conducted for each of the three ULFED device geometries to predict CO_2 removal under passive flow conditions (i.e. 0 RPM). The computational analysis was conducted to support the hypothesis that impeller generated active mixing enhances CO_2 removal rather than solely attributing increased CO_2 removal to development of uniform flow in the fiber bundle. The results are presented as supportive evidence, but model predictions were not verified experimentally. Results of the analysis are shown in Table 5.4. Estimated V_{CO_2} for each Device are compared to the measured maximum CO_2 removal rate for each device listed as percent difference, i.e. Active Mixing % Enhancement = (measured $V^*_{CO_2,max\ speed}$ − predicted $V_{CO_2,0\ RPM}$)/(predicted $V_{CO_2,0\ RPM}$). Predictions were made using Reynolds coefficients that best represent the bundle geometry (a = 0.54, b = 0.42) as well as conservative values that maximized predicted performance (a = 0.71, b = 0.32). CO_2 removal estimates differed by <5% between devices for each set of Reynolds coefficients. The representative and maximum CO_2 removal rates predicted were 40.1 ± 1.0 mL/min and 53.6 ± 0.9, respectively. This suggests that improved flow uniformity in the bundle at low rotation speeds only partially accounts for the increasing performance with rotation speed. Comparing model to experimental performance, we predict that active mixing in the ULFED contributes to an estimated 10–50% enhancement in Devices 1 and 2, and 40–80% enhancement in Device 3.

The measured rate of hemolysis in the standard-ULFED circuit was comparable to a clinically approved oxygenator circuit. Two indexes of red cell trauma are reported here that indicate the rate of pfHb accumulation over time, the key difference being how time is reported. A major limitation of the NIH calculation is that hemolysis is normalized for blood flow rate, but

operating flow rate is ultimately irrelevant. Two systems intended for use at 5 L/min versus 0.25 L/min that cause equivalent rates of total cell damage would differ in NIH by a factor of 20, despite returning an equal number of pfHb species to a patient. As a result the NIH calculation is bias against low-flow devices. The TIH calculation removes the flow rate normalization and provides a clinically relevant time-of-therapy rate of hemolysis. The limitation of both indices however is that no reliable benchmark threshold values have been validated for low-flow devices against in vivo performance to our knowledge. More information or in vivo testing is therefore necessary to make conclusions regarding acceptability of the dialysis-ULFED performance. No difference in hemolysis was observed between the control and standard-ULFED circuits, so we expect in vivo hemolysis to be acceptable in this configuration.

Table 5.4. Predicted ULFED performance for each set of *Re* coefficients in Equation 5.6.

ULFED Design	$0.54Re^{0.42}$		$0.71Re^{0.32}$	
	Predicted V_{CO_2} (0 RPM)	Active Mixing % Enhancement	Predicted V_{CO_2} (0 RPM)	Active Mixing % Enhancement
Device 1	39 mL/min	48%	53 mL/min	10%
Device 2	40 mL/min	50%	53 mL/min	12%
Device 3	41 mL/min	82%	55 mL/min	37%

Additional shortcomings of the NIH calculation are highlighted by the Minimax circuit performance. The NIH value of 0.105 ± 0.012 g/100 L is twice the generally accepted threshold (0.05 g/100 L) for tolerable hemolysis, despite each of the circuit components being approved

clinically. NIH values of approved adult oxygenator circuits have been reported up to 0.047 g/100 L at a blood flow rate of 5 L/min [142]. This translates to an absolute rate of hemolysis almost twice that of the Minimax circuit reported here, further exemplifying the ambiguity of normalizing by blood flow rate.

The simplicity of using the TIH calculation is further emphasized when considering the physiological pathway of plasma free hemoglobin clearance from the body. Conjugation of pfHb to haptoglobin allows clearance primarily through the reticuloendothelial system at plasma concentrations up to 130-150 mg/dL [105, 106]. Above these levels hemoglobin deposits into body tissues, hemoglobinuria occurs, and can eventually lead to endothelial cytotoxicity and excessive nitric oxide scavenging [107–109]. Bernstein et al. demonstrated in dogs that the haptoglobin clearance pathway sufficiently managed continuous infusions of 0.1 mg Hb/kg/min for three weeks without complications or plasma concentrations exceeding 100 mg/dL [143]. This infusion rate is equivalent to 0.7 g/100min in a 70 kg human, far exceeding hemolysis measured in either ULFED circuit configuration.

Additional in vitro hemocompatibility testing could be conducted in future ULFED prototypes that focus on platelet adhesion and activation levels. Thrombus formation was qualitatively determined to be minimal after disassembly and inspection of ULFED prototypes following blood testing. Coagulation in the ULFED could form as a result of platelet activation in response to non-biologic surface contact or platelet cell lysis [120]. Fiber materials used in the ULFED were chosen partially to minimize biologic responses as demonstrated in previous oxygenator devices, but surface effects are still possible [97]. Verification that coagulation is minimal in the ULFED without excessive anticoagulation is valuable to support conclusions regarding safety. Platelet deposition rates on surfaces in future ULFED prototypes can be

quantified through plasma lactate dehydrogenase (LDH) levels and electron microscopy to identify thrombus networks on fiber surfaces or between fiber layers [8, 122].

Future work may also focus on in vivo validation of benchtop performance or improvements to the ULFED aimed at simplifying the design, such as sealing the blood compartment with a magnetically coupled driveshaft that would obviate the driveshaft seal and saline infusion. Improvements to the housing design that were not thoroughly investigated here may also be investigated. The gap distance between the housing wall and fiber bundle could be revisited, enabling priming volume to be reduced by up to 30%. Future ULFED bundles could be shortened to reduce priming volume and materials after bundle length was shown to have no impact on gas exchange. Incorporation of carbonic anhydrase (CA) immobilized fibers may enhance gas exchange and improve biocompatibility [6–8]. CA fibers in an active mixing device is explored further in Chapter 6.0.

6.0 CARBONIC ANHYDRASE WITH ACTIVE MIXING FOR LOW FLOW CO_2 REMOVAL ENHANCEMENT

6.1 INTRODUCTION

The use of bioactive carbonic anhydrase (CA) immobilized fibers has been demonstrated in miniaturized gas exchange modules to increase CO_2 removal performance by up to 37% in blood [84]. CO_2 removal enhancement with CA fibers diminished as the flow rate in the modules increased, suggesting that devices with longer transit times (i.e. low flow rate) would benefit the greatest from the technology [84]. Additional mechanisms that reduce the diffusional boundary layer resistance without affecting device transit time such as active mixing should also promote delivery of bicarbonate to the boundary layer. A low-flow active mixing CO_2 removal device such as the ULFED could therefore benefit significantly from the CA fiber technology.

To evaluate the feasibility of combining the CO_2 removal enhancements of active mixing and CA immobilized fibers in a meaningful way, Bioactive CA fibers were incorporated into a modified ULFED prototype to evaluate the feasibility of improving CO_2 removal versus either approach independently. In vitro gas exchange tests were conducted with a CA-ULFED prototype and control devices at low blood flow rates (250 mL/min).

6.2 METHODS

6.2.1 Device Fabrication

The device used for evaluating CA with active mixing (Figure 6.1) was designed with comparable geometry to the ULFED feasibility prototype described in Section 4.2.1. The design of the CA-ULFED devices differ only in the length of the fiber bundle and the type of fibers used. PP fibers were swapped for wetting-resistant polymethylpentene (PMP) (380 μm outer diameter, Membrana Oxyplus, Wuppertal, Germany) fibers to eliminate concerns associated with hydrophobicity losses through the immobilization process. The blood compartment length of the prototype was reduced to 9.3 cm due to the availability of shortened PMP fibers. Bundle permeance in the modified ULFED using larger diameter PMP fibers was matched to the PP bundle in other ULFED designs to replicate active mixing conditions. The final CA-ULFED was designed with bundle porosity = 0.56 and 523 fibers, for total surface area 0.058 m^2. Device assembly was otherwise consistent with the techniques described in Section 4.2.1 with the exception of the fiber potting adhesive. A waterproof epoxy (Anchor-Tite Superglue; Pacer Technology, Ranchero, CA, USA) was used for potting fibers to allow fibers to remain hydrated during potting. A flexible driveshaft was fitted with 7 impellers (Crescent geometry, 3 vanes, 2 mm shaft spacing). All other components and dimensions used in the modified ULFED matched those described in Section 4.2.1. Six prototypes were fabricated and tested for gas exchange (n=2 for three fiber test groups).

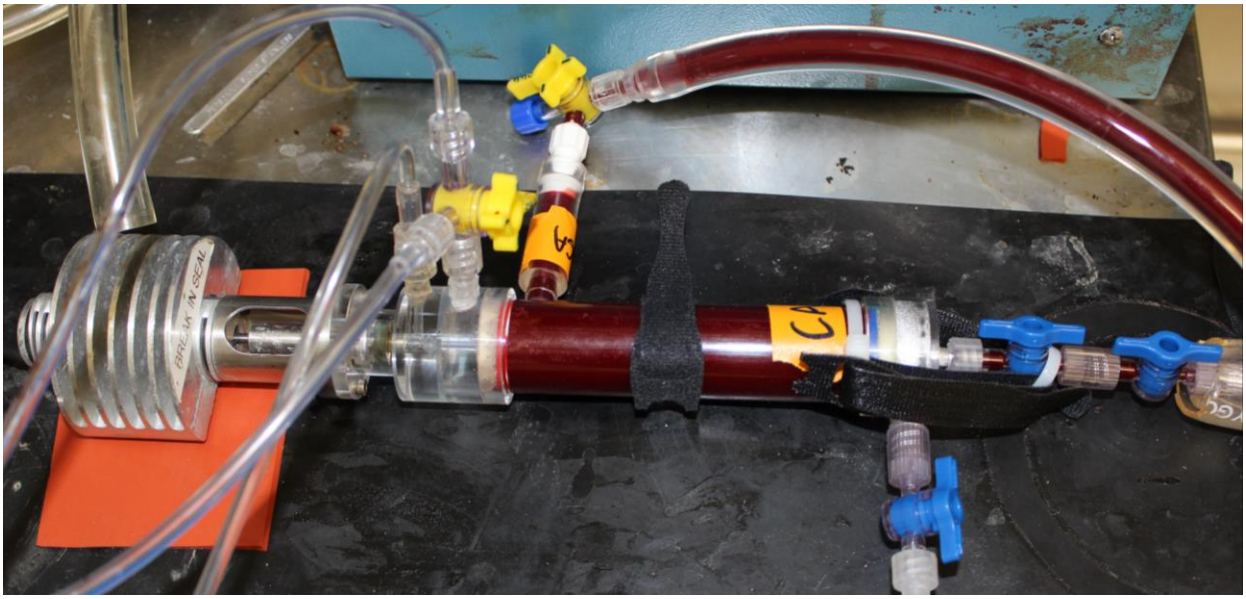

Figure 6.1. Mini-ULFED prototype with CA fibers in blood gas exchange loop.

6.2.2 Fiber Preparation & Assays

CA was immobilized to chitosan groups bound to surface amine groups on PMP fibers. The fiber immobilization protocol was initially developed and tested on siloxane-coated PP fiber [84], but adapted here for PMP fibers. PMP fibers were cleaned and aminated by plasma-enhanced chemical vapor disposition (PECVD) using an ION 40 plasma chamber (PVA Tepla, Corona, CA, USA). The number of available binding sites for CA immobilization were increased by treating aminated fibers with 5% glutaraldehyde in 100mM phosphate buffer (8.5 pH) followed by 1% chitosan (chitosan 448869; Sigma Aldrich, St. Louis, MO, USA) in 1% acetic acid to cross-link chitosan to surface groups. Residual chitosan non-covalently bound was cleaned from

fibers with a deionized water rinse. Fibers were left overnight in a bovine CA solution (1 mg/mL in 100 mM 8.5 pH phosphate buffer) (carbonic anhydrase C3934; Sigma Aldrich, St. Louis, MO, USA) after a second glutaraldehyde treatment to bind CA to chitosan activated amine groups.

Surface amination following chitosan binding on PMP fibers was quantified with a Sulfosuccinimidyl-4-0-(4,40-dimethoxytrityl) butyrate (sulfo-SDTB) colormetric amine assay (M109; ProChem Inc., Rockford, IL, USA) [144]. An NHS moiety in the sulfo-SDTB first binds to surface amine groups. A colormetric group on the sulfo-SDTB is then cleaved from bound molecules using perchloric acid after solution is rinsed away. Supernatant fluid is then quantified spectrophotometrically at 498 nm. Concentration was calculated from a standard curve generated with serial dilutions of sulfo-SDTB stock solution in 35% perchloric acid.

Carbonic anhydrase activity levels were measured using an esterase activity by monitoring the rate of hydrolysis of p-nitrophenyl acetate (p-NPA) to p-nitrophenol (p-NP). Activity was measured under both passive and shearing flow conditions. Passive flow testing followed the assay protocol verified previously and results were compared to reported activity levels for fibers used for gas exchange in earlier studies [84]. Activity was quantified prior to blood testing spectrophotometrically every 1 minute for 6 minutes at 412 nm in 114 fiber mats aminated and immobilized in parallel with the 523 fiber CA-ULFED mats. Mats were rolled and inserted into a 15 mL recirculating loop of 100 mM phosphate buffer 7.5 + 80 μM p-NPA at 45 mL/min. One activity unit is defined as the amount of CA necessary to hydrolyze 1 μmol p-NPA per minute. Assays were repeated for each mat (n=3) and the average of each is reported.

Shearing flow activity levels were measured to evaluate the non-permanent effects of active mixing on immobilized CA (e.g. possible conformational changes affecting catalytic rate in shearing flow). Fiber mats used in passive flow activity assays were potted into complete

mini-ULFED prototypes to replicate active mixing conditions of gas exchange devices. Activity was measured over 10 minutes at 2 minute increments in 60 mL recirculating loops of 100 mM phosphate buffer 7.5 + 80 μM p-NPA. Two control and two CA devices were tested from 0-30,000 RPM at 10,000 RPM increments. A fifth test device containing no fibers was fabricated to control for the effects of shearing flow on p-NPA independent of fibers. Measurements were replicated (n=2) at each rotation speed.

6.2.3 Gas Exchange Testing

CO_2 removal testing was conducted in a recirculating gas exchange loop as described in Section 4.2.2 using similar methods for blood collection, anticoagulation, and gas exchange measurements. Three fiber types were evaluated in mini-ULFED prototypes (untreated control fibers, chitosan immobilized control fibers, and CA immobilized fibers) for a total of six devices (n=2 of each). Gas exchange was measured at 10,000 RPM increments from 0-30,000 RPM, with a minimum of two measurements at each speed. Pure O_2 sweep gas was maintained at 3.0 L/min for all measurements to minimize potential variability between devices. A 0 RPM measurement was repeated after each rotation speed in the CA-fiber devices to validate that performance did not vary from baseline. Variance from baseline with repeated 0 RPM measurements may indicate permanent damage to immobilized CA.

Average device performances at minimum (0 RPM) and maximum (30,000 RPM) speeds were compared statistically in SPSS (PASW Statistics 18; IBM, Armonk, NY). One-way ANOVA with post-hoc Tukey t-tests were conducted for each rotation speed to evaluate the hypothesis that CA-fiber performance is greater than each control group. Appropriateness of parametric statistical comparisons was verified by testing assumptions of homogeneity of

variance and normality with Levene's test and Kolmogorov-Smirnov tests, respectively. Significance was accepted at the level of $p<0.05$.

6.3 RESULTS

6.3.1 Fiber Amine Density and Activity Assays

Results of the amine density assays are shown in Figure 6.2. Amine density of chitosan fibers (2.78 ± 0.52 nmol/cm^2) were significantly greater ($p>0.05$) than untreated PMP control fibers (0.04 ± 0.008 nmol/cm^2). This level of amination is comparable to surface densities reported by Kimmel et al. used for CA immobilizations and subsequent gas exchange testing [8].

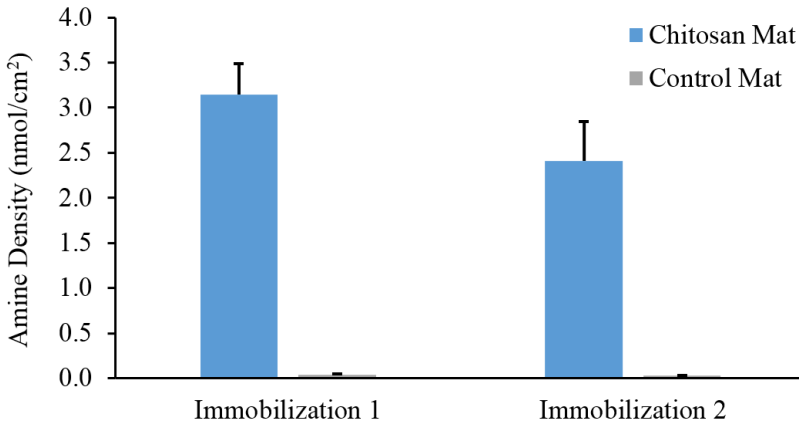

Figure 6.2. Average amine density on chitosan immobilized fibers versus control fibers. Chitosan data represents the average of two separate immobilizations corresponding to each mini-ULFED device tested in blood. Error bars represent one standard deviation.

Activity levels for passive flow activity assays are shown in Figure 6.3. Sample fiber mats from both immobilization had activity levels >0.005 μM/min/cm^2 under passive flow conditions. CO_2 removal rates from PBS were measured on these fibers (data not shown) under passive flow conditions to verify that percent enhancement versus control was consistent with previous work [84].

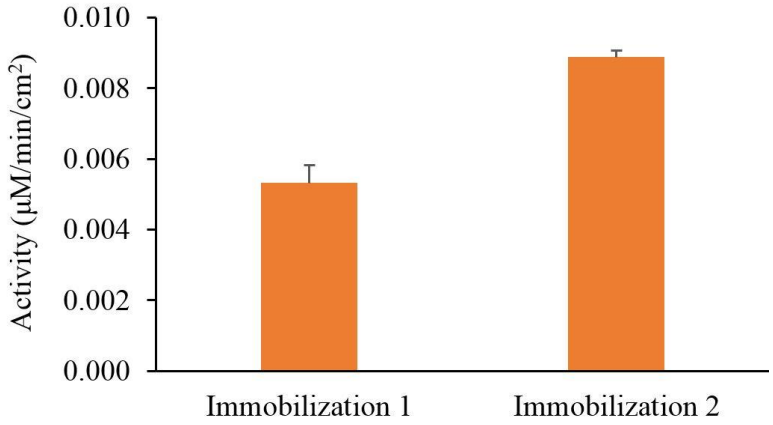

Figure 6.3. Immobilized carbonic anhydrase activity levels on mini-ULFED PMP fibers. Activity level is the average of repeated assays (n=3) on the same fiber set. Error bars represent one standard deviation.

Measured activity levels of the same 114 fiber mats under shearing flow are shown in Figure 6.4. Activity is reported as the average and standard deviation between two devices at each rotation speed. Fiberless control data is reported as average and standard deviation of

activity in one test with repeated measurements since only one device was fabricated. Average activity of the CA devices was significantly greater than the control devices (untreated fibers and fiber-less) at each rotation speed. This provides evidence that impeller generated flow and associated shear does not have a transient deactivation effect on immobilized CA enzyme. Overall activity levels in the CA device were lower than associated passive flow tests however the devices differ in geometry and this was anticipated. As rotation speed increased the apparent activity level increased by over 50% at 30,000 RPM versus passive (0 RPM) conditions in the CA device. This observation could indicate that CA activity becomes more active under shearing flow, but similar behavior in each of the control devices suggest this may be an artifact of the p-NPA assay.

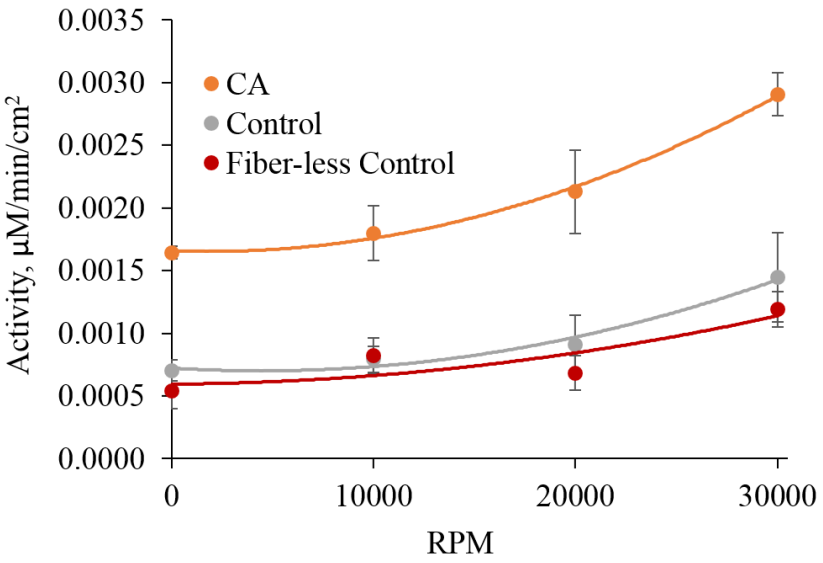

Figure 6.4. Mini-ULFED activity levels under shearing flow conditions. Error bars represent one standard deviation.

6.3.2 In Vitro Gas Exchange

Normalized CO_2 removal rates achieved in each test group are shown in Figure 6.5 as total performance of each device (left) and as percent enhancement at each rotation speed versus the untreated control fibers (right). Statistical analysis was conducted at minimum and maximum rotation speeds. At 0 RPM, CA was found to enhance CO_2 removal by 9% and 14% versus untreated control fibers and chitosan fibers (ANOVA with post-hoc Tukey test $p<0.05$) whereas no statistical difference was determined between chitosan and untreated fibers ($p>0.05$). At maximum speed, no statistical difference was found between any groups (ANOVA $p=0.94$). CA outperforming each control device at 0 RPM was anticipated, verifying the benefits of CA fibers under passive flow conditions as was shown previously [8, 84]. Chitosan fiber performance increased 63% from 0 RPM to 30,000 RPM, comparable to the 59% increase measured with untreated fibers and statistically indistinguishable at each rotation speed. In contrast, CA fiber performance increased by an average 44% for a maximum CO_2 removal rate within 2% of that achieved by the control devices.

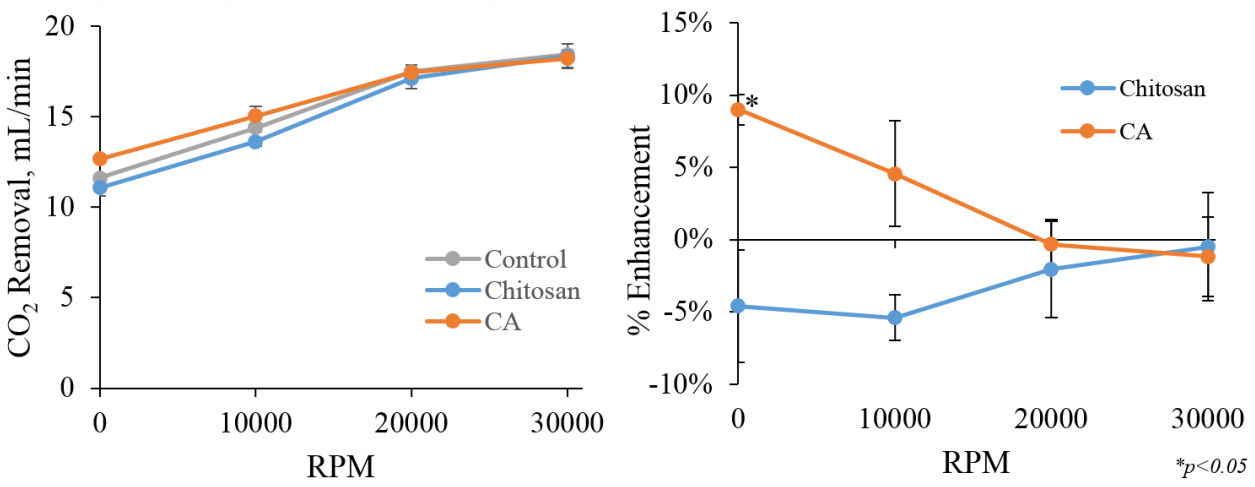

Figure 6.5. CO_2 Removal rate of CA-ULFED and controls versus rotation speed. (left) Total CO_2 removal rates of each test group (two devices each) versus rotation speed. (right) CO_2 removal performance of CA and chitosan fiber devices as percent enhancement versus control (untreated) fibers at each rotation speed.

6.4 DISCUSSION

Carbonic anhydrase enzyme fiber coatings have been shown to enhance CO_2 removal performance in low-flow artificial lung devices. PMP hollow fiber membranes were immobilized with CA using established methods and incorporated into a mini-ULFED to investigate the combined effects of active mixing and enzyme approaches. CA coated fibers were found to improve CO_2 removal by 9% under passive flow (0 RPM) conditions, but contributed to no additional gas exchange at the maximum rotation speed tested.

CA fibers offer a simplified approach to enhance CO_2 removal in low-flow devices. Use of CA fibers adds minimal bedside complexity to CO_2 removal systems and was shown to reduce

platelet deposition rates versus heparin control fibers [122]. Several other approaches to improve CO_2 removal are in development that use additional circuit components to continuously modify blood pH or electrolyte concentrations. Adding acidic species to whole blood or sweep gas has been explored to push the equilibrium of CO_2/bicarbonate ion toward CO_2 and increase blood pCO_2 [85–87]. This increases the partial pressure gradient driving CO_2 diffusion through fiber walls and increases gas transfer rates. Whole blood acidification with continuous lactic acid infusion increased CO_2 removal up to 78% in pigs [87]. Addition of small amounts of sulfur dioxide (SO_2) to sweep gas increased CO_2 removal by 17% in vitro, but synergistically enhanced CO_2 removal when combined with CA fibers by improving gas exchange by 109% [85]. Blood electrodialysis was shown to double CO_2 removal at 250 mL/min blood flow in pigs [88]. Further testing is necessary to assess the impact on renal function after ion concentrations were affected and required correction during treatment however. Direct elimination of bicarbonate ion from blood was also investigated by removing ultrafiltrate containing bicarbonate and replacing it sodium hydroxide replacement solution [90]. An average of 60 mL/min of CO_2 was removed in bicarbonate dialysis when ultrafiltrate was replaced at 100-150 mL/min.

Carbonic anhydrase is a native enzyme localized to erythrocytes that catalyzes the reversible hydration of CO_2 into carbonic acid that subsequently dissociates to bicarbonate ion. Through this reaction the CO_2 carrying capacity of blood is significantly increased, where >90% of CO_2 is in the form of bicarbonate or bound to hemoglobin [6, 33]. Physiologically this reaction is utilized for blood buffering but presents challenges for artificial lung operation by maintaining low CO_2 partial pressures in the blood. The relatively low pCO_2 gradient between blood and sweep gas limits pressure gradients driving diffusion of gas through the fiber membrane into the sweep gas as well as diffusion of CO_2 gas to the surface boundary layer.

Within the surface boundary layer dissolved CO_2 is quickly depleted. CO_2 replenishment is primarily dependent on the diffusion of additional CO_2 from bulk flow due to the slow uncatalyzed dehydration of HCO_3 to CO_2 and low red cell concentration in the boundary layer. Replenishment of CO_2 to the fiber surface slows as bulk pCO_2 drops, causing disequilibrium of HCO_3/CO_2 in the boundary layer. In previous work we demonstrated that immobilizing CA enzyme directly to fiber surfaces increases CO_2 removal efficiency by locally dehydrating bicarbonate ions to CO_2 at gas exchange surfaces [6–8, 84]. Up to 37% increased CO_2 removal from blood was achieved under passive flow conditions in miniaturized artificial lung modules. This effect was shown by Arazawa et al. to be most effective when disequilibrium in the boundary layer was greatest, i.e. when blood flow rate is minimized. In this work we hypothesized the contribution of CA coatings could be maximized when paired with conditions that reduce boundary layer thickness and promote HCO_3/CO_2 disequilibrium – conditions that align with objectives of the ULFED. Active mixing in the ULFED minimizes boundary layer thickness while low flows promote disequilibrium. By combining the demonstrated effects of impeller mixing in the ULFED with CA fibers we hypothesized the two technologies would complement each other, achieving greater CO_2 removal rates than either independently.

Gas exchange comparisons at 0 RPM are representative of passive flow conditions, so the higher removal rates measured in the CA device were anticipated. The percent enhancement under passive conditions was less than the 14-37% enhancement previously reported. The device geometry, flow pathways, and flow rate in the mini-ULFED differed enough that a reasonable prediction for passive flow conditions in our test device was not determined. Matching performances at the maximum rotation speed suggest that CA fibers do not increase gas exchange enhancement versus active mixing alone.

The mechanism explaining the finding that CA is ineffective versus active mixing alone is under investigation. Active mixing may cannibalize enhancement associated with CA fibers. Carbonic anhydrase coatings are thought to take advantage of disequilibrium within the boundary layer to locally convert HCO_3 to CO_2. Active mixing alternatively increases fluid velocity at the fiber surface to minimize the boundary layer thickness, reducing the diffusional distance for bulk CO_2 to reach the fiber surface. At extreme fluid velocities the boundary layer thickness can be effectively negligible. In such a system bulk CO_2 reaches the surface without diffusional resistance and immobilized CA competes with endogenous enzyme. This effect may not have been observed in passive flow modules due to the relatively low velocities versus an effective active mixing system.

Shear effects from aggressive impeller flows may also transiently deactivate immobilized CA. Unfolding of proteins under shearing flow is well documented for blood enzymes and evidence exists that transient unfolding can occur [145, 146]. To our knowledge no formal evaluations have been conducted specifically to investigate transient shear effects on CA enzyme. This theory was evaluated by measuring activity levels of CA fibers versus control devices in modified ULFED with impeller mixing. CA fiber activity was significantly greater than control activity at all rotation speeds, contributing evidence that impeller mixing does not transiently deactivate CA. A limitation of this analysis however is that p-NPA hydrolysis to p-NP by CA is dramatically slower than the corresponding bicarbonate/CO_2 reaction. The rate constant for HCO_3/CO_2 ($\sim 1 \times 10^6$ s^{-1}) is on the order of 1 million times greater than for p-NPA/p-NP (~ 1 s^{-1}) [147, 148]. Therefore measuring the slower p-NPA/p-NP reaction rate may not reveal a partial reduction in CA catalytic rate by shearing flow that affects HCO_3/CO_2 conversion. The

presented data here contributes evidence to the hypothesis that CA activity is preserved under shearing flow conditions, but limitations with the assay prevent fully supporting this conclusion.

7.0 SUMMARY AND CONCLUSIONS

Mechanical ventilation has long been the first point of care for patients suffering from hypercapnic lung failure. Less invasive ventilation techniques have shown patient benefit, but low CO_2 removal rates introduces new risks. Evidence continues to grow that extracorporeal CO_2 removal ($ECCO_2R$) can effectively prevent intubation, facilitate earlier extubation, or allow reduction of ventilator settings in hypercapnic respiratory failure. $ECCO_2R$ systems exist but improvements to system complexity and invasiveness are necessary to mitigate risks associated with high blood flow rates. The objective of this project was to develop novel CO_2 removal devices for clinically significant respiratory support that minimize invasiveness and simplify treatment.

The impeller percutaneous respiratory assist catheter (IPRAC) is an intravascular device that reduces system complexity as it requires no external blood circuitry. The IPRAC was previously shown to achieve the greatest CO_2 removal efficiency of any reported blood gas exchanger, with potential for further improvement through impeller design optimization. The effects of impeller spacing, number of vanes, and blade design were investigated with the objective of achieving CO_2 removal to 25-35% of the metabolic CO_2 production. We also targeted a reduction of the insertion diameter from 25 Fr to <20 Fr to minimize invasiveness. Reducing the spacing between impellers to allow additional impellers on the shaft was found to improve CO_2 removal rates, but all other effects were found to insignificantly affect

performance. Overall improvement in CO_2 removal performance was ~10% and maximum CO_2 removal rates of 15-20% metabolic CO_2 production was achieved.

Hemocompatibility studies were subsequently conducted with the IPRAC to establish the safety of impeller generated active mixing. Hemolytic contribution of the rotating impellers, fiber bundle, impeller/cage interactions, and surface finish (roughness) were systematically evaluated through in vitro hemolysis studies. Contact between rotating impellers and the surrounding safety coil was found to exacerbate cell damage, but this effect may be alleviated through surface treatments of impellers (polishing). Each other design component was found to insignificantly contribute to hemolysis, indicating the rotating impeller approach can be used safely in devices that may benefit from active mixing.

The rotating impeller technology was adapted for use in an extracorporeal artificial lung device. The objective of the ultra-low-flow $ECCO_2R$ device (ULFED) was to improve upon existing $ECCO_2R$ technologies by minimizing invasiveness and simplifying circuitry. Circuit blood flow rates on the order 250 mL/min are comparable to renal hemodialysis, and would enable use of patient connection strategies used for dialysis. Similar patient management strategies and circuity between dialysis and $ECCO_2R$ indicate potential for use of the ULFED directly with existing hemodialysis circuitry or with a hemodialysis machine. Removing CO_2 equivalent to 25-35% metabolic production at hemodialysis blood flows was demonstrated with a prototype modeled from the IPRAC. During feasibility testing an ULFED prototype achieved CO_2 removal of 75.3 mL/min at the target 250 mL/min blood flow rate. Identification of components that contributed to hemolysis and design features unnecessary for an extracorporeal device motivated a redesign of the ULFED prototype to tailor it for extracorporeal use.

A larger diameter ULFED prototype was designed to accommodate a rigid driveshaft that eliminated impeller/cage contact and allowed investigation of previously unexplored design features. A suitable range of device dimensions for the ULFED was determined using a theoretical critical rotation speed analysis. Additional design features previously uninvestigated in the IPRAC that may impact gas exchange were also evaluated (bundle aspect ratio and number of flow recirculation regions in the bundle – i.e. number of impellers). Bundle diameter was found to affect gas exchange performance where a reduction in the fiber bundle diameter improved gas exchange by ~30% versus other larger diameter prototypes. Length of the fiber bundle and the number of recirculation regions in the bundle were found to insignificantly affect total gas exchange. The CO_2 removal rate in the redesigned ULFED reached 74 mL/min (30-37% metabolic production) at 4,000 RPM and 250 mL/min blood flow.

Hemolysis studies were conducted with the top performing ULFED using both $ECCO_2R$ circuit components (centrifugal blood pump and ECMO cannula) and hemodialysis circuit components (roller pump and dialysis cannula). The time-of-therapy normalized rate of hemolysis (therapeutic index of hemolysis, TIH) using $ECCO_2R$ components was not statistically distinguishable from a control loop consisting of approved components. Hemolysis is therefore expected to be acceptable in vivo for the ULFED in this configuration. Hemolysis rates were higher using dialysis circuit components, however a reliable threshold for in vitro hemolysis for low-flow devices has not been established. The ULFED was shown to eliminate clinically significant levels of CO_2 from blood with acceptable hemolysis at hemodialysis blood flows, making minimally invasive dialysis connection strategies and simplified management possible for $ECCO_2R$.

Hollow fiber membranes with surface immobilized carbonic anhydrase have been shown to effectively enhance CO_2 removal rates from blood, with the most promising application being low-flow active mixing devices. Miniaturized ULFED prototypes were fabricated with CA immobilized fibers and evaluated for gas exchange. CA fibers together with active mixing may facilitate development of devices that can be miniaturized, operate at lower blood flows, at reduced rotation speeds, or achieve higher total gas exchange. These improvements could improve hemocompatibility, simplify treatment, or improve marketability of the ULFED. CO_2 removal rates under passive flow conditions (0 RPM) verified previous test results, however no significant difference was found between control and CA fibers as rotation speed increased.

7.1 FUTURE VISIONS

Among all concepts explored for partial support an intravascular device in theory may be the most attractive for respiratory assistance. Elimination of external circuitry and a blood pump reduces risks associated with blood outside the body, simplifies device management, and minimizes blood contacting surface area. Challenges for all intravascular devices remain achieving clinically significant gas exchange rates with a minimally invasive form factor. Active mixing was demonstrated among respiratory assist catheters to generate the most efficient CO_2 removal rates but significant improvements are necessary to match total performance of new extracorporeal CO_2 removal systems ($ECCO_2R$). Recent advances in $ECCO_2R$ technology and wider recognition of the clinical need has increased competition in the market space. Competitive development in $ECCO_2R$ focused on reducing risks, invasiveness, and complexity has advanced the field more quickly than competing technologies for intravascular devices. The

benefits of an intravascular design still give the concept a competitive advantage however, given the potential advantages for simplified support. Future work on the IPRAC may focus on integration of additional technologies that independently improve CO_2 removal. Demonstrated approaches feasible for an intravascular device such as adding fractions of acidic gas to fiber sweep gas could improve gas exchange if risks and challenges of such approaches are addressed. Other approaches that would enhance performance may include design improvements that allow higher surface areas without impacting insertion diameter. A collapsible impeller/cage assembly would allow expansion of a low-diameter device in situ. A design for two-stage insertion could also allow for placement of a packed fiber bundle that is later expanded by the impeller/cage assembly. Future intravascular technologies that improve or combine existing approaches for enhancing CO_2 removal, or development of new approaches would make respiratory assist catheters an attractive alternative to $ECCO_2R$.

Extracorporeal systems currently remain the most viable approach for simplified respiratory support. Growing competition to simplify systems and make attachment minimally invasive are pathways to wider clinical adoption, rather than limiting its use to ECMO centers. Most development in university research settings to enhance CO_2 removal rates has resulted in systems that add complexity to therapy. Approaches such as blood acidification, electrodialysis, or bicarbonate dialysis require additional circuit components and require monitoring and/or adjustment of blood pH and ionic concentrations. Industrial development in CO_2 removal has focused instead on approaches that simplify management with integrated systems and function similar to familiar therapies. The impeller technology and CA coating have an advantage over other CO_2 removal approaches in development because they minimize bedside complexity with minimal impact on the patient or circuit management. Impellers add complexity comparable to a

blood pump that is adjusted only to impact CO_2 removal rates, while CA enzyme coatings add no complexity to bedside systems. Demonstrating clinically significant gas exchange rates in the ULFED at operating conditions matching hemodialysis is a milestone in CO_2 removal. Intensivists treating patients with respiratory issues are the same clinicians already familiar or comfortable with dialysis systems. This leads to potential adoption of minimally invasive dialysis cannulation strategies, direct use with dialysis equipment, or to splice $ECCO_2R$ directly into existing dialysis circuitry. Future developments of the ULFED system may focus on design improvements independent of the gas exchange system or achieving secondary design objectives. Magnetically coupling or levitating the impeller driveshaft would seal the blood compartment, eliminating the need for driveshaft seals and the saline infusion line. Features identified to impact gas exchange such as bundle aspect ratio could be optimized to reduce priming volumes or further reduce necessary blood flow rates for treatment. Further developments with the ULFED, CA enzyme, and competing technologies will help push respiratory assistance to close logistical gaps between respiratory and renal dialysis and encourage widespread adaptation.

BIBLIOGRAPHY

1. Murphy S. et al., *National Vital Statistics Report - Deaths: Final Date for 2010*. Center for Disease Control; 2013.

2. Batchinsky A.I. et al., *Respiratory dialysis: Reduction in dependence on mechanical ventilation by venovenous extracorporeal CO2 removal**. Crit Care Med, 2011: p. 1382–1387.

3. Burki N.K. et al., *A novel extracorporeal CO2 removal system: Results of a pilot study in COPD patients with hypercapnic respiratory failure*. Chest, 2013. **143**(3): p. 678–686.

4. Bonin F. et al., *Avoidance of intubation during acute exacerbation of chronic obstructive pulmonary disease for a lung transplant candidate using extracorporeal carbon dioxide removal with the Hemolung*. J Thorac Cardiovasc Surg, 2013. **145**(5): p. e43–e44.

5. Mihelc K.M. et al., *Evaluation of a respiratory assist catheter that uses an impeller within a hollow fiber membrane bundle*. ASAIO J, 2009. **55**(6): p. 569–574.

6. Kaar J.L. et al., *Towards improved artificial lungs through biocatalysis*. Biomaterials, 2007. **28**(20): p. 3131–3139.

7. Arazawa D.T. et al., *Immobilized carbonic anhydrase on hollow fiber membranes accelerates CO2 removal from blood*. J Membr Sci, 2012. **403**–**404**: p. 25–31.

8. Kimmel J.D. et al., *Carbonic anhydrase immobilized on hollow fiber membranes using glutaraldehyde activated chitosan for artificial lung applications*. J Mater Sci Mater Med, 2013. **24**(11): p. 2611–2621.

9. CDC, *Health, United States, 2015: With Special Feature on Racial and Ethnic Health Disparities*. Hyattsville, MD: National Center for Health Statistics; 2016 p. 121.

10. Toy E.L. et al., *Treatment of COPD: Relationships between daily dosing frequency, adherence, resource use, and costs*. Respir Med, 2011. **105**(3): p. 435–441.

11. Kosacz N. et al., *Chronic obstructive pulmonary disease among adults--United States, 2011*. MMWR Morb Mortal Wkly Rep, 2012. **61**(46): p. 938–943.

12. *Chronic Obstructive Pulmonary Disease COPD*. American Lung Association; 2010 pp. 35–40.

13. Wells J.M. et al., *Pulmonary Arterial Enlargement and Acute Exacerbations of COPD*. N Engl J Med, 2012. **367**(10): p. 913–921.

14. Quon B.S. et al., *Contemporary management of acute exacerbations of copd*: A systematic review and metaanalysis*. Chest, 2008. **133**(3): p. 756–766.

15. Annich G, Lynch W, MacLaren G, Wilson J, and Bartlett Reds, eds *ECMO: Extracorporeal Cardiopulmonary Support in Critical Care*. (Annich G, Lynch W, MacLaren G, Wilson J, and Bartlett R, eds.) 4th ed. Ann Arbor, MI: Extracorporeal Life Support Organization; 2012.

16. Chandra D. et al., *Outcomes of Noninvasive Ventilation for Acute Exacerbations of Chronic Obstructive Pulmonary Disease in the United States, 1998–2008*. Am J Respir Crit Care Med, 2012. **185**(2): p. 152–159.

17. Rabe K.F. et al., *Global Strategy for the Diagnosis, Management, and Prevention of Chronic Obstructive Pulmonary Disease*. Am J Respir Crit Care Med, 2007. **176**(6): p. 532–555.

18. Phua J. et al., *Noninvasive ventilation in hypercapnic acute respiratory failure due to chronic obstructive pulmonary disease vs. other conditions: effectiveness and predictors of failure*. Intensive Care Med, 2005. **31**(4): p. 533–539.

19. Confalonieri M. et al., *A chart of failure risk for noninvasive ventilation in patients with COPD exacerbation*. Eur Respir J, 2005. **25**(2): p. 348–355.

20. Quinnell T.G. et al., *Prolonged invasive ventilation following acute ventilatory failure in copd*: Weaning results, survival, and the role of noninvasive ventilation*. CHEST J, 2006. **129**(1): p. 133–139.

21. Crummy F. et al., *The use of noninvasive mechanical ventilation in COPD with severe hypercapnic acidosis*. Respir Med, 2007. **101**(1): p. 53–61.

22. Lund L.W. and W.J. Federspiel, *Removing Extra CO2 in COPD Patients*. Curr Respir Care Rep, 2013. **2**(3): p. 131–138.

23. Fanelli V. et al., *Feasibility and safety of low-flow extracorporeal carbon dioxide removal to facilitate ultra-protective ventilation in patients with moderate acute respiratory distress sindrome*. Crit Care, 2016. **20**: p. 36.

24. *ARDS Lung Disease Data: 2008*. American Lung Association; 2008.

25. Cove M. et al., *Bench to bedside review: Extracorporeal carbon dioxide removal, past present and future*. Crit Care, 2012. **16**(5): p. 232–230.

26. Boyle A.J. et al., *Pharmacological treatments in ARDS; a state-of-the-art update*. BMC Med, 2013. **11**: p. 166.

27. Ware L.B. and M.A. Matthay, *The acute respiratory distress syndrome*. N Engl J Med, 2000. **342**(18): p. 1334–1349.

28. Brower R.G. et al., *Ventilation with lower tidal volumes as compared with traditional tidal volumes for acute lung injury and the acute respiratory distress syndrome*. N Engl J Med, 2000. **342**(18): p. 1301–1308.

29. Terragni P.P. et al., *Tidal Hyperinflation during Low Tidal Volume Ventilation in Acute Respiratory Distress Syndrome*. Am J Respir Crit Care Med, 2007. **175**(2): p. 160–166.

30. Slutsky A.S. and V.M. Ranieri, *Ventilator-Induced Lung Injury*. N Engl J Med, 2013. **369**(22): p. 2126–2136.

31. Kolobow T. et al., *The Carbon Dioxide Membrane Lung (CDML): A New Concept*. ASAIO J, 1977. **23**(1): p. 17–21.

32. Gattinoni L. et al., *Treatment of Acute Respiratory Failure with Low-Frequency Positive-Pressure Ventilation and Extracorporeal Removal of CO2*. The Lancet, 1980. **316**(8189): p. 292–294.

33. Silverthorn D.U., *Human Physiology: An Integrated Approach*. 4th ed. San Francisco: Pearson Education, Inc.; 2007.

34. Loeppky J.A. et al., *Quantitative description of whole blood CO2 dissociation curve and Haldane effect*. Respir Physiol, 1983. **51**(2): p. 167–181.

35. MacLaren G. et al., *Contemporary extracorporeal membrane oxygenation for adult respiratory failure: life support in the new era*. Intensive Care Med, 2012. **38**(2): p. 210–220.

36. Schmidt M. et al., *Blood oxygenation and decarboxylation determinants during venovenous ECMO for respiratory failure in adults*. Intensive Care Med, 2013. **39**(5): p. 838–846.

37. Wearden P.D. et al., *Respiratory dialysis with an active-mixing extracorporeal carbon dioxide removal system in a chronic sheep study*. Intensive Care Med, 2012. **38**(10): p. 1705–1711.

38. Dogal N.M. et al., *Evaluation of Three Hollow-Fiber Membrane Oxygenators Without Integrated Arterial Filters for Neonatal Cardiopulmonary Bypass*. Perfusion, 2012. **27**(2): p. 132–140.

39. Kopp R. et al., *Hemocompatibility of a Miniaturized Extracorporeal Membrane Oxygenation and a Pumpless Interventional Lung Assist in Experimental Lung Injury*. Artif Organs, 2010. **34**(1): p. 13–21.

40. Lehle K. et al., *Efficiency of gas transfer in venovenous extracorporeal membrane oxygenation: analysis of 317 cases with four different ECMO systems*. Intensive Care Med, 2014. doi:10.1007/s00134-014-3489-z.

41. Hattler B.G. et al., *A respiratory gas exchange catheter: In vitro and in vivo tests in large animals*. J Thorac Cardiovasc Surg, 2002. **124**(3): p. 520–530.

42. Conrad S.A. et al., *Major findings from the clinical trials of the intravascular oxygenator*. Artif Organs, 1994. **18**(11): p. 846–863.

43. Snider M.T. et al., *Small intrapulmonary artery lung prototypes: Design, construction, and in vitro water testing*. ASAIO J, 1994. **40**(3): p. M533–M539.

44. Makarewicz A.J. et al., *A pumping intravascular artificial lung with active mixing*. ASAIO J, 1993. **39**(3): p. M466–M469.

45. Cattaneo G.F.M. et al., *Intravascular blood oxygenation using hollow fibers in a disk-shaped configuration: Experimental evaluation of the relationship between porosity and performance*. ASAIO J, 2006. **52**(2): p. 180–185.

46. Kim G.-B. et al., *Design of an intravenous oxygenator*. J Artif Organs, 2006. **9**(1): p. 34–41.

47. Lick S.D. et al., *Paracorporeal artificial lung: Perioperative management for survival study in sheep*. J Invest Surg, 2003. **16**(3): p. 177–184.

48. Zhou X. et al., *Long-term support with an ambulatory percutaneous paracorporeal artificial lung*. J Heart Lung Transplant, 2012. **31**(6): p. 648–654.

49. Zwischenberger J.B. et al., *The paracorporeal artificial lung improves 5-day outcomes from lethal smoke/burn-induced acute respiratory distress syndrome in sheep*. Ann Thorac Surg, 2002. **74**(4): p. 1011–1018.

50. Federspiel W.J. and R.G. Svitek, *Lung, Artificial: Current Research and Future Directions*. In: Wnek GE, and Bowlin GL, eds. Encyclopedia of Biomaterials and Biomedical Engineering. New York, NY: Marcel Dekker, Inc.; 2004. pp. 922–931.

51. Mockros L.F. and R. Leonard, *Compact cross-flow tubular oxygenators*. Trans - Am Soc Artif Intern Organs, 1985. **31**: p. 628–633.

52. Federspiel W.J. and K.A. Henchir, *Lung, Artificial: Basic Principles and Current Applications*. In: Wnek GE, and Bowlin GL, eds. Encyclopedia of Biomaterials and Biomedical Engineering. New York, NY: Marcel Dekker, Inc.; 2004. pp. 910–921.

53. Trahanas J.M. et al., *Extracorporeal Support for Chronic Obstructive Pulmonary Disease: A Bright Future*. J Intensive Care Med, 2016. doi:10.1177/0885066616663119.

54. Morelli A. et al., *Extracorporeal carbon dioxide removal (ECCO2R) in patients with acute respiratory failure*. Intensive Care Med, 2017. doi:10.1007/s00134-016-4673-0.

55. Conrad S.A. et al., *Prolonged intracorporeal support of gas exchange with an intravenacaval oxygenator*. Chest, 1993. **103**(1): p. 158–161.

56. Mortensen J.D. and G. Berry, *Conceptual and design features of a practical, clinically effective intravenous mechanical blood oxygen/carbon dioxide exchange device (IVOX)*. Int J Artif Organs, 1989. **12**(6): p. 384–389.

57. Cox Jr. S.C. et al., *Development and current status of a new intracorporeal membrane oxygenator (IVOX)*. Perfusion, 1991. **6**(4): p. 291–296.

58. Eash H.J. et al., *Evaluation of Fiber Bundle Rotation for Enhancing Gas Exchange in a Respiratory Assist Catheter*. ASAIO J, 2007. **53**(3): p. 368–373.

59. Hattler B.G. et al., *Respiratory Dialysis: A New Concept In Pulmonary Support*. ASAIO J, 1992. **38**: p. M322–M325.

60. Federspiel W.J. et al., *Experimental Evaluation of a Model for Oxygen Exchange in a Pulsating Intravascular Artificial Lung*. Ann Biomed Eng, 2000. **28**(2): p. 160–167.

61. Nodelman V. et al., *Enhancement of O2 and CO2 transfer through microporous hollow fibers by pressure cycling*. Ann Biomed Eng, 1998. **26**(6): p. 1044–1054.

62. Cattaneo G. et al., *Compact intra-and extracorporeal oxygenator developments*. Perfusion, 2004. **19**(4): p. 251–255.

63. Muller T. et al., *Extracorporeal pumpless interventional lung assist in clinical practice: determinants of efficacy*. Eur Respir J, 2008. **33**(3): p. 551–558.

64. Wang D. et al., *Toward ambulatory arteriovenous CO2 removal: Initial studies and prototype development*. ASAIO J, 2003. **49**(5): p. 564–567.

65. Zwischenberger J.B. et al., *Percutaneous extracorporeal arteriovenous CO2 removal for severe respiratory failure*. Ann Thorac Surg, 1999. **68**(1): p. 181–187.

66. Kluge S. et al., *Avoiding invasive mechanical ventilation by extracorporeal carbon dioxide removal in patients failing noninvasive ventilation*. Intensive Care Med, 2012. **38**(10): p. 1632–1639.

67. Flörchinger B. et al., *Pumpless Extracorporeal Lung Assist: A 10-Year Institutional Experience*. Ann Thorac Surg, 2008. **86**(2): p. 410–417.

68. Jeffries R.G. et al., *Pre-clinical evaluation of an adult extracorporeal carbon dioxide removal system with active mixing for pediatric respiratory support*. Int J Artif Organs, 2014. **37**(12): p. 888–899.

69. Mani R.K. et al., *Respiratory Dialysis for Avoidance of Intubation in Acute Exacerbation of COPD*. J Novemb, 2013. **59**(6): p. 675–678.

70. Cole S. et al., *Extracorporeal carbon dioxide removal as an alternative to endotracheal intubation for non-invasive ventilation failure in acute exacerbation of COPD*. J Intensive Care Soc, 2014. **15**(4): p. 1–3.

71. Hermann A. et al., *A novel pump-driven veno-venous gas exchange system during extracorporeal CO2-removal*. Intensive Care Med, 2015: p. 1–8.

72. Braune S. et al., *The feasibility and safety of extracorporeal carbon dioxide removal to avoid intubation in patients with COPD unresponsive to noninvasive ventilation for acute hypercapnic respiratory failure (ECLAIR study): multicentre case-control study*. Intensive Care Med, 2016. doi:10.1007/s00134-016-4452-y.

73. Gramaticopolo S. et al., *Extracorporeal CO2 Removal – A Way to Achieve Ultraprotective Mechanical Ventilation and Lung Support: The Missing Piece of Multiple Organ Support Therapy*. Contrib Nephrol, 2010. **165**: p. 174–184.

74. Ruberto F. et al., *Extracorporeal Removal CO2 Using a Venovenous, Low-Flow System (Decapsmart) in a Lung Transplanted Patient: A Case Report*. Transplant Proc, 2009. **41**(4): p. 1412–1414.

75. Terragni P.P. et al., *Tidal Volume Lower than 6 ml/kg Enhances Lung Protection: Role of Extracorporeal Carbon Dioxide Removal*. Anesthesiology, 2009. **111**(4): p. 826–835.

76. Moscatelli A. et al., *Noninvasive ventilation and low-flow veno-venous extracorporeal carbon dioxide removal as a bridge to lung transplantation in a child with refractory hypercapnic respiratory failure due to bronchiolitis obliterans**. Pediatr Crit Care Med, 2010. **11**(1): p. e8–e12.

77. Del Sorbo L. et al., *Extracorporeal CO2 Removal in Hypercapnic Patients At Risk of Noninvasive Ventilation Failure: A Matched Cohort Study With Historical Control*. Crit Care Med, 2015. **43**(1): p. 120–127.

78. Karagiannidis C. et al., *Veno-venous extracorporeal CO2 removal for the treatment of severe respiratory acidosis: pathophysiological and technical considerations*. Crit Care, 2014. **18**(3): p. R124.

79. *A Multicenter Randomized Control Trial (RCT) to Determine Safety and Efficacy of PALP™ for ECCO2-R in Conjunction With Liberation From Mechanical Ventilation (MV) Compared to MV Alone in COPD Exacerbation and Respiratory Failure (NCT02107222)*. ClinicalTrials.gov, 2014 https://clinicaltrials.gov/ct2/show/NCT02107222. Accessed October 18, 2016.

80. Godet T. et al., *Novel CO2 removal device driven by a renal-replacement system without hemofilter. A first step experimental validation*. Anaesth Crit Care Pain Med, 2015. **34**(3): p. 135–140.

81. *"Low Flow" CO2 Removal Via a Membrane Gas Exchange Device (Prismalung®) on a Renal Replacement Platform (Prismaflex®) in Hypercapnic, Ventilated Patients Requiring Renal Replacement (NCT02590575)*. ClinicalTrials.gov, 2016 https://clinicaltrials.gov/ct2/show/NCT02590575. Accessed August 30, 2016.

82. *Extracorporeal CO2 Removal (ECCO2R) With a Renal Replacement Platform (PRISMALUNG) to Enhance Lung Protective Ventilation in Patients With Mild to Moderate Acute Respiratory Distress Syndrome (ARDS) (NCT02606240)*. ClinicalTrials.gov, 2016 https://clinicaltrials.gov/ct2/show/NCT02606240. Accessed August 30, 2016.

83. *Ultra-protective Pulmonary Ventilation Supported by Low Flow Extracorporeal Carbon Dioxide Removal (ECCO2R) and Prone Positioning for ARDS; a Pilot Study. (NCT02252094)*. ClinicalTrials.gov, 2016 https://clinicaltrials.gov/ct2/show/NCT02252094?term=extracorporeal+co2&rank=20. Accessed .

84. Arazawa D.T. et al., *Kinetics of CO2 exchange with carbonic anhydrase immobilized on fiber membranes in artificial lungs*. J Mater Sci Mater Med, 2015. **26**(6): p. 5525.

85. Arazawa D.T. et al., *Acidic sweep gas with carbonic anhydrase coated hollow fiber membranes synergistically accelerates CO2 removal from blood*. Acta Biomater, 2015. doi:10.1016/j.actbio.2015.07.007.

86. Zanella A. et al., *Blood acidification enhances carbon dioxide removal of membrane lung: An experimental study*. Intensive Care Med, 2009. **35**(8): p. 1484–1487.

87. Zanella A. et al., *Regional Blood Acidification Enhances Extracorporeal Carbon Dioxide Removal: A 48-hour Animal Study. [Miscellaneous Article]*. Anesthesiol Febr 2014, 2014. **120**(2): p. 416–424.

88. Zanella A. et al., *Respiratory Electrodialysis: a Novel, Highly Efficient, Extracorporeal CO2 Removal Technique*. Am J Respir Crit Care Med, 2015. **192**(6): p. 719–726.

89. Zanella A. et al., *Extracorporeal CO2 removal by respiratory electrodialysis: an in-vitro study*. ASAIO J, 2015. doi:10.1097/MAT.0000000000000316.

90. Cressoni M. et al., *Decreasing pulmonary ventilation through bicarbonate ultrafiltration: An experimental study*. Crit Care Med, 2009. **37**(9): p. 2612–2618.

91. Jeffries R.G. et al., *Effect of Impeller Design and Spacing on Gas Exchange in a Percutaneous Respiratory Assist Catheter*. Artif Organs, 2014. **38**(12): p. 1007–1017.

92. Kaushik M. et al., *Extracorporeal Carbon Dioxide Removal: The Future of Lung Support Lies in the History*. Blood Purif, 2012. **34**(2): p. 94–106.

93. Habashi N.M. et al., *Low blood flow extracorporeal carbon dioxide removal (ECCO2R): A review of the concept and a case report*. Intensive Care Med, 1995. **21**(7): p. 594–597.

94. Bigatello L.M. et al., *Outcome of patients undergoing prolonged mechanical ventilation after critical illness*. Crit Care Med, 2007. **35**(11): p. 2491–2497.

95. Pesenti A. et al., *Carbon dioxide dialysis will save the lung*. Crit Care Med, 2010. **38**(10 SUPPL.): p. S549–S554.

96. Thourani V.H. et al., *Venoarterial Extracorporeal Membrane Oxygenation (VA-ECMO) in Pediatric Cardiac Support*. Ann Thorac Surg, 2006. **82**(1): p. 138–145.

97. Federspiel W.J. and R.G. Svitek, *Lung, Artificial: Current Research and Future Directions*. In: Wnek GE, and Bowlin GL, eds. Encyclopedia of Biomaterials and Biomedical Engineering. New York, NY: Marcel Dekker, Inc.; 2004. pp. 922–931.

98. Macha M. et al., *Acute In Vivo Studies of the Pittsburgh Intravenous Membrane Oxygenator*. ASAIO J, 1996. **42**(5): p. M609–M615.

99. Zwischenberger J.B. et al., *Intravascular membrane oxygenator and carbon dioxide removal devices: A review of performance and improvements*. ASAIO J, 1999. **45**(1): p. 41–46.

100. Eash H.J. et al., *Evaluation of Local Gas Exchange in a Pulsating Respiratory Support Catheter*. ASAIO J, 2005. **51**(2): p. 152–157.

101. Svitek R.G. and W.J. Federspiel, *A Mathematical Model to Predict CO2 Removal in Hollow Fiber Membrane Oxygenators*. Ann Biomed Eng, 2008. **36**(6): p. 992–1003.

102. Vaslef S.N. et al., *Use of a mathematical model to predict oxygen transfer rates in hollow fiber membrane oxygenators*. ASAIO J, 1994. **40**(4): p. 990–996.

103. Wickramasinghe S.R. et al., *Mass transfer in various hollow fiber geometries*. J Membr Sci, 1992. **69**(3): p. 235–250.

104. Turri F. and J.I. Yanagihara, *Computer-assisted numerical analysis for oxygen and carbon dioxide mass transfer in blood oxygenators*. Artif Organs, 2011. **35**(6): p. 579–592.

105. Lathem W., *The renal excretion of hemoglobin: Regulatory mechanisms and the differential excretion of free and protein-bound hemoglobin*. J Clin Invest, 1959. **38**(4): p. 652–658.

106. Ottenberg R. and C.L. Fox, *The rate of removal of hemoglobin from the circulation and its renal threshold in human beings*. Am J Physiol, 1938. **123**(2): p. 516–525.

107. Andersen M.N. et al., *Mechanisms of plasma hemoglobin clearance after acute hemolysis: studies in open-heart surgical patients.* Ann Surg, 1966. **163**(4): p. 529–536.

108. Olsen D.B., *The History of Continuous-Flow Blood Pumps*. Artif Organs, 2000. **24**(6): p. 401–404.

109. Rother RP et al., *The clinical sequelae of intravascular hemolysis and extracellular plasma hemoglobin: A novel mechanism of human disease*. JAMA, 2005. **293**(13): p. 1653–1662.

110. Araki K. et al., *Hemolysis and Heat Generation in Six Different Types of Centrifugal Blood Pumps*. Artif Organs, 1995. **19**(9): p. 928–932.

111. Araki K. et al., *Heat Generation and Hemolysis at the Shaft Seal in Centrifugal Blood Pumps*. ASAIO, 1995. **3**(41).

112. Anai H. et al., *An Approach to Reducing Hemolysis in an Axial-Flow Blood Pump*. ASAIO, 1995. **41**(3).

113. Burgreen G.W. et al., *Computational Fluid Dynamics Analysis of a Maglev Centrifugal Left Ventricular Assist Device*. Artif Organs, 2004. **28**(10): p. 874–880.

114. Umezu M. et al., *Effects of Surface Roughness on Mechanical Hemolysis*. Artif Organs, 1996. **20**(5): p. 575–578.

115. *ASTM F1841-97 (2005). Standard Practice for Assessment of Hemolysis in Continuous Flow Blood Pumps*.

116. Dobrovolskaia M.A. et al., *Method for Analysis of Nanoparticle Hemolytic Properties in Vitro*. Nano Lett, 2008. **8**(8): p. 2180–2187.

117. Wu Z.J. et al., *Computational Fluid Dynamics and Experimental Characterization of the Pediatric Pump-Lung*. Cardiovasc Eng Technol, 2011. **2**(4): p. 276–287.

118. Monroe J.M. et al., *Surface roughness and edge geometries in hemolysis with rotating disk flow*. J Biomed Mater Res, 1981. **15**(6): p. 923–939.

119. Maruyama O. et al., *Hemolysis Resulting From Surface Roughness Under Shear Flow Conditions Using a Rotational Shear Stressor*. Artif Organs, 2006. **30**(5): p. 365–370.

120. Oliver W.C., *Anticoagulation and Coagulation Management for ECMO*. Semin Cardiothorac Vasc Anesth, 2009. **13**(3): p. 154–175.

121. Holme P.A. et al., *Shear-Induced Platelet Activation and Platelet Microparticle Formation at Blood Flow Conditions as in Arteries With a Severe Stenosis*. Arterioscler Thromb Vasc Biol, 1997. **17**(4): p. 646–653.

122. Oh H.I. et al., *Hemocompatibility assessment of carbonic anhydrase modified hollow fiber membranes for artificial lungs*. Artif Organs, 2010. **34**(5): p. 439–442.

123. Peek G.J. et al., *Efficacy and economic assessment of conventional ventilatory support versus extracorporeal membrane oxygenation for severe adult respiratory failure (CESAR): a multicentre randomised controlled trial*. The Lancet, 2009. **374**(9698): p. 1351–1363.

124. Lightowler J.V. et al., *Non-invasive positive pressure ventilation to treat respiratory failure resulting from exacerbations of chronic obstructive pulmonary disease: Cochrane systematic review and meta-analysis*. BMJ, 2003. **326**(7382): p. 185.

125. *ANSI/AAMI/ISO 7199:2009 -- Cardiovascular implants and artificial organs — Blood-gas exchangers (oxygenators)*. 2009.

126. Abrams D.C. et al., *Pilot Study of Extracorporeal Carbon Dioxide Removal to Facilitate Extubation and Ambulation in Exacerbations of Chronic Obstructive Pulmonary Disease*. Ann Am Thorac Soc, 2013. **10**(4): p. 307–314.

127. Hermann A. et al., *First Experience With a New Miniaturized Pump-Driven Venovenous Extracorporeal CO2 Removal System (iLA Activve): A Retrospective Data Analysis*. ASAIO J, 2014. **60**(3): p. 342–347.

128. Moss C.E. et al., *A retrospective observational case series of low flow veno-venous extracorporeal carbon dioxide removal use in patients with respiratory failure:* ASAIO J, 2016: p. 1.

129. Bein T. et al., *Lower tidal volume strategy (≈3 ml/kg) combined with extracorporeal CO2 removal versus "conventional" protective ventilation (6 ml/kg) in severe ARDS*. Intensive Care Med, 2013. **39**(5): p. 847–856.

130. Hewitt T.J. et al., *A mathematical model of gas exchange in an intravenous membrane oxygenator*. Ann Biomed Eng, 1998. **26**(1): p. 166–178.

131. Ahmed T. and M.J. Semmens, *Use of Transverse Flow Hollow Fibers for Bubbleless Membrane Aeration*. Water Res, 1996. **30**(2): p. 440–446.

132. Fujii Y. and S. Kigoshi, *Characterization of Hollow-Fiber Membranes*. J Chem Eng Jpn, 1994. **27**(3): p. 321–328.

133. Vaslef S.N. et al., *Design and Evaluation of a New, Low Pressure Loss, Implantable Artificial Lung*. ASAIO J, 1994. **40**(3): p. M522–M526.

134. Yang M.-C. and E.L. Cussler, *Designing hollow-fiber contactors*. AIChE J, 1986. **32**(11): p. 1910–1916.

135. Vaslef S.N. et al., *Computer-Assisted design of an implantable, intrathoracic artificial lung*. Artif Organs, 1994. **18**(11): p. 813–817.

136. *Medtronic Minimax Plus, Instructions For Use: M932349A001 Rev. 1.0*. 2008.

137. Svitek R.G. et al., *In Vitro Evaluation of the TandemHeart Pediatric Centrifugal Pump:* ASAIO J, 2007. **53**(6): p. 747–753.

138. Paulsen M.J. et al., *A Simple, Standard Method to Characterize Pressure/Flow Performance of Vascular Access Cannulas:* ASAIO J, 2013. **59**(1): p. 24–29.

139. Zimmermann M. et al., *Pumpless extracorporeal interventional lung assist in patients with acute respiratory distress syndrome: a prospective pilot study*. Crit Care, 2009. **13**(1): p. R10.

140. Bein T. et al., *A new pumpless extracorporeal interventional lung assist in critical hypoxemia/hypercapnia**. Crit Care Med, 2006. **34**(5): p. 1372–1377.

141. Jeffries R.G., *In Vitro and Seven-Day Chronic In Vivo Evaluation of the Hemolung Adult CO2 Removal System for Pediatric Respiratory Support*. 2014.

142. Kawahito S. et al., *Blood trauma induced by clinically accepted oxygenators*. ASAIO J, 2001. **47**(5): p. 492–495.

143. Bernstein E.F. et al., *Some biologic limitations to prolonged blood pumping*. ASAIO Trans, 1965. **11**(1).

144. Cook A.D. et al., *Colorimetric analysis of surface reactive amino groups on poly(lactic acid-co-lysine):poly(lactic acid) blends*. Biomaterials, 1997. **18**(21): p. 1417–1424.

145. Siediecki C.A. et al., *Shear-dependent changes in the three-dimensional structure of human von Willebrand factor*. Blood, 1996. **88**(8): p. 2939–2950.

146. Jaspe J. and S.J. Hagen, *Do Protein Molecules Unfold in a Simple Shear Flow?* Biophys J, 2006. **91**(9): p. 3415–3424.

147. Gilmour K.M., *Perspectives on carbonic anhydrase*. Comp Biochem Physiol A Mol Integr Physiol, 2010. **157**(3): p. 193–197.

148. Thorslund A. and S. Lindskog, *Studies of the Esterase Activity and the Anion Inhibition of Bovine Zinc and Cobalt Carbonic Anhydrases*. Eur J Biochem, 1967. **3**(1): p. 117–123.